NON-DESTRUCTIVE EVALUATION OF THE CONDITION OF SUBSURFACE DRAINAGE IN PAVEMENT USING GROUND PENETRATING RADAR (GPR)

A Dissertation

Submitted to the Faculty

of

Purdue University

by

Hao Bai

In Partial Fulfillment of the

Requirements for the Degree

of

Doctor of Philosophy

December 2020

Purdue University

West Lafayette, Indiana

THE PURDUE UNIVERSITY GRADUATE SCHOOL
STATEMENT OF COMMITTEE APPROVAL

Dr. Joseph V. Sinfield, Chair

Lyles School of Civil Engineering

Dr. Maria Caterina Santagata

Lyles School of Civil Engineering

Dr. Mark R. Bell

School of Electrical and Computer Engineering

Dr. Robert L. Nowack

Department of Earth, Atmospheric, and Planetary Sciences

Approved by:

Dr. Dulcy M Abraham

Chair, Burke Graduate Program,
Lyles School of Civil Engineering

ACKNOWLEDGMENTS

This work was supported in part by the Joint Transportation Research Program administered by the Indiana Department of Transportation (INDOT) and Purdue University. The authors would also like to thank Dr. Dwayne Harris and other INDOT staff for assisting with data collection. The contents of this thesis reflect the views of the authors, who are responsible for the facts and the accuracy of the data presented herein, and do not necessarily reflect the official views or policies of the sponsoring organizations. These contents do not constitute a standard, specification, or regulation.

TABLE OF CONTENTS

LIST OF TABLES

LIST OF FIGURES

ABSTRACT

Bai, Hao Ph.D., Purdue University, December 2020. Non-destructive Evaluation of the Condition of Subsurface Drainage in Pavement Using Ground Penetrating Radar (GPR) . Major Professor: Joseph V. Sinfield.

Pavement drainage systems are one of the key drivers of pavement function and longevity, and effective drain maintenance can significantly extend a pavement's service life. Maintenance of these drains, however, is often hampered by the challenge of locating the drains. Ground Penetrating Radar (GPR) typically offers a rapid and effective method to detect these underground targets. However, typical detection schema that rely upon the observation of the hyperbolic return from a GPR scan of a buried conduit still tend to miss many of the older drains beneath pavements as they may be partially or fully filled with sediment and/or may be fabricated from clay or other earthen materials, yielding a return signal that is convolved with significant background noise.

To manage this challenge, this work puts forward an improved background noise and clutter reduction method to enhance the target signals in what amounts to a constructed environment that tends to have more consistent subsurface properties than one might encounter in a general setting. Within this technique, two major algorithms are employed. Algorithm 1 is the core of this method, and plays the role of reducing background noise and clutter. Algorithm 2 is supplementary, and helps eliminate anomalous discontinuous returns generated by the equipment itself, which could otherwise lead to false detection indications in the output of Algorithm 1. Instead of traditional 2-D GPR images, the result of the proposed algorithms is a 1-D plot along the survey line, highlighting a set of "points of interest" that could indicate buried drain locations identified at any given GPR operating frequency. Subsurface exploration using two different operating frequencies, 900 MHz and 400 MHz herein, is then employed to further enhance detection confidence. Points of interest are ultimately coded to define the confidence of the detection. Comparing the

final result of proposed algorithms with the original GPR images, the improved algorithm is demonstrated to provide significantly improved detection results, and could potentially be applied to similar problems in other contexts.

Besides the background reduction methods, a group of simulations performed using GPRMAX2D software are examined to explore the influence of road cross-section designs on sub-pavement drainage conduit GPR signatures, and evaluate the effectiveness of alternate GPR antennae configurations in locating these buried conduits in different ground conditions. Two different models were explored to simulate conduit detection. In addition, different pipe and soil conditions were modeled, such as pipe size, pipe material, soil moisture level, and soil type. Four different quantitative measurements are used to analyze GPR performance based on different key factors. The four measurements are 1) signal to background ratio (SBR) in dB; 2) signal to receiver noise ratio (SNR) in dB; 3) signal energy in Volts; and 4) average signal band power in Watts.

The water and clay content of subsurface soil can significantly influence the detection results obtained from ground penetrating radar (GPR). Due to the variation of the material properties underground, the center frequency of transmitted GPR signals shifts to a lower range as wave attenuation increases. Examination of wave propagation in the subsurface employing an attenuation filter based on a linear system model shows that received GPR signals will be shifted to lower frequencies than those originally transmitted. The amount of the shift is controlled by a wave attenuation factor, which is determined by the dielectric constant, electric conductivity, and magnetic susceptibility of the transmitted medium. This work introduces a receiver-transmitter-receiver dual-frequency configuration for GPR that employs two operational frequencies for a given test - one higher and one slightly lower - to take advantage of this phenomenon to improve subpavement drain detection results. In this configuration, the original signal is transmitted from the higher frequency transmitter. After traveling through underground materials, the signal is received by two receivers with different frequencies. One of the receivers has the same higher center frequency as the transmitter, and the other receiver has a lower center frequency. This configuration can be expressed as Rx(low-frequency)-Tx(high-frequency)-Rx(high-frequency) and was applied

in both laboratory experiments and field tests. Results are analyzed in the frequency domain to evaluate and compare the properties of the signal obtained by both receivers. The laboratory experiment used the configuration of Rx(400MHz)-Tx(900MHz)-Rx(900MHz). The field tests, in addition to the configuration used in the lab tests, employed another configuration of Rx(270MHz)-Tx(400MHz)-Rx(400MHz) to obtain more information about this phenomenon. Both lab and field test results illustrate the frequency-shift phenomenon described by theoretical calculations. Based on the power spectrum for each signal, the lower frequency antenna typically received more energy (higher density values) at its peak frequency than the higher frequency antenna.

1. INTRODUCTION

Subsurface drainage features are routinely incorporated in the design of pavement systems as they are believed to increase pavement service life provided that they are installed correctly and maintained. When poorly maintained, the existence of the drains can lead to roadway freeze-thaw damage or differential settlement, as obstructed or otherwise damaged conduits can serve as concentrated sources of water, ill-controlled paths for erosion, or undesirable air voids prone to local displacement. Maintenance of these drains is therefore essential.

However, effective maintenance is often hampered by the challenge of locating the drains, which may have been installed years prior to the current pavement surface, and thus may be undocumented on as-built drawings, and may have outlets that are visually obscured due to silt build-up and overgrowth of vegetative cover. To this day, the exercise of locating drainage conduits is routinely performed through manual search operations that entail physically walking up and down the slopes of roadway embankments in an effort to find signs of drainage outlets. Given that there are literally tens of thousands of drains associated with a nation's highways, a more rapid method to explore the subsurface beneath pavements has obvious value.

There are several different methods that can be used to detect subsurface features like these drains below pavement, such as Metal Detectors, Electronic Marker Systems (EMS), Electromagnetic Terrain Conductivity, Acoustic Emission, Resistivity, Ground Penetrating Radar (GPR), Microgravitational Techniques, and Seismic Reflection/Refraction methods [1]. Among these, several researchers have demonstrated the potential to locate plastic and clay conduit in agricultural soils [2,3], and assess water presence in/around buried conduits [4] using ground penetrating radar (GPR). Other researchers have successfully utilized GPR in the analysis of materials such as wood, concrete, and asphalt [5–8]. Early detection and evaluation of pipe leaking was also monitored by GPR via microwave tomographic

inversion [9, 10]. Thus, due to the size, geometry, and varying materials employed in most pavement and pavement drainage systems, and the desire to scan extensive lengths of highway with relative speed and ease, GPR tends to offer the greatest potential to facilitate drainage feature detection in subsurface settings and is likely the most commonly employed method used to complement manual drainage conduit detection in practice.

However, successful use of the method is highly dependent upon subsurface conditions, the presence or lack of water in the studied system, the nature of the subsurface target being sought, and its depth. In addition, GPR, despite its potential, has traditionally suffered from several key drawbacks that have limited its use in sub-surface drainage evaluation, such as 1) low GPR image quality in high water content environment and 2) weak GPR reflection signal strength of non-steel targets. Further, effective use of GPR still requires expert data interpretation and traditionally relies upon human visual observations or code driven pattern recognition algorithms that seek the 2-D hyperbolic returns indicative of a buried conduit [11]. Unfortunately, these procedures can still miss many of the older drains beneath pavements (as illustrated below) as they may be partially or fully filled with sediment and/or may be fabricated from clay or other earthen materials, yielding a return signal that is convolved with significant background noise. This work carefully examines the sub-pavement drainage detection scenario by first exploring pavement designs, sources of water in these settings and drainage system performance. This background is then used to assess the relevance of GPR to the detection/evaluation challenges, and GPR simulation and experimentation approaches are determined as means to identify ways to enhance GPR performance for sub-pavement drainage evaluation, leading to hypotheses that are rigorously explored in this thesis.

1.1 Overview of Pavement Systems

1.1.1 Pavement and Subsurface Drainage Systems

A pavement is usually constructed of asphalt or Portland cement concrete, or a layered composite of these materials. An asphalt pavement is referred to as a flexible pavement,

in which a bituminous binder is combined with coarse and fine aggregates. A flexible pavement is typically constructed using Hot Mix Asphalt (HMA) or Warm Mix Asphalt (WMA). A Portland cement concrete pavement (PCCP) is referred to as a rigid pavement. In addition to these two major pavement categories, aggregate pavement is also common, which is constructed with compacted aggregate. The pavement structure is considered to be that part of the road that is placed on the finished sub-grade and encompasses all paved surfaces including shoulders [12]. Figure 1.1 [13] shows typical cross-sections of flexible, rigid, and composite pavements, noting of course that the design of any specific roadway may vary.

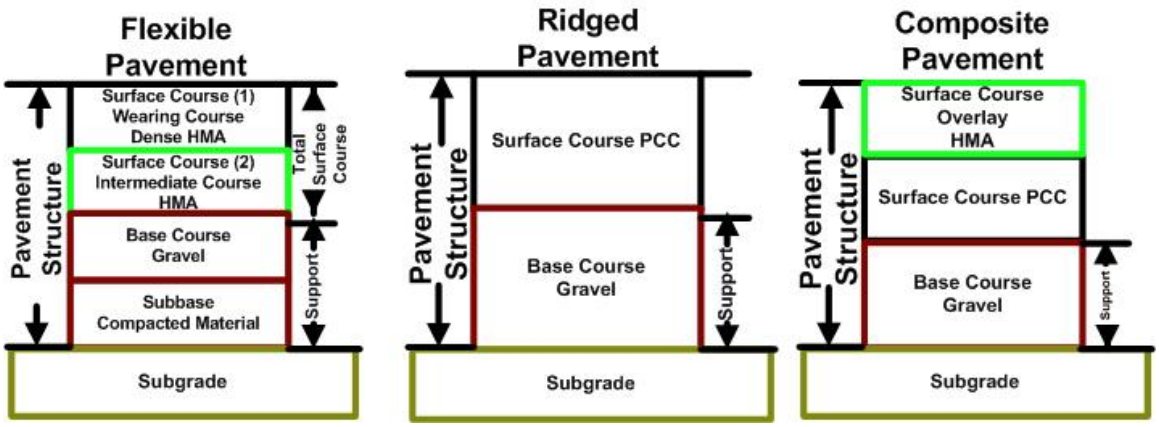

Figure 1.1.: Typical Cross sections of Flexible Pavement (HMA or WMA), Rigid Pavement (PCCP) and Composite pavement

Subsurface drains have been utilized in pavement systems since the 1950s. Transverse subsurface drains were among the first types of subsurface drains to be installed. This type of drain was typically a drain tile or perforated pipe constructed perpendicular to the pavement and spaced longitudinally throughout the project. Beginning in the 1960s, longitudinal pipes were constructed along the edges of the pavement with outlets to side ditches. Little or no maintenance was performed on the subsurface drain systems until a mid-1990s study showed that poor performance of the subsurface drain system was causing failures of pavement structures [12].

Today, subsurface drainage systems in pavement take the form of edge drainage pipes and outlet pipes, which are considered the most important drains in the system, here shown in Figure 1.2 [14]. In the transverse direction, several drainage alternatives can be considered based on design requirements. Hagen and Cochran [15] compared four typical drainage systems and concluded that use of permeable asphalt-stabilized base for the transverse drainable layers usually provided the most effective means to remove water from pavement and provided the driest pavement foundation and the least early pavement distress. Although ideal, this practice is not always followed and thus different designs may be encounter in the field. Nonetheless, several key features tend be be consistent across designs. Figure 1.3 [15] gives a basic view of the different subsurface drainage elements in an example PCC Pavement cross-section [15].

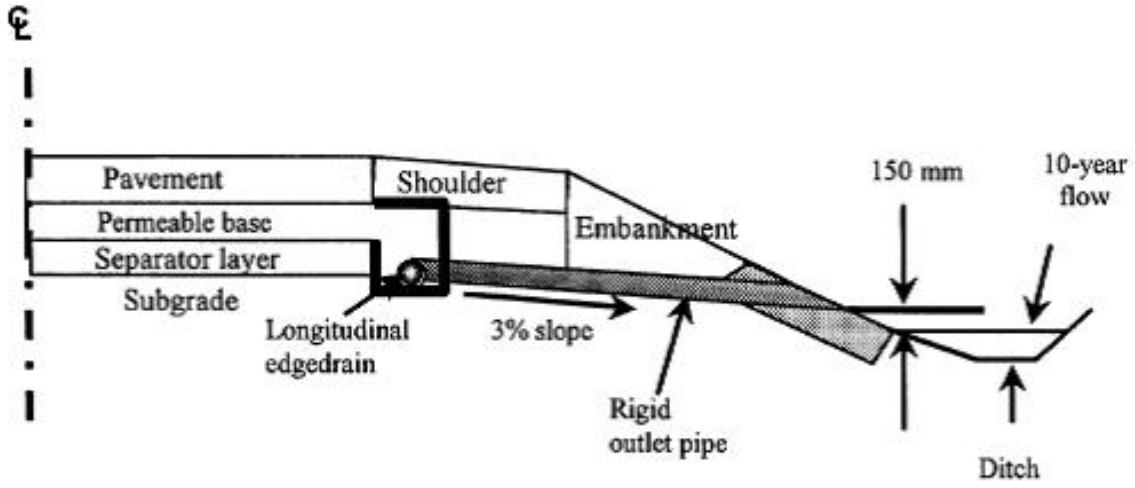

Figure 1.2.: Typical Drainage Systems of Modern Pavements (With Logitudinal Edgedrain and Outlet Pipe)

1.1.2 Water Sources in the Pavement

The majority of water in pavement comes from the surrounding environment, such as rainfall (usually the largest source), snow, dew, melting ice, capillarity from free ground

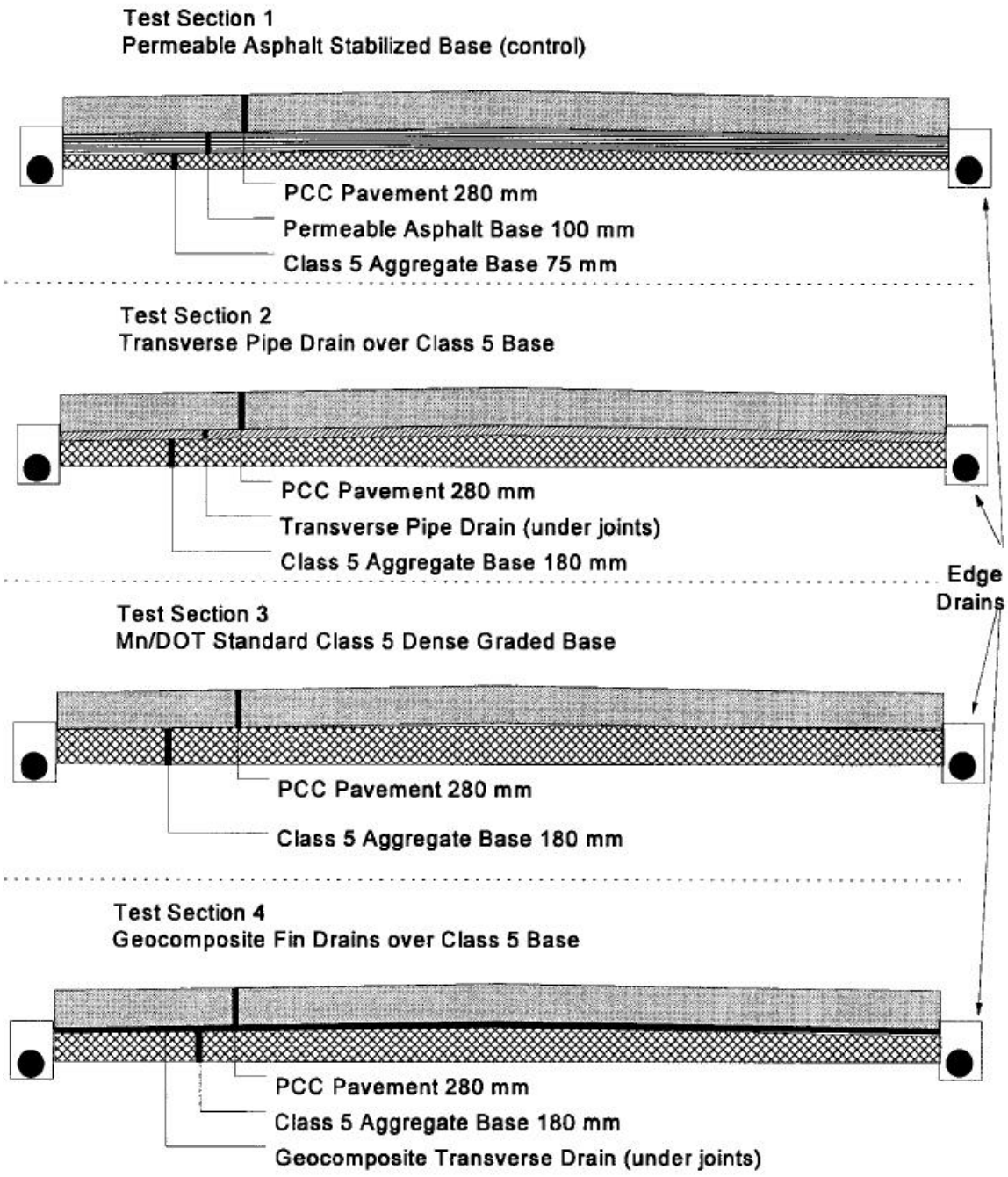

Figure 1.3.: PCC Pavement Drainage Systems

water, and from melting of frozen pavement layers and/or subgrades [16]. Water from the sources mentioned above can enter the pavement structural section in several ways [17]:

1. Cracks and joints in the pavement surface. Normally pavements will develop cracks during their services life.

2. Infiltration through the shoulders and edges of pavement, also side ditches.

3. Melting of an ice layer.

4. Condensation of water vapor, such as dew, generally small amounts.

5. Capillarity from free ground water surface.

This water, which may undergo freeze thaw cycles in cold climates, is typically the source of road damage when sub-pavement drains fail to perform as designed.

1.1.3 Performance of Drainage in Pavement

The reliable design and maintenance of subsurface drains can effectively remove free water and extend the service life of pavement. On the other hand, lack of drainage, and/or a poor sub-base with high fines content can obstruct proper water removal and lead to subsequent pavement damage [18]. It is therefore important to routinely assess drain condition and effectiveness.

Ahmed et al. [19] conducted a study on the performance of existing sub-pavement drainage systems in Indiana. Observations in the study revealed that outlet pipes were frequently exposed for some length or crushed. Outlet markers were not present in the majority of cases, making it difficult to locate the outlets. Vegetation growth around the pipes sometimes blocked the flow completely. Field results were collected for different types of pavements, and the drainage efficiency was reported for these pavements. Figure 1.4 [19] shows a typical hidden outlet pipe. Table 1.1 [16, 20] provides AASHTO criteria to describe the performance of drainage systems.

Subsurface drainage systems are installed for all important highway pavement structural sections. Although considering and constructing a sub-pavement drainage system is important to enable pavement function, maintenance is the key factor related to the

Figure 1.4.: Typical Hidden Outlet Pipe

service life of pavement. Several pavement failures have occurred recently in Indiana which have been attributed to poor drainage conditions (e.g., challenges with clogged sub-pavement outlet drains on I64 in the Seymour District; road patch failure associated with poor drainage on I69 in Fort Wayne; ice formation and related pavement damage caused by poor drainage on I164 in the Vincennes District). The Indiana Department of Transportation (INDOT) has concluded that unmaintained drainage can sometimes lead to worse damage than undrained pavement. Therefore, maintenance of the drainage system is as important as providing the system [21]. In order to fulfill this goal, locating and evaluating the subsurface drainage conduit is the first and the most important problem to be solved.

Table 1.1.: AASHTO Drainage Criteria

Quality of Drainage	**Water Removed Within**
Excellent	2 Hours
Good	1 Day
Fair	1 Week
Poor	1 Month
Very poor	Water will not drain

1.2 Introduction to Ground Penetrating Radar

1.2.1 Introduction

Ground Penetrating Radar offers the potential to address the location and evaluation challenge. GPR is a specific variant of Radar. Radar is an acronym for Radio Detection and Ranging and is based on a simple principle: detecting objects and determining their distances (range) from the echoes they reflect [22]. Radar operates based on the principle of transmitting electromagnetic waves (Tx) and receiving (Rx) reflected signals from any object in their path [23]. Radars transmit either pulsed (most situations) or continuous signals. For pulsed radars the target range is simply determined by the time it takes the pulse of radiated energy to travel to the target and return [24].

Ground Penetrating Radar (GPR) is a high resolution geophysical technique that utilizes electromagnetic radar waves to locate and map subsurface targets, including buried drainage systems. GPR operates by transmitting short pulses of electromagnetic energy into the pavement. These pulses are reflected back to the radar antenna. The amplitude and arrival time are related to the depth of targets and surrounding material properties [13]. GPR can also be called “ground-probing radar,” “sub-surface radar,” or “surface-penetrating radar (SPR)” depending on the application. These specific names refer to a range of electromagnetic techniques designed primarily for the location of objects or interfaces buried beneath the earth’s surface or located within a visually opaque medium [25].

1.2.2 History and Applications of GPR

GPR was first developed in the early 1970's for military applications such as locating underground tunnels. Since then, it has been used in a broad array of applications including locating landmines and unexploded munitions, performing contaminant mapping and ground water analysis, studying glaciers and other ice formations, and carrying out infrastructure and material profiling. Locating underground utilities (in this case drainage systems) is thus only one of many applications for which the technique has been applied.

An overview of peer-reviewed literature related to several primary GPR application areas is presented below, highlighting some of the key insights borrowed from these fields for the work pursued in this research.

Measurements of Soil Properties

Ground Penetrating Radar is well known as an effective non-destructive geophysical method in soil studies, especially for the shallow depths. Zajícová and Chuman [26] provided a detailed review of GPR applications related to soil surveys and studies. One of the most frequent applications of GPR is related to soil water content estimation. To evaluate the soil water content is mainly based on the GPR wave velocity analysis (e.g. [27–32]) and wave inversion techniques (e.g. [33–37]). Besides real-time or short time soil moisture content measurement, investigation of long term soil moisture change is also important and analyzed in several applications, such as railway track-beds condition monitoring [38]. Moreover, Wu et al. [39] developed a drone-borne GPR system to increase the measurement efficiency of soil moisture mapping significantly. Akinsunmade et al. [40] also concluded correlation patterns between soil properties and GPR response in order to well understand the soil types, physical properties and condition of soil disturbances (soil compaction).

Clay content in soils is another important soil property, as it affects the water holding capacity and dielectric properties of soils which can influence geophysical evaluation results significantly, including in GPR applications [41]. Frequency-shift phenomenon are commonly used to evaluate the clay content of the soil by researchers [42–44]. This frequency-

shift effect is also applied to enhance pipe target detection results in this study [45], as will be discussed in detail in Chapter 8.

Besides soils, other researchers have also successfully utilized GPR in the analysis of materials such as wood, concrete, and asphalt (e.g., [5–8]).

Agriculture and Hydro-geophysics

Ground penetrating radar has been used extensively to assess the hydraulic properties of the subsurface that control underground water movement and the spread of chemicals that enter the groundwater system. In this area, multiple researchers have successfully measured hydro-geological properties critical to agriculture and environmental fate and transport at the field scale using GPR (e.g. [46–50]). GPR has also been applied in other aspects of agriculture [51], such as monitoring the movement of agrochemicals [52]; water table depth estimation [53]; mapping the soil spatial variability of agricultural fields [54, 55]; groundwater pollution risk evaluation [56]; quantifying the impact of hydrology on crop production [57]; and detecting produce in cultivated soils [58]. In addition, GPR has been employed in agricultural contexts highly related to this research to detect and locate agricultural drainage pipes [2, 59–64] as well as assess water presence in/around buried conduits [4]. While knowledge of the characteristic signal return patterns from drainage pipes are quite similar to those seen in sub-pavement drainage applications, agricultural conduits are typically located quite close to the ground surface, are often large in dimension, and are buried beneath simple soil strata (vs. multiple pavement layers of varying material properties), making related findings of limited value for the application pursued herein.

Archaeological

As a nondestructive geophysical survey method, ground penetrating radar has multiple advantages in archaeological studies [65–67], and has been used extensively to detect underground structures and buried objects without causing damage. Both 2-D and 3-D GPR surveys are widely employed in archaeology [68–72], with related work encompass-

ing both urban areas [68, 73] and more rural field settings [74, 75]. GPR modeling and simulation are also common in archaeology [76, 77]. In archaeology, archaeologists often employ pattern recognition algorithms [78, 79] to GPR data to search for signals indicative of manufactured rather than naturally occurring subsurface features. This same principle is employed in the background/clutter reduction algorithm employed in this study.

Mine Detection

GPR is widely used for the detection of metallic, plastic, and wooden mines. Several automatic mine detection algorithms have been developed within this application area, including algorithms based on fuzzy logic [80] and systems designed to make use of limited data [81]. Bruschini et al. [82] introduced a combined GPR and metal detector sensor system to increase mine detection accuracy and reduce false alarms when searching for metallic mines. Montoya and Smith [83] introduced a GPR system based on Resistively Loaded Vee Dipoles, which greatly reduced antenna related clutter and enhanced detection sensitivity for antipersonnel mines. Earp et al. [84] performed a study of metallic mine detection effectiveness using an ultrawideband GPR system. Sun and Li [85] introduced a time-frequency analysis technique to detect buried plastic landmines. Beyond these efforts, some of the greatest successes in landmine detection accuracy are a byproduct of digital signal processing (DSP) techniques such as the non-uniform fast Fourier transform (NUFFT) based migration method [86]; the Kalman filter based DSP approach (e.g. [87]); and the hidden Markov models (HMMs) method [88]. Several of these techniques, or their variants, are employed in this work, as detailed in Chapters 5, 6, 7 and 8.

GPR Application in Civil Engineering and Pavement Evaluation

Because of the fast processing and nondestructive nature of ground penetrating radar, it is also widely used in the transportation area and civil engineering applications [89, 90], especially for pavement and bridge evaluations. One of the most common applications is pavement thickness evaluation both during construction and once roads are in service, and

several compact, low cost GPR systems and theoretical analysis models have been developed for this purpose [91, 92]. GPR has also been used to evaluate the nature of the subgrade soil and stratigraphy underlying roadways [93] as well as in-situ density and moisture content in the pavements [94]; to assess pavement quality, through evaluation of pavement layer properties and detection of under-pavement air voids [93, 95, 96]; and to evaluate rail road condition [97]. GPR is also applied to detect and evaluate pavement layer stripping, especially for asphalt concrete pavements [5, 98]. Evaluation of surface and internal cracks in pavements and bridges is another important area of investigation for health monitoring of road and bridge structures [99–101]. Furthermore, more advanced data acquisition approaches have been applied to analyze the structural health of pavement, such as data deep learning techniques [102] and blind test means [103] to locate cavities/voids automatically. Among the many contributions to the technology in this area of application are developments that have enabled successful air coupling of the GPR signal with the roadway which have facilitated non-static tests that make application of the technology to evaluation of extensive highway networks practical from a time and cost perspective.

Underground Utilities and Pipe Detection

Accurate detection and condition evaluation of underground utilities (especially pipes and drainage) is key to help maintain these essential services and avoid unnecessary damage during further construction. The main approaches to fulfill this purpose are acoustic methods [104, 105] and electromagnetic methods, typically ground penetrating radar [106–108]. Being an important research focus of this research, it is helpful to briefly review prior work in this area. Specifically several researchers have explored the application of GPR to underground utility detection and evaluation. Yuan et al. [109] developed a drop-flow method to identify the features of GPR hyperbola signals of underground utilities (pipes) to estimate their complex spatial configurations, sizes and locations. Li et al. [110] introduced data interpretation method to estimate the depth and orientation of buried utilities based

on GPR and GPS data. Curioni et al. [111] analyzed the effects of seasonal variations and influences on utility detection by GPR in a sandy soil.

Pipe and drainage detection and mapping is the major problem in utility detection applications, and there has been a great deal of research in this area. In order to locate pipes by GPR, several different approaches have been applied, such as ultra-wide-band GPR hardware modification [112] and point coordinates extraction data processing [113]. Moreover, Koganti et al. [114] evaluated the GPR detection features of subsurface drainage mapping surveys based on different survey configurations and site conditions; Zhao and Al-Qadi [115] specifically introduced a GPR imaging reconstruction method by FDTD modeling to analyze the conditions of under pavement drainage pipes.

The two major materials of underground pipes and drainage are metal and plastic. As a result, the characteristics of GPR reflection signals based on these two types of materials have been explored by numerous researchers. Meschino et al. [108] and Frezza et al. [116] focused on metallic target detection approaches; on the other hand, Zhang et al. [117] and Ayala-Cabrera et al. [118] focused on plastic pipes detection by time-frequency methods; Ni et al. [119] introduced a discrete wavelet transform GPR signal processing method to analyze the detection features for both PVC and metal pipes and compared the signal differences; Prego et al. [120] designed a site experiment to interpret GPR detection data features based on several possible configurations of multiple buried pipes, including different depths, materials (PUR, PVC, DI, PP, PA, Concrete) and proximity or overlapping in both horizontal and vertical directions.

Besides the location detection of pipes, GPR has also been applied to evaluate different pipeline faults, like blockage and leakage [121, 122]. Lai et al. [123] and Cheung and Lai [122] mapped water-pipe leakage conditions by GPR wave velocity analysis; Atef et al. [124] detected water leaks through a combination of GPR imaging and IR imaging. Ocaña-Levario et al. [125] introduced an advanced approach to locate water leaks by applying variance filters and multi-agent system analysis.

The above outlined studies highlight the potential to employ GPR for sub-pavement drainage detection, specifically calling attention to equipment modifications and digital signal processing techniques that could improve GPR results in the sub-pavement setting.

1.2.3 Overview of Controlled Lab and Field GPR Experimentation

Controlled Lab and field (site) experiments are an efficient means to simulate real situations in the natural field condition and a way to test possible solutions. Several researchers have pursued lab or field experiments to simulate problems similar to the challenge pursued herein in various GPR application areas. In particular, several researchers have successfully performed experiments that each lend valuable input into potential solutions to the challenge of sub-surface drainage evaluation:

Among all the environment factors listed above, soil type and its degree of saturation are among the most important elements which can strongly influence results of GPR studies. Clay dominated soil, which frequently contains some amount of water, is considered to be the most challenging problem if it appears in detection areas. Johnson and Poeter [126] set up a lab experiment in a sand tank with saturated clay layers using a GPR system to track a dense non–aqueous phase liquid (DNAPL) injection. A 1.5GHz GPR antenna was used in this experiment. Based on the results they presented, several steel plates and pipes buried in these clay layers were detected using their GPR system, which provided evidence that metal objects buried in clay may be detected using certain specific GPR designs.

Siriwardane et al. [127] developed a lab experiment to detect the water level in a silty soil sample during seepage under transient conditions using GPR. This work provides insight into the appropriate dimensions for an effective in-laboratory test setup, highlights the design of a test tank in which water levels can be controlled, and also demonstrates the potential for GPR to be employed in environments involving both clay and water.

Yigit et al. [128] established a laboratory scale experiment to detect several buried objects based on the classical B-scan ground penetrating radar imagery using a synthetic aperture radar (SAR) focusing algorithm. Simulation and experimental results employing

an air launched signal presented in the article demonstrate that centimeter scale objects (4-6 cm) could be detected in heterogeneous soils when employing a GPR system with a SAR based focusing algorithm.

Zhang et al. [117] designed a lab wooden box experiment to focus on detection of RF tagged buried plastic pipes by GPR. With designed higher frequency RF tags pre-installed on the pipe walls, this study proposed a simple approach to enhance the utilities detection visibility in both time and frequency domains, especially big frequency shifts.

Besides the lab scale GPR experiments studies discussed above, there have been many other related GPR lab experiments that are relevant to this work herein, such as laboratory measurements of subsurface moisture content [27, 129]; clay content estimation [44]; pipe leakage evaluation [123, 125].

The scale of laboratory experiments, most of the time, cannot simulate the entire complex surrounding conditions of the natural filed environment. So, the lab test results of GPR commonly have some limitations and variation of results may be observed when in the field. Consequently, controlled field scale experiments often become necessary in most GPR studies.

In order to establish efficient GPR data acquisition approaches to detect underground pipes, Prego et al. [120] constructed an asphalt paved field experiment site, $14 \times 1m$ in size, with 75 cm of sub-base course, 10 cm of intermediate course and 5 cm of surface course. There were 38 different types of pipes installed separately or aliased on this site with the diameter from 24 to 315 mm (e.g. polyurethane, PVC, DI). Different frequency GPR antennas and different survey directions were also evaluated. This study analyzed and concluded the vertical and horizontal spatial resolutions and pipe reflection signal signatures under various experimental combinations.

Besides pipe detection, field experiments have also been performed to other common GPR applications. Cheung et and Lai [122] designed a full scale ($20mlong \times 10mwide$) field experimental set up to evaluate iron water pipe leakage conditions. This field site was paved with reinforced concrete and pavement bricks in order to analyze the different GPR signal features. The entire study was based on the GPR wave velocity analysis of different

frequency GPR antennas in order to determine the location of upward/downward spreading water leakages. Moreover, this full scale field site were also designed to detect underground voids or cavities using a blind test approach [103].

Furthermore, Ercoli et al. [27] studied GPR water content measures of sandy soils by both laboratory and field scale experiments. After laboratory experiments on two types of sandy soils, and development of basic water content data acquisition models and approaches, an in-situ field (area of $6m \times 3m$) GPR survey was carried out to validate the data processing method and compare the results of both lab and field experiments. This study yielded a calibrated model for water content estimation by GPR.

In summary, controlled or known condition lab and field experiments are widely used in GPR related research in order to establish efficient hardware/software problem solving approaches. This approach will also be employed to inform the work herein.

The general problem statement and hypotheses of this thesis are introduced in the following sections.

1.3 Problem Statement

As introduced above, locating and evaluating the condition of existing subsurface drainage systems is a key factor to enable proper maintenance and increase the service life of pavement. While there are several different methods that can be used to detect objects in subsurface settings, such as metal detectors, electronic marker systems, acoustic emission sensing, resistivity measurements, micro-gravitational techniques and seismic reflection/refraction methods [1]. Enhanced, this thesis particularly focused on the method of ground penetrating radar (GPR), a near surface nondestructive geophysical technique.

As detailed above, a number of researchers have already demonstrated the potential to locate metallic/plastic pipes and clay conduit in both agricultural fields (e.g., [2, 3, 59–64]) and pavement drainage pipes evaluations (e.g., [108, 112, 115–120]). However, routine success in use of the method is highly dependent upon subsurface conditions, the presence or lack of water, the nature of the subsurface target being sought, and its depth. Thus, effec-

tive and practical use of GPR still requires advances in data interpretation and hardware configuration design. Overcoming these challenges is the focus of this research.

1.4 Hypotheses and Problem Solving Approaches

1.4.1 Research Hypotheses

In order to enhance the GPR detection accuracy of under pavement pipes, the surrounding conditions of potential targets and the GPR hardware features need to be well considered and analyzed. A few of research hypotheses have been established to consider in this thesis, as follows:

Hypothesis 1

Question: What parameters of the field environment affect GPR detection significantly?

Hypothesis: A number of parameters could affect GPR field surveys, such as target (pipe) materials/size, water content of surrounding soils, clay conditions, pavement structural types, pipe installation differences and antenna operating frequencies.

Prediction: To analyze the above parameters, a group of computer-based simulations and related laboratory experiments is a valuable approach to help fully understand the influence of these key factors prior to the next research step. In Chapter 4 and 5, groups of simulations are designed and performed to predict the effect of several critical parameters on GPR applications.

Hypothesis 2

Question: What possible signal processing approach could enhance the potential target signal strength when it is at the same level as background clutter and noise, or even lower?

Hypothesis: When the material of a potential target is nonmetallic, such as PVC pipes, and the surrounding conditions involve moisture and silty/clay soils, the refection signals of

the potential target may not be clearly shown in the GPR signals. However, weakened target reflection signals should still be received by the receiver antenna, but will be hidden by the background noise and clutter signals. An advanced background noise removal method could possibly enhance the weak target signals.

Prediction: Statistical analysis of the GPR signal and use of noise/clutter reduction techniques will make it possible to extract the weak target signals. Specifically, the main targets in this research are under-pavement pipes, which are well designed and systematically constructed. Thus, for a certain length of survey, the conditions under the pavement could be considered "uniform". To take advantage of this, an improved moving window background noise reduction algorithm is developed to enhance possible targets based on statistical analysis. In Chapter 6, the details of this approach are introduced. Furthermore, in Chapter 7, a pattern recognition method is also introduced to improve the contrast level of GPR observations and thus further enhance potential targets.

Hypothesis 3

Question: Is there any hardware/antenna modification that could improve the GPR detection results, such as multi-antenna and multi-frequency antenna configurations?

Hypothesis: An antenna's frequency, polarization, offset (distance between Transmitter (Tx) and Receiver (Rx)) and survey direction are key factors that dominate GPR detection results. Different combinations of GPR antennas can lead to varying results. Furthermore, the central frequency of transmitted GPR waves will shift to lower frequencies when traveling trough under-pavement materials. As a result, the survey configuration of higher frequency Transmitters (Tx) with lower frequency Receivers (Rx) may improve/enhance the potential target reflection signals.

Prediction: The frequency of an antenna determines the resolution and transmission depth of radio waves. The use of different Tx and Rx GPR frequency antennas can maximize the possibility of successful detection. The frequency-shift phenomenon of GPR transmitting signals has been observed by several researchers, as shown in the previous

background sections. In order to take advantage of this fact, necessary modifications of GPR antenna configurations are applied in this research to improve the energy of received GPR signals. The details of this approach are introduced in Chapter 8.

1.4.2 Introduction of Problem Solving Approaches

As discussed above, successful detection of under-pavement pipes/drainage based on GPR still needs further analysis and research. Moreover, based on the hypotheses and predictions established in section 1.4.1 and past related research works introduced in section 1.2.2 and 1.2.3, the brief problem solving approaches employed in this thesis are shown in Fig 1.5. As designed, in-situ field tests on known targets will be the main technique employed herein to pursue and evaluate possible GPR detection improvements of under-pavement drainage. Small-scale and full-scale laboratory experiments, of course, have also been designed to verify suggested methodologies, for both hardware and software (signal processing) based techniques. The detailed research approach and key factors affecting the experiment design will be discussed in Chapter 4.

1.5 Objectives and Scope

Given the above background, the objective of the research herein was to explore the above stated opportunities to improve ground penetrating radar technology to enable rapid location of subsurface drainage features in pavements and thus alleviate some of the cost and complexity of maintaining these systems. To this end, this research study encompassed the following activities:

1. Performance of a literature review to develop a thorough understanding of the current state of knowledge on GPR applicability to sub-pavement drainage feature assessment (presented above).

2. Definition of the set of physical parameters that characterize sub-pavement drainage systems in field settings likely to be encountered throughout Indiana.

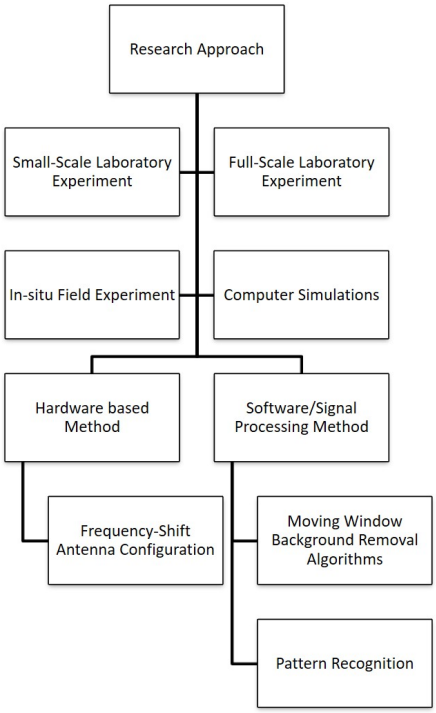

Figure 1.5.: Overview of Problem Solving Approaches Pursued in this Research

3. Identification and acquisition of commercially available equipment to enable in-lab and in-field experimentation techniques and with modified equipment configurations with the potential to enhance drainage system detection success.

4. Application of GPR simulation tools to inexpensively and rapidly evaluate alternate GPR test configurations.

5. Design, fabrication, and application of a laboratory based experiment to enable proof testing of the enhanced/modified GPR system under controlled testing conditions.

6. Development and/or application of unique signal processing techniques to enhance drainage system detection sensitivity.

7. Performance of in-laboratory and in-field tests on simulated and/or actual road segments of known cross-section to assess GPR system performance under representative working conditions.

8. Analysis and synthesis of all findings to develop relevant conclusions.

9. Translation of the findings into an implementation plan for future routine application, where appropriate.

1.6 Organization

This thesis is aimed to provide readers with the background on ground penetrating radar in the application of underground-pipe detection as well as the improved algorithms and result analysis of background reduction and target detection theory.

This chapter provides general background on the designed and challenge of the pavement drainage systems, history of ground penetrating radar development and an overview of research in related GPR application areas.

Chapter 2 provides theories involved in ground penetrating radar detection, such as electromagnetic theory, digital signal processing, basic radar theory and detection theory.

Chapter 3 introduces the main GPR equipment used in this research as well as the standard procedures of typical GPR data collection.

Chapter 4 outlines the general research approaches pursued in this work, including computer based simulations and digital signal processing methods as well as hardware configuration modification approaches, which all involved lab and field tests.

Chapter 5 provides a group of theoretical simulations to analyze the effect of GPR antenna configuration differences on pipe target detection. Furthermore, a basic/simple background noise reduction analysis is applied to the simulated GPR results in order to explore the possibilities of improvements in GPR detection success rate that could be achieved through modified/improved background signal reduction algorithms in the following chapters.

Chapter 6 introduces the first digital signal processing method - an improved background signal reduction approach as well as related theory to enhance the underground pipe detection success rate. This approach is based on a moving window background re-

duction algorithm and a probabilities analyzing method, which converts 2D GPR images into 1D output to show potential target locations.

Chapter 7 introduces the second digital signal processing approach to further refine the detection success rate of a GPR survey. This method is based on a pattern recognition image processing method, which improves the contrast of GPR images in order to identify more readily targets.

Chapter 8 delves more deeply into antenna theory and introduces an alternative GPR antenna configuration based on the frequency-shift phenomenon to improve the detection success of the GPR method. This method is based on GPR antenna modification/combination to take advantage of the frequency-shift that occurs when GPR radio waves are transmitted in underground materials.

Chapter 9 provides the conclusions and future research recommendations for under-pavement pipe detection using Ground Penetrating Radar (GPR).

2. THEORY

2.1 Introduction

The following sections provide fundamental background on the theory employed throughout this effort, covering core concepts of electromagnetic waves, material interactions involving EM waves, and related concepts of GPR.

2.2 Electromagnetic Wave Properties

2.2.1 Overview of Electromagnetic Theory

Ground Penetrating Radar is fundamentally established on electromagnetic theory. Maxwell's equations mathematically describe the physics of EM fields, while constitutive relationships quantify material properties. Combining the two provides the foundations for quantitatively describing GPR signals. [130, 131]

Maxwell's Equations In mathematical terms, EM fields and relationships are expressed as follows:

$$\bigtriangledown \times \vec{E} = -\frac{\partial \vec{b}}{\partial t} \tag{2.1}$$

$$\bigtriangledown \times \vec{H} = \vec{J} + \frac{\partial \vec{d}}{\partial t} \tag{2.2}$$

$$\bigtriangledown \bullet \vec{D} = \rho \tag{2.3}$$

and

$$\bigtriangledown \bullet \vec{B} = 0 \tag{2.4}$$

where

$\vec{E}$ = electric field strength vector (V/m)

$\vec{B}$ = magnetic flux density vector (T)

$\vec{D}$ = electric displacement vector (C/m^2)

$\vec{H}$ = magnetic field intensity (A/m)

ρ = electric charge density (C/m^2)

$\vec{J}$ = electric current density vector (A/m^2)

t = time (s)

Constitutive Equations Constitutive relations are the means of relating the material physical properties to the electromagnetic fields. For GPR, the electrical and magnetic properties are of importance. And there are three quantities must be used for GPR:

- Electrical conductivity $\tilde{\sigma}$,

$$\vec{J} = \tilde{\sigma}\vec{E}, \tag{2.5}$$

- Dielectric permittivity $\tilde{\epsilon}$,

$$\vec{D} = \tilde{\epsilon}\vec{E} \tag{2.6}$$

- Magnetic permeability $\tilde{\mu}$,

$$\vec{B} = \tilde{\mu}\vec{H} \tag{2.7}$$

where

$\vec{E}$ = electric field strength vector (V/m)

$\vec{B}$ = magnetic flux density vector (T)

$\vec{D}$ = electric displacement vector (C/m^2)

$\vec{H}$ = magnetic field intensity (A/m)

$\vec{J}$ = electric current density vector (A/m^2)

$\tilde{\sigma}$ is electrical conductivity, which characterizes free charge movement when an electric field is present;

$\tilde{\epsilon}$ is dielectric permittivity, which characterizes displacement of charge constrained in a material structure to the presence of an electric field;

$\tilde{\mu}$ is magnetic permeability, which describes how intrinsic atomic and molecular magnetic moments respond to a magnetic field.

Followed by A.P.Annon [130], in GPR applications, the properties of introduced factors are dependent upon the history of the incident field. As a result, the fully correct expressions of the equations (2.5), (2.6) and (2.7) should be formed as follows:

$$\vec{J} = \int_0^\infty \tilde{\sigma(\beta)} \cdot E(\vec{t - \beta})d\beta \tag{2.8}$$

$$\vec{D} = \int_0^\infty \tilde{\epsilon(\beta)} \cdot E(\vec{t - \beta})d\beta \tag{2.9}$$

$$\vec{B} = \int_0^\infty \tilde{\mu(\beta)} \cdot H(\vec{t - \beta})d\beta \tag{2.10}$$

where

β expresses the incident field travel distance.

The more complex expressions above must be applied when frequency dependent (dispersive) material properties need to be considered. In most of GPR applications, the scalar constant form of σ, ϵ, μ is considered. The dielectric permittivity ϵ is considered as a very

important quantity for GPR. For most cases, the terms relative permittivity or "dielectric constant" are used and defined as follows:

$$\epsilon_r = \frac{\epsilon}{\epsilon_0} \tag{2.11}$$

where

ϵ_r is the relative permittivity (dielectric constant) of materials.

ϵ is the absolute permittivity of materials.

ϵ_0 is the permittivity of vacuum, which is about $8.89 \times 10^{-12} F/m$.

2.2.2 Wave Natural and Sinusoidally Time-varying Fields

Ground penetrating radar exploits the wave character of EM fields. The wave character becomes evident when Maxwell's equations are rewritten to eliminate either the electric or the magnetic field. [131] Using the electric field, rewriting yields the transverse vector wave equation

$$\vec{\Delta} \times \vec{\Delta} \times \vec{E} + \mu\sigma \cdot \frac{\partial \vec{E}}{\partial t} + \mu\epsilon \cdot \frac{\partial^2 \vec{E}}{\partial t^2} = 0 \tag{2.12}$$

in which the terms B and C are defined as follows:

$$B = \mu\sigma \cdot \frac{\partial \vec{E}}{\partial t}$$

$$C = \mu\epsilon \cdot \frac{\partial^2 \vec{E}}{\partial t^2}$$

Ground penetrating radar is effective in low-loss materials where energy dissipation (term B) is small compared to energy storage (term C). With GPR, the electric field is the field normally measured and it has the following form:

$$\vec{E} = f\left(\vec{r} \cdot \vec{k}, t\right) \hat{\mu} \tag{2.13}$$

where $\vec{r}$ is a vector describes the spatial position and $f\left(\vec{r}\cdot\hat{k},t\right)$ satisfies the scalar equation

$$\frac{\partial^2}{\partial\beta^2}f\left(\beta,t\right)-\mu\sigma\frac{\partial}{\partial t}f\left(\beta,t\right)-\mu\epsilon\frac{\partial^2}{\partial t^2}f\left(\beta,t\right)\equiv 0 \tag{2.14}$$

where $\beta=\vec{r}\cdot\hat{k}$ is the distance in the propagation direction.

While in low-loss conditions

$$f\left(\beta,t\right)\approx f\left(\beta\pm vt\right)e^{\mp\alpha\beta} \tag{2.15}$$

where velocity v is expressed as

$$v=\frac{1}{\sqrt{\epsilon\mu}} \tag{2.16}$$

and attenuation α is expressed as

$$\alpha=\frac{1}{2}\sigma\sqrt{\frac{\mu}{\epsilon}} \tag{2.17}$$

The EM field normally propagates as spatially damped waves when electrical losses are small. The signal amplitude decays exponentially in the direction of field translation, the β direction, and the decaying rate is normally expressed as $e^{-\alpha\beta}$, shown in the following figure 2.1.

In many cases, discussions are given in terms of sinusoidal excitation with angular frequency ω, in this form

$$f\left(\beta,t\right)=Aexp\left(-\left(i\left(\frac{\beta}{v}-\omega t\right)\right)\right)e^{-\alpha\beta} \tag{2.18}$$

where A is the peak signal amplitude.

Sinusoidal signals are characterized by both excitation ω and spatial wavelength λ, where $\lambda=2\pi v/\omega$.

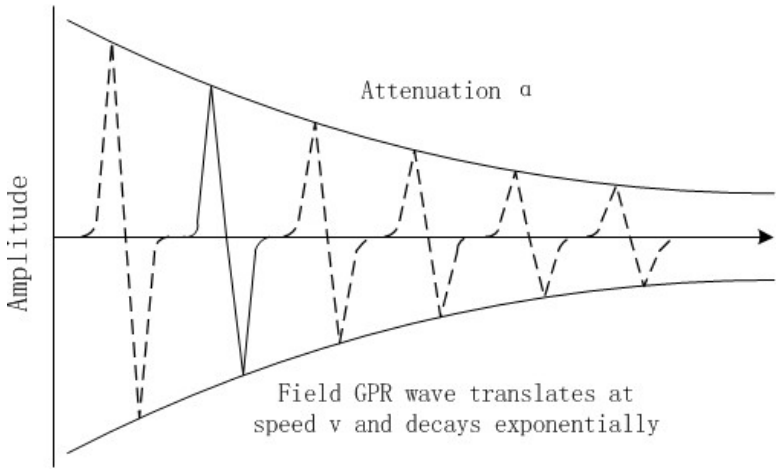

Figure 2.1.: Illustrative of GPR wave translation and exponential decay in field, Attenuation rate α

2.2.3 Snell's Law and Fresnel Reflection Coefficients

Ground penetrating radar methods normally depend on detection of reflected or scattered signal. "GPR method involves directing an electromagnetic radio energy (radar) pulse into the subsurface, followed by measurement of the elapsed time taken by the signal as it is travels downwards from the transmitting antenna, partially reflects off a buried feature, and is eventually returned to the surface, where it is picked up by a receiving antenna. Reflections from different depths produce a signal trace, which is a function of radar wave amplitude (and energy) versus time." [64, 132]

The signal is generated by a radar transmitter and should flow according to the basic wave transmission law, known as Snell's law. Snell's law expresses how wave fronts change direction and propagation amplitude changes as the waves move through different materials, where the travel velocity is not constant.

Snell's law can be expressed as the following equation.

$$\frac{sin\theta_1}{v_1} = \frac{sin\theta_2}{v_2} \tag{2.19}$$

This rule must be applied at each boundary of different materials and the wave-front or rays must bend or change direction at each interface. When a plane EM wave impinges

on a interface or boundary, it is partially transmitted and partially reflected. The Fresnel reflection and transmission coefficients provided the quantified equations to show how the amplitudes of the EM fields vary across an interface between two materials [133]. The Figure 2.2 shows the illustrative of both Snell's law and Fresnel reflection and transmission coefficients. And the incident, reflected and transmitted field strengths are expressed with the following equation:

$$I + R \cdot I = T \cdot I \tag{2.20}$$

Where R is the reflection coefficient, while T is the transmission coefficient.

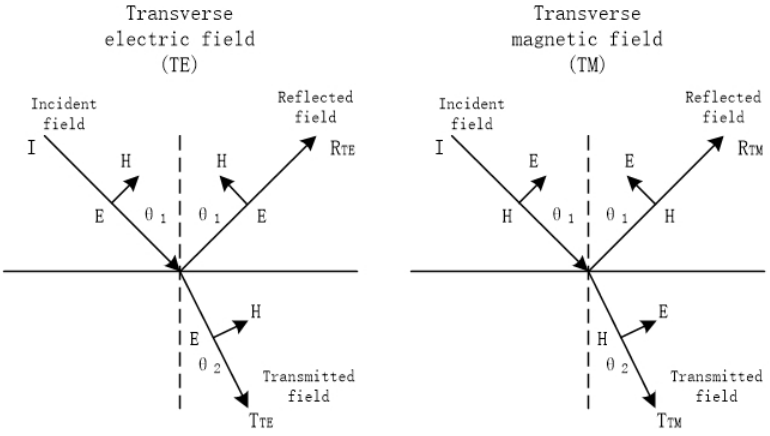

Figure 2.2.: Snell's Law and Fresnel coefficients

For transverse electric field (TE) and transverse magnetic field (TM), the results can be shown as:

$$R_{TE} = \frac{Y_1 \cdot cos\theta_1 - Y_2 \cdot cos\theta_2}{Y_1 \cdot cos\theta_1 + Y_2 \cdot cos\theta_2} \tag{2.21}$$

$$T_{TM} = \frac{Z_1 \cdot cos\theta_1 - Z_2 \cdot cos\theta_2}{Z_1 \cdot cos\theta_1 + Z_2 \cdot cos\theta_2} \tag{2.22}$$

and

$$T_{TE} = 1 + R_{TE} = \frac{2Y_1 cos\theta_1}{Y_1 \cdot cos\theta_1 + Y_2 \cdot cos\theta_2} \tag{2.23}$$

$$T_{TM} = 1 + R_{TM} = \frac{2Z_1 cos\theta_1}{Z_1 \cdot cos\theta_1 + Z_2 \cdot cos\theta_2} \tag{2.24}$$

where Z and Y are the impedances and admittances, the relation between them can be written as $Y = 1/Z$. The critical factor is that an EM impedance contrast must exist for there to be a response.

2.3 Material Properties and Wave Properties

2.3.1 Relative Permittivity and Wave Velocity

Ground penetrating radar is most useful in low-electrical-loss materials. If $\sigma = 0$, GPR would see very broad use since signals would penetrate to great depth. However, clay-rich environments or areas of groundwater can create conditions where GPR signal penetration is very limited. Table 2.1 shows some materials' dielectric constants (relative permittivity) and wave velocities [134].

As introduced in the previous sections, the velocity an EM wave travels in a material can be expressed as equation (2.16) $v = 1/\sqrt{\mu\epsilon}$.

As a result, the velocity of light (wave) in free space is

$$c = \frac{1}{\sqrt{\mu_0 \epsilon_0}} = 3 \times 10^8 m/s \tag{2.25}$$

where

μ_0 is the absolute magnetic susceptibility of free space, $\mu_0 = 1.26 \times 10^{-6} Hm^{-1}$

ϵ_0 is the absolute electric permittivity of free space, $\epsilon_0 = 8.86 \times 10^{-6} Fm^{-1}$

μ is the absolute magnetic susceptibility of medium, $\mu = \mu_0 \mu_r$

ϵ is the absolute electric permittivity of medium, $\epsilon = \epsilon_0 \epsilon_r$

Table 2.1.: Dielectric constant, wave velocity and wavelength at 400MHz central frequency of common subsurface media

Material	**Dielectric Constant** ϵ_r	**Wave Velocity** (m/ns)	**Wavelength (@400MHz)** (m)
Air	1	0.3	0.75
Water	81	0.033	0.0825
Rocks	4-12	0.15-0.087	0.375-0.2175
Sand dry	3-5	0.15-0.12	0.375-0.3
Sand wet	20-30	0.055	0.1375
Clay dry	2-6	0.11-0.09	0.275-0.225
Clay wet	15-40	0.052	0.13
Concrete	9-12	0.10-0.087	0.25-0.2175
Asphalt	3-6	0.17-0.12	0.425-0.3
Silty Clay	6.0	0.12	0.3
PVC plastic	3.3	0.16	0.4
Fiberglass	4.8	0.14	0.35
Metal	300	0.017	0.0425
Gasoline	1.94	0.22	0.55
Benzene	2.28	0.2	0.5
Methanol	32.6	0.052	0.13
DNAPL	2.3	0.19	0.475

and the relative permittivity, also known as dielectric constant

$$\epsilon_r = \frac{\epsilon}{\epsilon_0} \tag{2.26}$$

has a value in the range 1 to 80 for most geological materials [25],

and the relative magnetic susceptibility

$$\mu_r = \frac{\mu}{\mu_0} \tag{2.27}$$

is 1 for non-magnetic geologic materials. ($\mu_r = 1$)

Then, the EM wave velocity in a non-magnetic medium is given approximately by the following formula [25, 135, 136].

$$v = \frac{c}{\sqrt{\epsilon_r}} \tag{2.28}$$

And the wavelength λ is calculated as

$$\lambda = \frac{v}{f} \tag{2.29}$$

where

λ is the wavelength when travelling in a medium (m)

v is the wave velocity when travelling in a medium (m/s)

f is the center frequency of the wave (Hz)

For most dry geological materials, such as sand and gravel, the dielectric constant (relative permittivity) generally varies roughly in the range $3 \leq \epsilon_r \leq 8$. Water has an an anomalously large value of dielectric constant, $\epsilon_r \sim 81$, due to the high polarizability of the water molecule in the presence of an applied electric field.

As a result, the high water content soils, such as clay, have significantly higher dielectric constant values, $\epsilon_r \sim 15 - 40$, than the dry soils, $\epsilon_r \sim 3 - 6$.

2.3.2 Material Impedance and Attenuation

General Concept For GPR applications involving subsurface pipes and utilities, the operating frequency normally falls into $300MHz$ to $1GHz$. Generally, the electromagnetic radiation propagates as waves through the medium at high frequencies. All frequency components travel at the same velocity and suffer the same attenuation. An impulse signal will travel with its shape intact [130]. Table 2.2 shows some materials' electrical conductivity and attenuation values of Common Geomaterials measured at an antenna frequency of 100MHz [25].

Table 2.2.: Electrical Conductivity and Attenuation values of Common Geomaterials measured at an antenna frequency of 100MHz

Material	**Electrical Conductivity** (S/m)	**Attenuation** (dB/m)	**Dielectric Constant** ϵ_r
Air	0	0	1
Asphalt dry	$10^{-2} : 10^{-1}$	2-15	2-4
Asphalt wet	$10^{-3} : 10{-}1$	2-20	6-12
Clay dry	$10^{-1} : 10^{-0}$	10-50	2-6
Clay wet	$10^{-1} : 10^{-0}$	20-100	5-40
Coal dry	$10^{-3} : 10^{-2}$	1-10	3.5
Coal wet	$10^{-3} : l0^{-1}$	2-20	8
Concrete dry	$10^{-3} : 10^{-2}$	2-12	4-10
Concrete wet	$10^{-2} : 10^{-1}$	10-25	10-20
Freshwater	$10^{-6} : 10^{-2}$	0.01	81
Freshwater ice	$10^{-4} : 10^{-3}$	0.1-2	4
Granite dry	$10^{-8} : 10^{-6}$	0.5-3	5
Granite wet	$10^{-3} : 10^{-2}$	2-5	7
Limestone dry	$10^{-8} : 10{-}6$	0.5-10	7
Limestone wet	$10^{-2} : 10^{-1}$	1-20	8
Permafrost	$10^{-5} : 10^{-2}$	0.1-5	4-8
Rock salt dry	$10^{-4} : 10^{-2}$	0.01-1	4-7
Sand dry	$10^{-7} : 10^{-3}$	0.01-1	2-6
Sand wet	$10^{-3} : 10^{-2}$	0.5-5	10-30
Sandstone dry	$10^{-6} : 10^{-5}$	2-10	2-5
Sandstone wet	$10{-}4 : 10^{-2}$	4-20	5-10
Sea water	10^{2}	100	81
Sea-water ice	$10^{-2} : l0^{-1}$	1-30	4-8
Shale dry	$10^{-3} : 10^{-2}$	1-10	4-9
Shale saturated	$10^{-3} : 10^{-1}$	5-30	9-16
Snow firm	$10^{-6} : 10^{-5}$	0.1-2	6-12
Soil clay dry	$10^{-2} : 10^{-1}$	0.3-3	4-10
Soil clay wet	$10^{-3} : 10^{-0}$	5-50	10-30
Soil loamy dry	$10^{-4} : 10^{-3}$	0.5-3	4-10
Soil loamy wet	$10^{-2} : 10^{-1}$	1-6	10-30
Soil sandy dry	$10^{-4} : 10^{-2}$	0.1-2	4-10
Soil sandy wet	$10^{-2} : 10^{-1}$	1-5	10-30

In this case, the impedance of material Z can be formed as

$$Z = \sqrt{\frac{\mu}{\epsilon}} = \frac{Z_0}{\sqrt{\epsilon}} \tag{2.30}$$

where

Z_0 is the impedance of free space

$$Z_0 = \sqrt{\frac{\mu_0}{\epsilon_0}} = 377ohms \tag{2.31}$$

To simplify the above equation, the impedance can also be expressed as

$$Z = \frac{c}{v} = \sqrt{\mu_r \epsilon_r} Z = \sqrt{\frac{\mu_0 \mu_r}{\epsilon_0 \epsilon_r}} = \sqrt{\mu_r \epsilon_r} \tag{2.32}$$

taking $\mu_r = 1$ as mentioned above, the impedance Z can finally be formed as

$$Z = \sqrt{\epsilon_r} \tag{2.33}$$

Attenuation α in this case can be generated as:

$$\alpha = \sqrt{\frac{\mu}{\epsilon}} \cdot \frac{\sigma}{2} = Z_0 \cdot \frac{\sigma}{2 \cdot \sqrt{\epsilon}} \tag{2.34}$$

Then, according to Annan (1992) [137] and Jol (1995) [138], the attenuation of a GPR wave can be given approximately by the following formula:

$$\alpha = 1.69 \frac{\sigma}{\sqrt{\epsilon_r}} (dB/m) \tag{2.35}$$

where σ is the conductivity value of the medium.

Multi-Layer Reflection At the boundary between two media, some energy will be reflected and the remaining energy will be transmitted into the next layer. The reflection field strength field is described by the reflection coefficient R.

$$R = \frac{Z_2 - Z_1}{Z_2 + Z_1} \tag{2.36}$$

where Z_1 and Z_2 are the impedances of medium 1 and 2.

In a nonconducting medium, such as dry soil or dry concrete, only a single frequency of radiation is considered. The reflection coefficient for a normally incident radar wave can be simplified from the the above equation and rewritten as

$$R = \frac{\sqrt{\epsilon_{r2}} - \sqrt{\epsilon_{r1}}}{\sqrt{\epsilon_{r2}} + \sqrt{\epsilon_{r1}}} \tag{2.37}$$

where ϵ_{r1} and ϵ_{r2} are the relative permittivity of medium 1 and 2.

The reflected energy is proportional to R^2. The reflected coefficient has a positive value when $\epsilon_{r2} > \epsilon_{r1}$, such as where an air-filled void exists void exists in a dielectric material. The effect on a pulse waveform is to change the phase of the reflected wavelet so that targets with different relative dielectric constants to the host material show different phase patterns of the reflected signal. However, the amplitude of the reflected signal is affected by the propagation dielectric of the host material, the geometric characteristics of the target and its dielectric parameters. [25] The following table 2.3 lists some common interfaces of GPR applications and the material properties at the boundary. ϵ_{ri} is the relative permittivity (dielectric constant) of i_{th} layer of material, and Z_i is the electrical impedance of i_{th} layer of material, the unit of Z_i is ohms [130].

Table 2.3.: Examples of normal incidence reflection coefficient for some common interfaces of GPR applications

Boundary	ϵ_{r1}	ϵ_{r2}	Z_1	Z_2	R
Air - dry soil	1	4	377	188	-0.05
Air - wet soil	1	25	377	75	-0.67
Dry soil - wet soil	4	25	188	75	-0.43
Dry soil - rock	4	6	188	154	-0.01
Wet soil - rock	25	6	75	154	+0.34
Ice - water	3.2	81	210	42	-0.67
Moist soil - water	9	81	126	42	-0.5
Moist soil - air	9	1	126	377	+0.5
Soil - metal	9	∞	126	0	-1

2.3.3 Water Involved Dielectric Properties of Soils

The relationship between dielectric constant and moisture content [135] As mentioned above, the most important factor in determining the dielectric constant ϵ_r of near-surface geomaterials is the volumetric water content, θ_w. The reason is because the relative permittivity (dielectric constant) is valued around $\epsilon_r \sim 81$, and this value of air is around $\epsilon_r \sim 1$, while the dielectric constant of most dry subsurface materials, like soils, gravels, concrete and rocks, is commonly values in the range $\epsilon_r \sim 3 - 4$. Thus, once water is involved in these materials, the characteristic dielectric properties will change significantly. The empirical Topp equation [139] is widely used to express the bulk dielectric constant of a soil as a function of its water content. The Topp equation works well in clays and loams but has less predictive capabilities for organic-rich soils. The equation is shown as

$$\epsilon_r = 3.03 + 9.3\theta_w + 146.0\theta_w^2 - 76.70\theta_w^3 \tag{2.38}$$

The Frequency Change due to Water and Temperature Water content and temperature of materials can also influence other values of dielectric properties of materials, such as the frequency of the dielectric relaxation. The following is quoted from Daniels (2005) [25]. From this expression, the general relationship between the frequency and water content and temperature could be simply shown.

"It should be noted that the complex dielectric constant, and hence the loss factor, of a soil is affected by both temperature and water content. The general effect of increasing the temperature is to reduce the frequency of the dielectric relaxation, while increasing the water content also increases the value of the loss factor while shifting its peak frequency down. It is observed that the frequency of the maximum dielectric loss of the water relaxation in soils is reduced and occurs over a more limited frequency range when compared with conductive water." [25]

2.4 Basic Radar Theory

2.4.1 Overview of Radar Systems

Introduction of Radar System

RADAR is short for radio detection and ranging. The technique works based on the pulse-echo measurement system, which is a system that uses the scattering of radiated waves (electromagnetic or acoustic) from an object to obtain information about that object. Normally, this system consists of four parts: 1) Transmitter 2) Transmit Transducer (Antenna) 3) Receive Transducer (Antenna) and 4) Receiver.

The function of these parts can be expressed as follows:

1. Transmitter: generates the signal.

2. Transmit Transducer: also known as Transmit Antenna in radar application; couples the energy in the transmitted signal to the propagating medium.

3. Receive Transducer: also known as Receive Antenna in radar application; couples a portion of the scattered energy in the propagating medium to the receiver.

4. Receiver: processes the signal collected by the receiver transducer to extract desired information about scattering objects.

The Transmitter of radar normally includes: Signal Generators, Modulators and Power Amplifiers. And the Receiver of radar normally includes: RF Amplifiers, Mixers, IF Amplifiers, Detectors and Filters.

A transducer is known as an antenna for electromagnetic (EM) waves (RF and Microwaves). It can take different forms as well, depending on different form of radiation, such as Lens or "telescopes" for Optical Radiation; Electromechanical Devices for Sonar; Piezo-electric transducers for Ultrasound; and Explosives or "thumpers" for Geophysical systems.

Delay and Range Estimation in Radar

As mentioned above, an electromagnetic pulse transmitted through free space travels at a velocity of $c = 2.998 \times 10^8 m/s$, and the travelling distance of entire path is $2R$, where R is known as the distance between the radar and the target. Assuming the total travelling time is τ, thus the following expressions can be established.

$$Rate \times Time = Distance \Rightarrow c\tau = 2R$$

$$\Rightarrow \tau = \frac{2R}{c} or R = \frac{c\tau}{2} \tag{2.39}$$

As a result, the range R to the target can be determined by measuring the delay until the reflected echo is heard. To do so, is difficult in an electromagnetically noisy environment.

2.4.2 Radar Equation

Friis Equation

The antenna of radar has an aperture, which is a surface of constant phase near the "face" of the antenna. The aperture of an antenna has an area expressed as A. This area always characterizes the antenna's behaviour. Now suppose two antennas "point at each other" with a large distance R apart.

Define:

A_T = aperture area of transmit antenna

A_T = aperture area of receive antenna

P_T = transmitted power

P_R = received power

λ = the wavelength of transmitted wave

R = the distance between transmit antenna ans receive antenna

Then the following equation can be obtained, known as the **Friis Equation**:

$$\frac{P_R}{P_T} = \frac{A_T A_R}{\lambda^2 R^2} \tag{2.40}$$

To fulfill the requirements of Friis Equation, it must be used under the condition of far field and small angles off boresight. And the aperture must be large enough for scalar diffraction to be accurate. The requirements can be formed as follows:

$$R \gg \frac{D_{max}^2}{4\lambda}$$

$$D_{min} \gg \lambda$$

For linear antenna systems, P_R/P_T remains the same when the roles of the transmit and receive antennas are reversed. This expression is called Reciprocity Theorem.

Antenna Gain

Assume an antenna that radiates (transmits) energy uniformly in all directions, a so called Isotropic Radiator. When receiving, it is equally sensitive to energy from all directions. Then if there is a receive aperture A_R at a distance R from an isotropic radiator, and the surface area of sphere of radius R, $a = 4\pi R^2$,

$$\frac{P_R}{P_T} = \frac{A_R}{4\pi R^2} \tag{2.41}$$

Apply to the Friis Equation

$$\frac{P_R}{P_T} = \frac{A_R}{4\pi R^2} = \frac{A_i A_R}{\lambda^2 R^2} \tag{2.42}$$

So

$$\Rightarrow A_i = \frac{\lambda^2}{4\pi} \tag{2.43}$$

The gain of A_T over A_i is then

$$G = \frac{(P_R/P_T)_T}{(P_R/P_T)_i} = \frac{(P_R)_T}{(P_R)_i} = \frac{4\pi A_T}{\lambda^2} \tag{2.44}$$

So in general, the relation between the effective area A and gain G of antenna is obtained

$$G = \frac{4\pi A}{\lambda^2} \tag{2.45}$$

$$A = \frac{\lambda^2 G}{4\pi} \tag{2.46}$$

The antenna gain G is often expressed in dB as:

$$G(dB) = 10log_{10}G(dB)$$

Based on the reciprocity theorem, the gain of an antenna on transmit is equal to the gain of an antenna on receive. So, the Friis Equation can be written in the form of antenna gains as following:

$$\frac{P_R}{P_T} = \frac{G_T G_R \lambda^2}{16\pi^2 R^2} \tag{2.47}$$

Radar Equation

The Radar Equation generally expresses the relation between power P_T transmitted, and power received P_R, assuming the target has the following characteristics: 1) a receive aperture, $A_R = \sigma(m^2)$; and 2) it re-radiates (reflects) all of this received energy isotropically.

So the power received by the target is given by

$$\frac{P_\sigma}{P_T} = \frac{A\sigma}{\lambda^2 R^2} \tag{2.48}$$

The fraction of the re-radiated power received is

$$\frac{P_R}{P_\sigma} = \frac{A_i A}{\lambda^2 R^2} = \frac{(\lambda^2/4\pi)\, A}{\lambda^2 R^2} = \frac{A}{4\pi R^2} \tag{2.49}$$

Combine the above equations together,

$$\frac{P_R}{P_T} = \frac{P_R}{P_\sigma} \cdot \frac{P_\sigma}{P_T} = \frac{A^2\sigma}{4\pi\lambda^2 R^4} \tag{2.50}$$

Finally, the **Radar Equation** can be expressed as

$$\frac{P_R}{P_T} = \frac{A^2\sigma}{4\pi\lambda^2 R^4} \tag{2.51}$$

2.4.3 Radar Cross Section (RCS)

The area σ in the above Radar Equation is defined as the Radar Cross Section (RCS), which is used to characterize the scattering characteristics of a target. The RCS is defined in terms of a hypothetical target, which defines an equivalence class of targets. The RCS is used to describe physical targets that behave nothing like the hypothetical target that defines it. So this is a simplified expression of complex physical targets' radar scattering characteristic.

There are several factors that could influence the radar cross section value, such as:

- Size of Target
- Shape of Target
- Wavelength of Radiation
- Target Material
- Orientation (Angle) of Radar facing the Target

Table 2.4 shows RCS values of some common objects with different shapes [25].

Table 2.4.: Examples of normal incidence reflection coefficient for some common interfaces of GPR applications

Scatterer	**Max RCS Area**	**Symbols**
Sphere	$\sigma_{max} = \pi a^2$	$a = radius$
Flat plate (arbitrary shape)	$\sigma_{max} = \frac{4\pi A^2}{\lambda^2}$	$A =$ plate area
Cylinder	$\sigma_{max} = \frac{2\pi a l^2}{\lambda}$	$a = radius$, $l = length$
Prolate spheroid	$\sigma_{max} = \frac{\pi b_0^2}{a_0^2}$	$a_0 =$ major axis, $b_0 =$ minor axis
Triangular trihedral corner reflector	$\sigma_{max} = \frac{4\pi L^4}{3\lambda^2}$	$L =$ side length

2.4.4 GPR Dynamic Range

Dynamic Range is a common evaluation parameter for a specific GPR system. It represents the maximum total attenuation loss during the two-way transit of the electromagnetic wave which will still allow reception; signals with greater losses will not be recorded. The ratio of the largest receivable signal to the minimal detectable signal is called the dynamic range and is defined as follows [131]:

$$DynamicRange = 20log\left(\frac{V_{max}}{V_{min}}\right) \tag{2.52}$$

The dynamic range is normally expressed in decibels (dB) for a specified bandwidth in hertz. The largest receivable signal, V_{max} (in V), must not overload the radar front end and, assuming some gain has been applied to the received signal, is the maximum sample voltage of the analog-to-digital conversion (ADC). The minimal detectable signal, V_min (in V), must be above the receiver noise level and have a minimum signal-to-noise ratio (SNR) to be detected.

The dynamic range of the system will affect the maximum range at which a target can be detected. It is obvious that the dynamic range directly influences the exploration depth of the GPR; as the larger the dynamic range, the greater the GPR penetration. Typically, radars will have a greater system dynamic range than sampling dynamic range. The dynamic range in decibels of an ADC can be simply described as [131]:

$$DynamicRange = 20log(2^N) \approx N \times 6(dB) \tag{2.53}$$

where N is the number if signal bits.

As a result, a 16-bit ADC will have approximately $96dB$ of theoretical dynamic range.

2.4.5 Signal Losses of GPR system

General Introduction

The range of a GPR is primarily governed by the total path loss, and the three main contributions to this are the material loss, the spreading loss and the target reflection loss or scattering loss.

The signal that is detected by the receiver undergoes various losses in its propagation path from the transmitter to the receiver. The total path loss for a particular distance is defined by

$$L_T = L_e + L_m + L_{t1} + L_{t2} + L_s + L_a + L_{sc} \tag{2.54}$$

where,

$L_T =$ total path loss in dB

$L_e =$ antenna efficiency loss in dB

$L_m =$ antenna mismatch losses in dB

$L_{t1} =$ transmission loss from air to material in dB

$L_{t2} =$ retransmission loss from material to air in dB

$L_s =$ antenna spreading losses in dB

$L_a =$ attenuation loss of material in dB

$L_{sc} =$ target scattering loss in dB

Antenna Loss

The antenna efficiency is a measure of the power available for radiation as a proportion of the power applied to the antenna terminals. Generally, a loss of $-2dB$ per antenna is considered normally. For a pair of loaded dipole antennas, the antenna loss will be given by:

$L_e = -4(dB)$

Antenna Mismatch Loss

The antenna mismatch loss is a measure of how well the antenna is matched to the transmitter; usually little power is lost by reflection from antenna mismatch and is on the order of $^{-}1dB$.

$L_m = -1(dB)$

Transmission Coupling Loss

In the case of antennas operated on the surface of the material the transmission loss from the antenna to the material is given by

$$L_{t1} = -20log_10 \left(\frac{4Z_m Z_a}{\mid Z_m + Z_a \mid^2} \right) (dB) \tag{2.55}$$

where:

Z_a = characteristic impedance of air, which equals 377Ω

Z_m = characteristic impedance of the material, typically, for many earth material Z_m = 125Ω

So, $L_{t1} = -2.5dB$.

Retransmission Coupling Loss

The retransmission loss from the material to the air on the return journey is given by

$$L_{t2} = -20log_10 \left(\frac{4Z_m Z_a}{\mid Z_m + Z_a \mid^2} \right) (dB) \tag{2.56}$$

So, $L_{t2} = -2.5dB$.

Spreading Loss

The antenna spreading loss is conventionally related to the inverse fourth power of distance for a point reflector, the L_s can be defined as

$$L_s = -10log_10\frac{G_t A_r \sigma}{(4\pi R^2)^2} \tag{2.57}$$

where:

G_t = gain of transmitting antenna (loaded dipole) = 15

A_r = receiving aperture (loaded dipole) = $4 \times 10^{-2} m^2$

R = range to the target = $1.0m$

σ = radar cross-section ($\sigma = 1m^2$).

So, $L_s = -21dB$

Target Scattering Loss

In the case of an interface between the material and a plane, where both the lateral dimensions of the interface and the overburden are large, then

$$L_{sc} = 20log\left(1 - \mid \frac{Z_1 - Z_2}{Z_1 + Z_2} \mid\right) + 20log\sigma \tag{2.58}$$

where:

Z_1 = characteristic impedance of the first layer of material

Z_2 = characteristic impedance of second layer of material

σ = target radar cross-section

Typically, L_{sc} would be in the order of $^{-}1.6dB$ for the interface between the first and second layers.

Material attenuation loss

The attenuation loss of the material is given by

$$L_a = 8.686 \times 2 \times R \times 2\pi f \sqrt{\left(\frac{\mu_0 \mu_r \epsilon_0 \epsilon_r}{2}\left(\sqrt{(1+tan^2\delta)}\right) - 1\right)} \tag{2.59}$$

where:

f = frequency in Hz

$tan\delta$ = loss tangent of material

ϵ_r = relative permittivity of material

ϵ_0 = absolute permittivity of free space

μ_r = relative magnetic susceptibility of material

μ_0 = absolute magnetic susceptibility of free space

Total losses

Based on the above information, the total losses that will occur at 100 MHz during transmission through 1m of material of 2.7 dB/m attenuation and then reflection from a boundary interface, where Z_1 = 125Ω and Z_2 = 89Ω would be

$$L_T = L_e + L_m + L_{t1} + L_{t2} + L_s + L_a + L_{sc} = -4dB - 1dB - 2.5dB - 21dB - 5.5dB - 1.6dB = -38dB \tag{2.60}$$

2.5 Basic GPR Signal Processing Theories

2.5.1 Introduction

The general objective of signal processing as applied to Ground Penetrating Radar is normally to present an image that can readily classify the target returns. The image of a buried target generated by a GPR will not, of course, correspond to its geometrical repre-

sentation. The fundamental reasons for this are related to the ratio of the wavelength of the radiation and the physical dimensions of the target. Unlike normal radar systems, in GPR applications, the target and the clutter are spatially fixed and the radar antenna is moved on/above the surface. The general processing problem encountered in dealing with GPR data is in the widest sense the extraction of a localized wavelet function from a time series which displays very similar time domain characteristics to the wavelet. This time series is generated by signals from the ground and other reflecting surfaces, as well as internally from the radar system.

The received time waveform can be described as the convolution of a number of time functions each representing the impulse response of some component of the radar system in addition to noise contributions from various sources. There is thus a range of signal processing methods and theories that can be applied to each single GPR scan.

2.5.2 Zero offset removal

An important process operation is to ensure that the mean value of the single GPR scan (A-scan) is near to zero. This assumes that the amplitude probability distribution of the signal is symmetric about the mean value and that the short time mean value is constant over the time duration. Signal processing algorithms that cater to these situations, such as

$$A'_n(t) = A_n(t) - \frac{1}{N}\sum_{n-0}^{N} A_n(t) \tag{2.61}$$

where $A_n(t) =$ unprocessed data sample, $A'_n(t) =$ processed data sample and $n =$ sample number, will only work where the short term mean value is constant and the amplitude probability distribution is symmetric.

2.5.3 Noise reduction

An important GPR signal processing technique is noise reduction and can be achieved by either averaging each individual sample of the A-scan signal or averaging repeated A-

scan signals. The general effect is to reduce the variance of the noise and gives an improvement in signal to noise ratio (SNR). Averaging normally has no effect on clutter but reduces random noise.

The general noise reduction process can be expressed as

$$A'_n(t) = A'_{n-1} + \frac{[A_n(t) - A'_{n-1}(t)}{K} \tag{2.62}$$

where $A'_n(t)$ is averaged value and $A_n(t)$ is current value. The factor K is a fixed value which will weight the averaged value appropriately, normally it equals the sample number or the number of scans.

2.5.4 Clutter Reduction

Clutter reduction can be achieved by subtracting from each scan signal an averaged value of an ensemble of scan signals taken over the area of interest, which can be shown as:

$$A'_{n,a}(t) = A_{n,a}(t) - \frac{1}{N_a}\sum_{a=1}^{N_a} A_{n,a}(t) \tag{2.63}$$

where n = 1 to N (N is the number of samples), a = 1 to N_a (N_a is the number of scan signals (waveforms), $A_{n,a}(t)$ is the unprocessed scan signal and $A'_{n,a}(t)$ is the processed scan signal.

This method works well for situations where the number of targets is limited and they are physically well separated, which is the same as the situation of the under pavement pipe (drainage) installations.

An alternative version of this process is related to the standard deviation of the signal samples. Each unprocessed scan signal is compared with the standard deviation time function, and samples which are greater than the standard deviation time function by a

predetermined amount, such as one, two or three σ, are defined as significant. Then this alternative version can be expressed as:

$$A'_{n,a}(t) = A_{n,a}(t) - \frac{K}{N_a}\sum_{a=1}^{N_a} A_{n,a}(t) \tag{2.64}$$

where K is a variable related to the required magnitude of the standard deviation.

This process method can also be applied to a selected section of the scan signal in order to remove clutter associated with a particular region of time.

2.5.5 Time varying gain

The received signal is reduced in amplitude compared with the transmitted signal as a result of both attenuation by the medium of propagation and by the path or spreading loss encountered in traveling to and from the target. In GPR signal processing , it is normally to apply time varying gain to compensate for these losses. The process can be shown as:

$$A'_n(t) = A'_n(t)kn \tag{2.65}$$

where k is the weighting function of the sample number.

2.6 Summary

In this chapter, several basic theories related to GPR application to underground target detection are introduced. Further developed/introduced methods to solve the research problems in this thesis are based on these theories in this chapter, including both digital signal processing methods and hardware based approaches.

3. EQUIPMENT OVERVIEW

3.1 Introduction

In this effort, equipment was acquired to assemble an enhanced GPR unit capable of utilizing multiple transmitter and receiver antennae operating at varying frequencies to develop an image of the subsurface. The key aspects of this new hardware are described in detail below.

3.2 Overview of GPR Equipment

To enable the multi-antennae capability desired for this effort, a new GPR control unit, the SIR-30, was purchased from GSSI Inc. This unit was selected due to its features and compatibility with existing INDOT (sponsor) equipment, and offers the ability to collect data from 4 different channels at the same time. This allows simultaneous collection of data from different frequency antennae, facilitates use of a Multi-input Multi-output (MIMO) antenna array, and also enables the comparison of data at different antennae polarization. The key components of this system include the following:

1. Main Control Unit (SIR-30): enables 4 antennae to work at the same time
2. LCD Digital Monitor together with Keyboard and Mouse(or a laptop with an Ethernet cable connection): facilitates user interface with control unit
3. Antennae with Distance Measuring Instrument (DMI): together with SIR-30control unit, the antennae and DMI create a complete location-indexable Tx-Rx system

3.2.1 Main Control Unit (SIR-30)

The SIR-30 control unit serves as the center of the GPR system used in this research, enabling simultaneous operation of 4-channels, as well as high data transmission speed and improved data resolution. The maximum pulse repetition frequency (PRF) that can be transmitted by the SIR-30 is $\sim 733KHz$, which means the system can collect $\sim 3/4$ million samples per second. However, the actual data collection rate pursued in lab experiments and field surveys varied based on the PRF of each antenna and the desired density of data collection points. Based on the combined capabilities of the control unit and antennae, the average vehicle speed for a field survey is likely limited to around 3-4 miles per hour to ensure capture of quality data with a resolution of roughly at 48 traces/ft. The control unit also has a 32-bit A/D unit which enhances detection sensitivity relative to pre-existing INDOT equipment.

Figure 3.1 provides an image of the SIR-30 unit. This unit can be controlled by a laptop connected by Ethernet cable, which enables convenient use in the field. Also this unit itself is a personal computer. So, with an interface LCD monitor and input devices (keyboard and mouse), it can be self-controlled, which increases data transmission and storage speed, which are again valuable benefits in the field.

The unit dimensions are 17.7×13×5.1in (45×33×13cm) and it weights only 18.5 lbs (8.4 kg).

3.2.2 GPR Antennae

Based on the required resolution and depth of penetration for the pavement drainage application, antennae of three different frequencies will be employed in this research, 900 MHz, 400 MHz, and 270 MHz. Each of the antennae are pulsed radar devices; the original signal they generate is a simple Ricker pulse. An illustration of an integrated antenna box is shown in Figure 3.2. Each antenna box contains separate transmitter and receiver antennae, one control unit connector, and two Distance Measuring Instruments (DMI) with connectors for different DMI survey wheels.

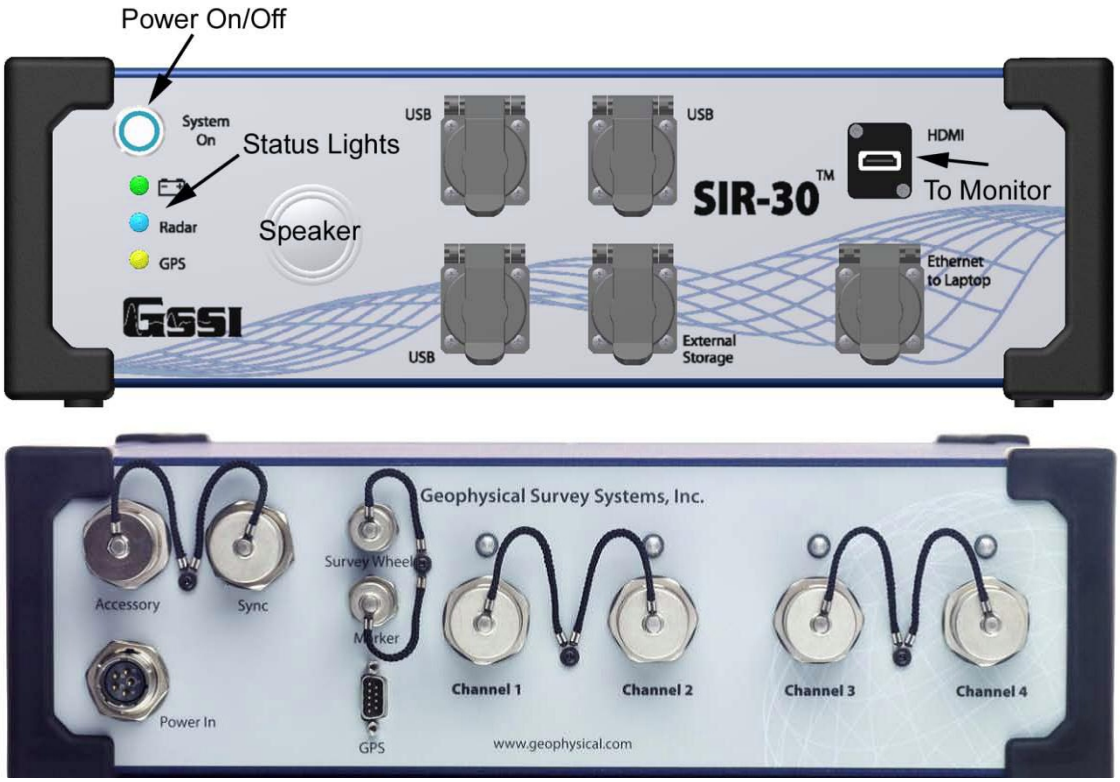

Figure 3.1.: Front and back view of SIR-30 control unit (GSSI SIR-30 Manual)

This design makes it possible to build a MIMO GPR system, in which the transmitter and receiver can be controlled individually.

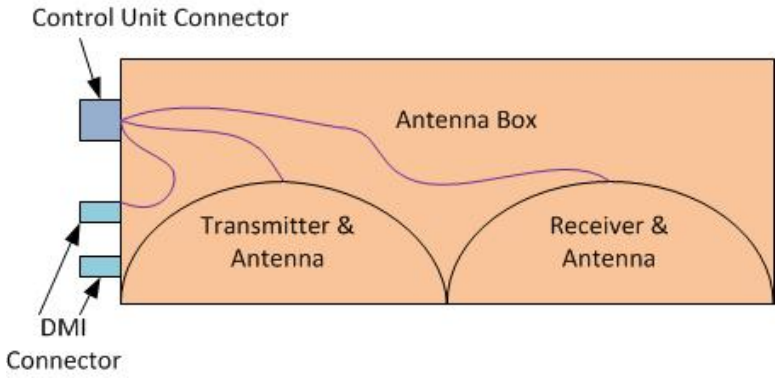

Figure 3.2.: Schematic of an integrated antenna box produced by GSSI Inc

Outfitted with a suitable DMI survey wheel, the antennae can be run in distance mode or continuous time mode. The former mode provides the exact horizontal position of imaged targets. In continuous time mode, antennae transmit signals based on a time clock signal, which is useful in static tests without antennae movement. Most GPR surveys require the movement of the antennae to obtain data at different positions along the survey line. As a result, traditionally, a constant travel speed must be carefully maintained in order to receive stable shapes in the reflected signal, which is not straightforward in practice. However, together with the DMI, the antennae can transmit signals and track position in the distance control mode. Because the antenna position can then be determined very easily, the speed will not influence the shape of the received signals, simplifying field operation.

Model 3101 900MHz GPR Antenna

This antenna with a central frequency of 900 MHz is designed for applications requiring high resolution but shallow penetration depth (GSSI Inc. Manual). (Dimensions of the integrated antenna box are $13\times7.5\times3.5$ inches ($33\times20\times8$cm)). Figure 3.3 shows the Model 3101 900 MHz antenna attached to a Model 611 survey wheel. The pulse duration of the source signal is 15ns. The effective penetration depth is between 0 and 6ft depending on the dielectric permittivity of encountered materials.

Model 5040 400MHz GPR Antenna

This antenna with 400MHz central frequency,shown in Figure 3.4, is a mid-frequency GPR antenna designed for greater penetration depths, but with decreased resolution compared to the high frequency antenna.The dimensions of the entire antenna unit are $12\times12\times6.5$ inches ($30\times30\times17$cm).The transmitted pulse duration of this antenna is 25ns, and the effective penetration depth is 0 to 16ft depending on the dielectric permittivity of encountered materials.

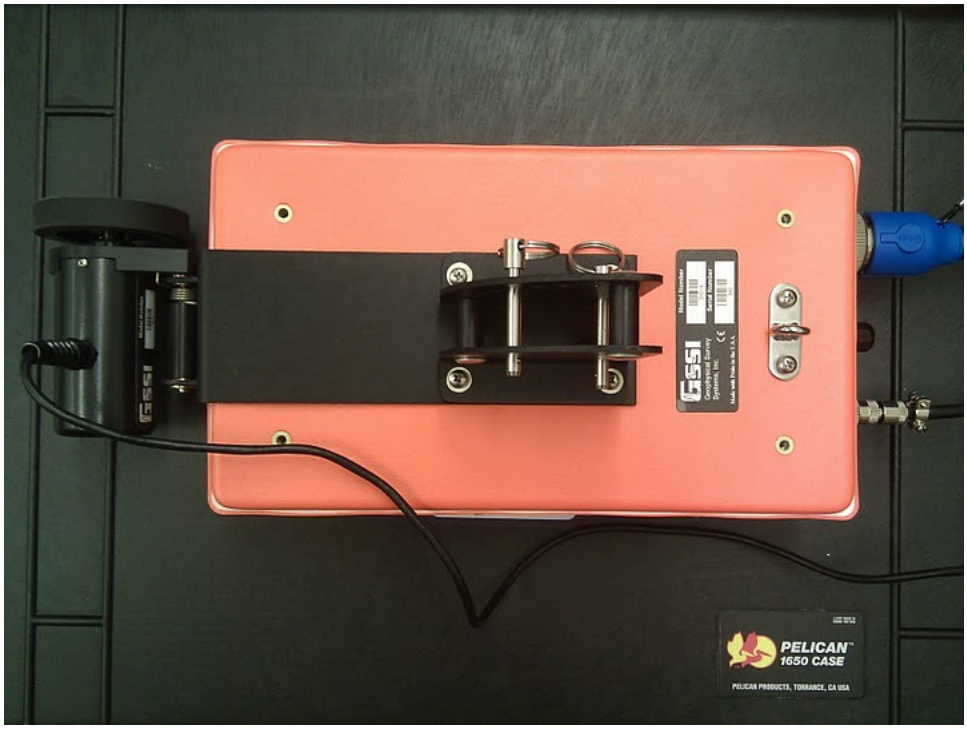

Figure 3.3.: Model 3101 900 MHz antenna attached to a Model 611 survey wheel

Model 5104 270MHz GPR Antenna

This antenna is designed for deeper penetration with a 270MHz centered frequency. The dimensions of this antenna case are 17.5×17.5×7.5 inches (44.5×44.5×19cm). The transmitted pulse duration is 3.6ns and the effective penetration depth is 0 to 25ft depending on the dielectric permittivity of encountered materials. The application of this frequency is normally for large targets buried at greater depths.

Model 611 survey wheel (DMI)

Compared to a typical survey cart used in the field with large wheels (about 12 inches in diameter), the wheel size of this equipment is quite small - about 3.83 (3 5/6) inches in diameter which is a suitable size to be used in laboratory tests. It can be attached directly to the 900MHz antenna box (Figure 3.3) and also can be used together with 400MHz antenna.

Figure 3.4.: Top View of Model 5040 400MHz GPR antenna

The maximum control rate of this wheel is about 609.6 ticks/foot (2000 ticks/meter), which means this wheel can control the antenna to transmit at most 2000 signals per meter.

3.3 Standard Testing Procedures

As described above, the GPR system used in this project contains several components. Before carrying out lab or field experiments, correct integration of the system must be completed. The general procedures to prepare the multi-channel GPR system for use are straightforward and can be summarized as follows:

1. Attach a DMI survey wheel to each of the antenna boxes to be used in the test and connect them with a suitable cable;

2. Connect all antennae needed in the experiment to the main SIR-30 control unit using supplied and appropriately connective cables;

Choose one from 3 and 4:

3. If using monitor to control the unit directly, connect a digital LCD monitor to the SIR-30 main body with an HDMI cable, as well as the necessary input devices, such as a keyboard and mouse;

4. If using a laptop to run the unit, first set up the laptop as a client computer which can communicate to the main body of SIR-30, then connect the laptop to SIR-30 with an Ethernet cable;

5. Plug in all source power connections on the monitor or laptop, then the SIR-30 control unit;

6. Open the SIR-30 control program to identify necessary parameters of all connected antennae;

7. The system is now ready to perform a survey.

4. RESEARCH APPROACHES AND METHODS

4.1 Introduction

The work carried out in this study involved a two-pronged approach to improve GPR-based sub-pavement drainage system evaluation. Specifically, two major avenues were explored to achieve improvements in GPR detection success: 1) software-based signal processing and 2) modifications of hardware test configurations (see Figure 4.1). Simulations (section 4.3) and experiments (section 4.4) were employed throughout this work as an efficient means to assess the potential benefits and limitations of these improvement efforts under various test conditions. Once high potential solutions were identified, extensive field tests (section 4.5) were also performed.

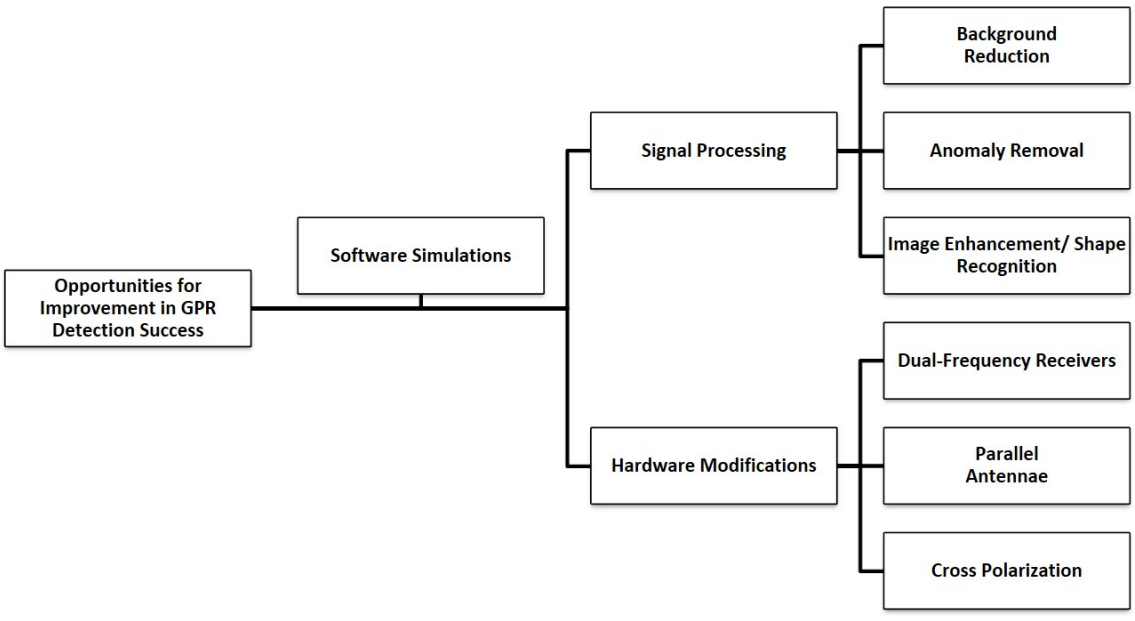

Figure 4.1.: Avenues of potential improvement in GPR detection success

4.2 Design Factors of Research Methods

Two main sets of variables which influence GPR observations were considered in different simulation and experimental contexts: Environment factors and Equipment factors.

4.2.1 Environment Factors

There are several key environment factors, which will easily influence the detection accuracy using GPR, detailed introduced as follows.

Drainage conduit type and size

Subsurface drainage systems encountered in the built environment vary widely and may range in size from just a few to tens of square centimeters in cross section. Further, drainage conduits may be concrete, clay, or plastic pipe (e.g. transverse or longitudinal pipe drains) or geo-textile composites (e.g. geo-composite edge drains or permeable layers).

Drainage conduit installation geometry

Sub-pavement drainage systems may be oriented in a transverse or longitudinal direction relative to the roadway and must be installed at a slope steeper than 0.2% for subsurface drains and 0.3% for outlet pipes; different geophysical techniques may be required to rapidly locate drains in these two distinct orientations.

Soil type and sub-grade type

Although most primary road designs share common design principles, the sub-grade materials can vary location to location based on availability and their bulk dielectric properties can potentially be influenced by aggregate compaction and infiltration by other soils (the more conductive the soil, the greater the radar attenuation).

- Highly conductive soil: Water saturated (wet) soil or highly salty soil (e.g., where salt is used for ice melting)
- Clay dominated soil: usually includes significant moisture, making it highly conductive
- Silt dominated soil: usually found in topsoil, containing some amount of moisture, making it moderately conductive – less likely in primary road scenario
- Sand dominated soil: containing little moisture, and hence low conductivity
- Granular and compacted soil: usually found under paved areas, very low conductivity

Pavement material (HMA or WMA, Concrete)

Clearly primary road surfaces may take on an array of forms related to varying formulations of hot (warm) mixed asphalt or concrete.

Strata thickness and conduit depth

Again, primary road layer thickness and the resulting location of subsurface drainage conduits can vary based on road design.

4.2.2 Equipment Factors

Arrangement and number of GPR transmitters and receivers

GPR surveys can be performed in a variety of ways (e.g., common offset, multi-offset) that each maximize the response from some sub-surface features and minimize the response from others.

Coupling geometries

GPR can generally be air-coupled or ground-coupled into the subsurface; the choice of coupling method involves a compromise between coupling efficiency and testing speed.

Operating frequency range (commonly from 10 MHz to more than 1,000 MHz)

Although GPR is generally viewed as the geophysical method with the highest resolution for imaging the subsurface (with centimeter scale resolution possible in some circumstances), there is an inevitable trade-off between resolution and penetration depth, driven by operating frequency. Depth of investigation increases with decreasing frequency but at the cost of decreased resolution. While GPR waves can reach depths of 30-40 m in materials such as ice or volcanic rock, they may penetrate only 1-2 m in materials such as clay or shale.

Absolute vs. relative measurements

While it would be ideal to obtain absolute measurements with any sensing system (that is measurements that are accurate and definitive at a single point in time), under some circumstances relative measurements (that is subsequent measurements compared to each other) may prove useful in difficult sensing conditions and could yield insight (for example, scanning the sub-surface before and after rainfall to find variations in subsurface moisture that may help locate drainage conduits).

4.2.3 Design Criteria of Subsurface Drainage

The primary features of a typical drainage system include the followings [140, 141], which would be helpful in both lab and field experiment design:

- Permeable drainage layer.
- Filter layer or impervious membrane (such as different Geosynthetics).

- Perforated edge pipes (typically longitudinal direction, for collection use).
- Outlet pipes and side ditches.
- Markers.

Furthermore, there are several criteria of subdrainage design which will also be important when detecting drains [12]:

Slope and depth Based on design requirements, subsurface drainage pipes need to be installed at a fixed depth below the pavement, typically greater than 100 mm. And the slope is required to be steeper than 0.2% for subsurface drains and 0.3% for outlet pipes.

Size Subsurface drainage pipe must be 6in diameter for newly constructed pavement and 4in for rehabilitation of existing pavement.

Location Subsurface drains are typically constructed along each pavement edge. The drainage pipe is continuous through each intersection, ramp, turn lane and taper, and should be located in the pavement section.

4.3 Computer-Based Electromagnetic Simulation

4.3.1 Overview

Simulations were carried out using GPRMAX2D software (Copyright 2005 by Antonis Giannopoulos) to inform the design and performance of lab and field experiments. GPRMAX2D is an electromagnetic wave simulation software package for Ground Penetrating Radar models designed by Dr. Antonis Giannopoulos of the University of Edinburgh, UK. This simulator is based on the Finite-Difference Time-Domain (FDTD) method. Simulations were employed throughout this work for multiple purposes including the design of the in-laboratory test basin, exploration of the influence of road cross-section designs on radar signatures, and evaluation of alternate GPR antennae configurations. In

particular, simulations offer the advantage of modelling situations with infinite boundary conditions, which eliminates the influence of even subtle side reflections that might be encountered in a scaled down laboratory experiment that must inevitably be “contained”.

4.3.2 Simulation with Infinite Boundary Conditions

Two simulations in particular were pursued to determine the influence of water and pavement cover on GPR observations of sub-pavement conduits and are highlighted here. The depth of pipes (PVC) was set at 0.6m, which is a reasonable depth based on typical road cross-section design. The dimensions of the simulated area were chosen to enable inclusion of 3 different diameter pipes, located with enough distance (0.75m in the models) between them to avoid relative interference. The antennae of GPR unit were simulated to move along the ground surface in the simulation models. The data collection rate was one trace per 0.03 meters. Two different offsets (along the horizontal direction) between the transmitter and receiver were considered in both models, 0 meters and 0.2 meters.

Schematics of these two models are shown in Figure 4.2. The size of the simulated area is $3m(L) \times 0.8m(D)$. There are 3 PVC pipes involved; with diameters of $4''$, $6''$ and $8''$, respectively. Side and bottom boundary conditions for the calculation area were absolved infinite boundaries. In addition, a free boundary is modeled at the surface. As illustrated in Figure 4.2 below, Model 1 involves only sand and no pavement cover. One concrete pavement layer is introduced in Model 2. While these models are obviously simplified relative to an actual road cross-section, they help to assess fundamental geometric and material impacts on different GPR test configurations. In particular, several groups of simulations have been analyzed for each model involving important factors such as radar frequencies, antennae offset, and water conditions in the sand (saturated or dry). Table 4.1 provides the details of the analyzed simulations.

As shown in Table 4.1, 12 different simulations have been analyzed with different key parameters. Figures 4.3 (a-f) and 4.4 (a-f) provide all the analyzed results, for Models 1 and 2, respectively.In all the following figures, the horizontal axis represents the trace

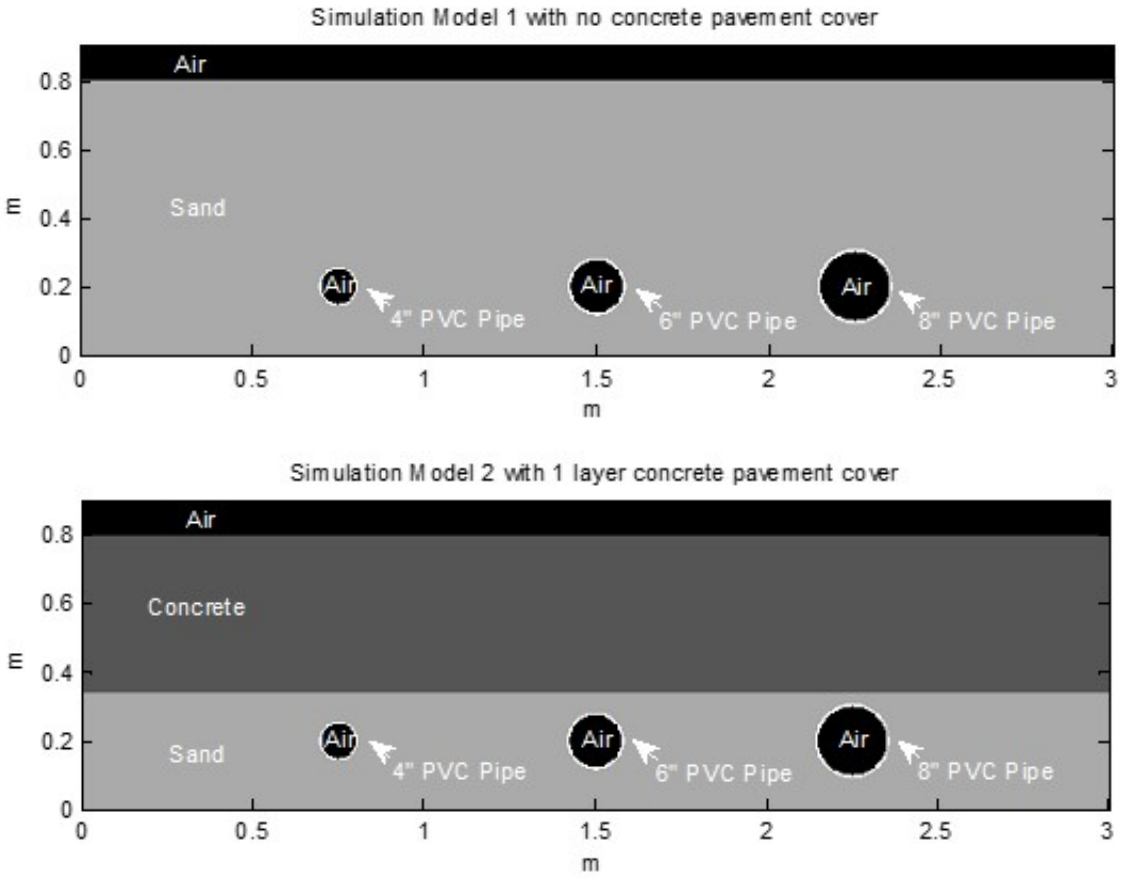

Figure 4.2.: Schematics of Simulation Models: no pavement cover (top) and concrete pavement cover (bottom)

Table 4.1.: Details of analyzed simulations and related parameters

Model.	Antennae Offset (m)	Operated Frequency (MHz)	Water Conditions of Sand (Dry or Saturated)	Simulation No.	Result Figure No.
Model 1	0	900	Dry	1-0-900D	5-3 (a)
		400	Dry	1-0-400D	5-3 (b)
		900	Saturated	1-0-900S	5-3 (c)
	0.2	900	Dry	1-0.2-900D	5-3 (d)
		400	Dry	1-0.2-400D	5-3 (e)
		900	Saturated	1-0.2-900S	5-3 (f)
Model 2	0	900	Dry	2-0-900D	5-4 (a)
		400	Dry	2-0-400D	5-4 (b)
		900	Saturated	2-0-900S	5-4 (c)
	0.2	900	Dry	2-0.2-900D	5-4 (d)
		400	Dry	2-0.2-400D	5-4 (e)
		900	Saturated	2-0.2-900S	5-4 (f)

number along the scan direction. The vertical axis represents the time axis, which provides

the arrival time of reflected signals in the unit of nanoseconds. All the hyperbola shapes in the simulation results indicate reflection signals of potential targets.

Comparing all the sets of simulation results, there are several conclusions that can be drawn, as follows:

- Simulations with 0.2 meters offsets between the transmitter and receiver can help improve the GPR results significantly, especially with saturated soil conditions. As shown in Figure 4.3 (c), when using the 900MHz antennae with Model 1 involving saturated sand and a 0m offset between Tx and Rx, the target is very hard to detect. However, in Figure 4.3 (f), which has the same soil conditions as 4.3 (c) but with 0.2 meters offset between Tx and Rx, the three targets are clearly found. The reflection delay from targets in saturated sand is much longer than for the dry sand, which is shown in Figure 4.3 (d). In dry sand the delayed reflection time is around 8ns (Figure 4.3 (d)), but in saturated sand it varies from 16ns to 18ns (Figure 4.3 (f)), due to the fact that EM waves travel much more slowly in water than in dry materials (sand in this case).

- Based on the simulation results, a concrete pavement layer will decrease the resolution of GPR images under dry sand conditions, as shown by comparing Figures 4.3 (a) and Figure 4.4 (a). With 0.2m offset of the Tx and Rx, the results improve as shown in Figures 4.4 (d) and (e).

An interesting preliminary finding revealed in the simulation is that the quality of the GPR results improves under both 400 MHz (Figure 4.4 (e)) and 900 MHz (Figure 4.4 (f)) analysis when pavement cover is present. The improved images are again generally associated with a 0.2 meter offset between Tx and Rx. These observations are discussed again later in the context of the field experiments.

Details of additional simulations are provided where relevant throughout the thesis.

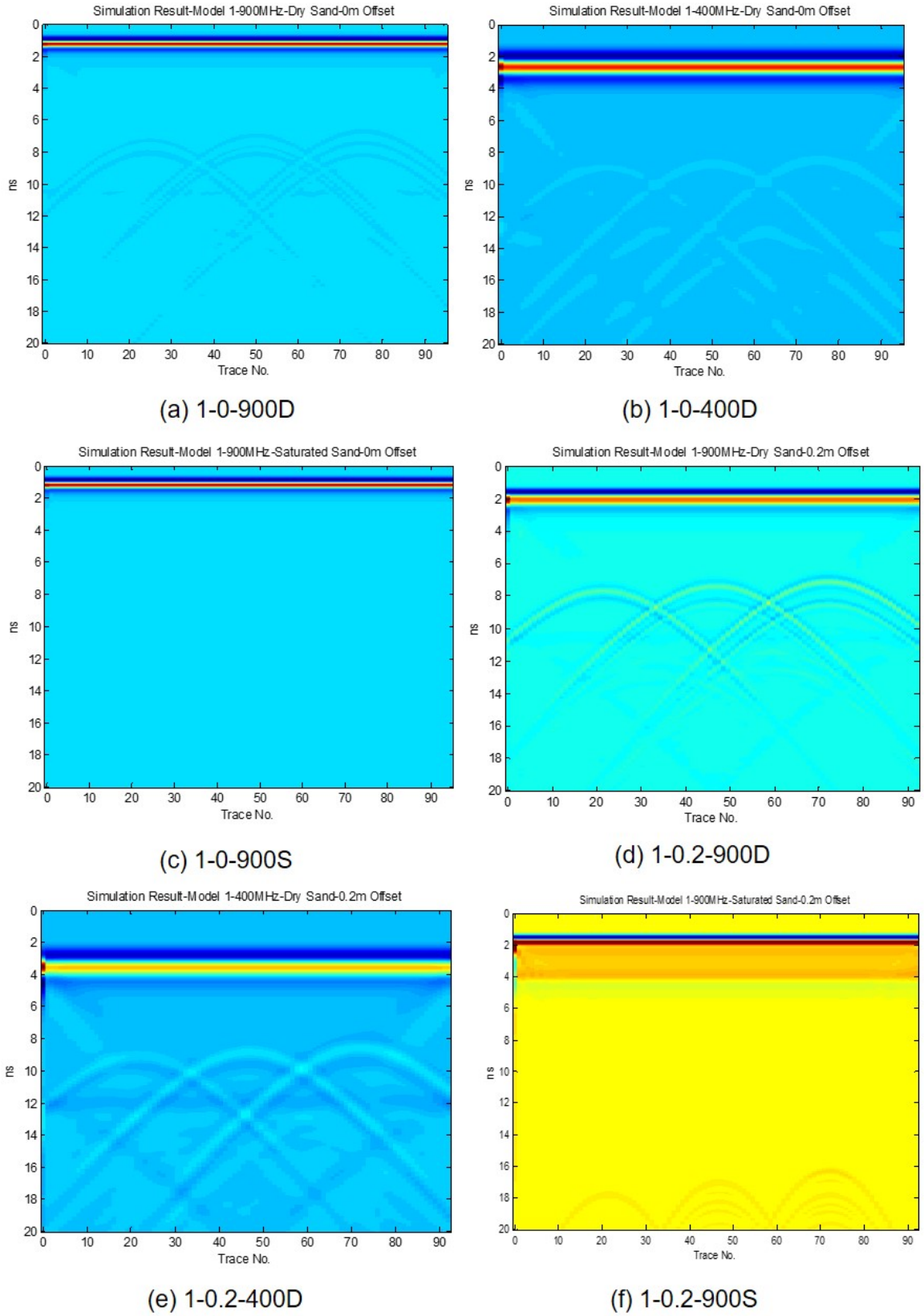

Figure 4.3.: Simulation Results of Model 1: Sand only

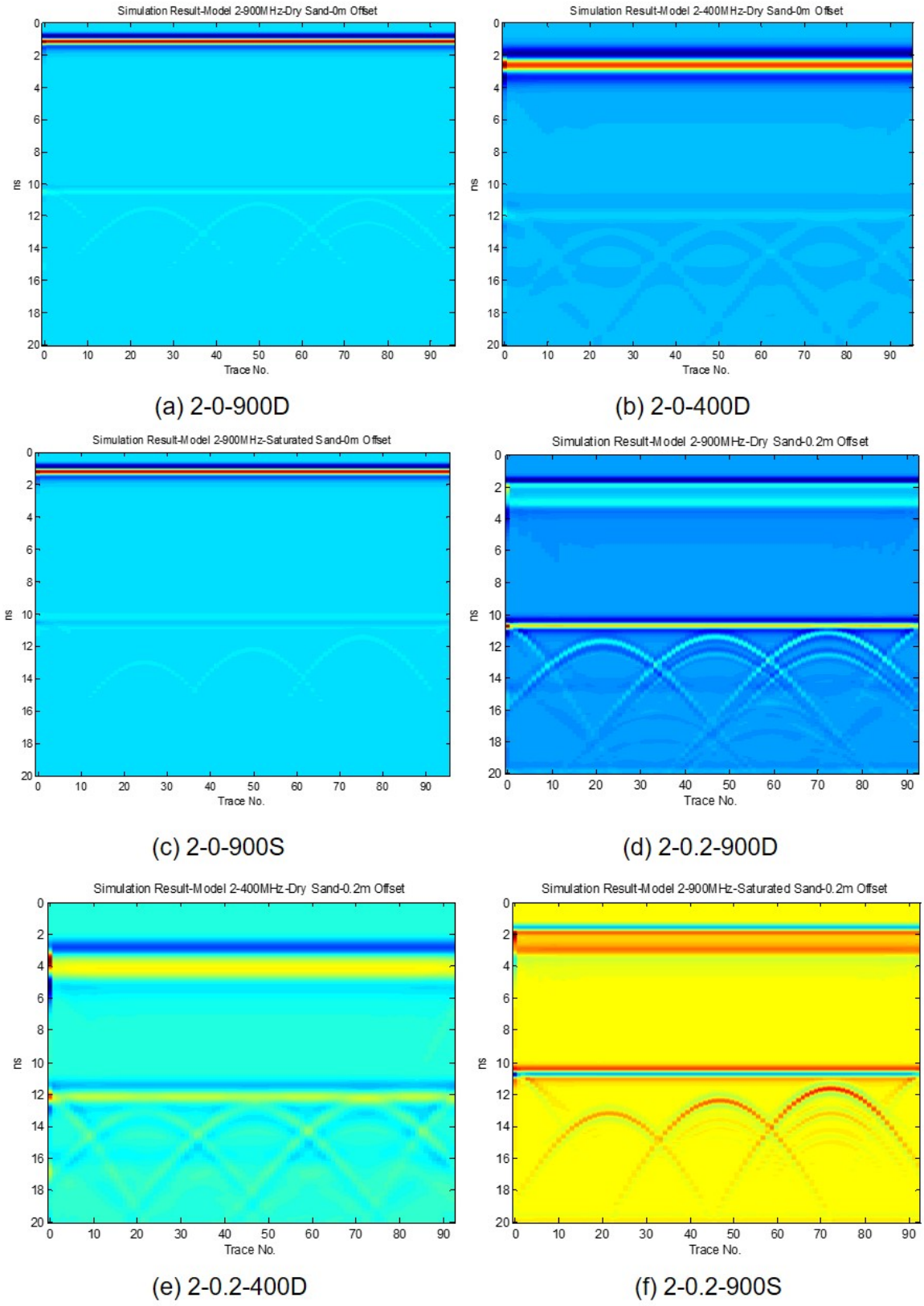

Figure 4.4.: Simulation Results of Model 2: Sand with concrete cover layer

4.4 Design of Laboratory Experiments

Lab experiments are an efficient means to proof test equipment, simulate situations likely to be encountered in the field, and assess possible solutions to identified detection or operational challenges. With this in mind, a simple in-laboratory test basin – that is a vessel that contains the soils and other materials used to represent any given field scenario — was designed and fabricated for use in this program.

4.4.1 Test Basin Design

The design of the test basin took advantage of insights gained through work by other researchers who have performed in-laboratory GPR experiments [126–128]. Their work was particularly valuable in highlighting means to manage water/liquids in a test apparatus, defining appropriate dimensions for an effective in-laboratory test setup, and managing air-launched GPR antennae when working at a laboratory scale.

Even with the benefit of past studies, effort was placed on ensuring that the test basin used here was appropriately sized and designed. The main concern here is the potential for the walls of the vessel to create side reflections of electromagnetic (EM) energy that could interfere with observations of targets in the test medium. In addition, several other factors associated with the design of the test basin can influence the data collected by GPR, such as the material from which it is fabricated, and the nature of the soil, aggregate, and roadway materials that it contains.

To assess these variables simulations were carried out using the GPRMAX2D software described above. Simulations performed encompassed the following ranges of key variables:

1. Since the depth of drainage conduits below pavement is normally in the range of 0.5m to 1m, initial simulations were performed assuming a depth of 1m which provides a conservative bound for basin design.

2. Several potential fabrication materials were considered for the experimental basin, such as, (1) a simple metal box, (2) a simple wooden box and (3) a canvas box supported by round metal bars. (Note that steel was used as a test material to verify model function based on steel's "mirror-like" reflection of electromagnetic waves).

3. Finally, several key boundary conditions associated with selected basin materials were also explored. Possible boundary effects caused by the use of a test basin could include, (1) sidewall reflections (e.g. from the walls of a metal box), (2) bottom reflections (e.g. from a steel support plate below the basin), (3) support reflections (e.g. from metal bars used to support a canvas box) and (4) corner reflections (e.g. from the edges of the basin).

To explore possible designs, three different basin sizes were analyzed involving differing width to depth ratios and different wall materials as summarized in Table 4.2. Figures 4.5 (a)–(c) illustrate the geometries of the three simulated models. In these simulations, the GPR antennae are simulated to move along the surface of the experimental basin, and the data collection rate is 1 trace per 0.03 meters. Moreover, there is no offset between transmitter and receiver in these simulations because it is assumed that they are performed with a standard Tx/Rx antenna unit, in which the transmitting and receiving antennae cannot be physically separated.

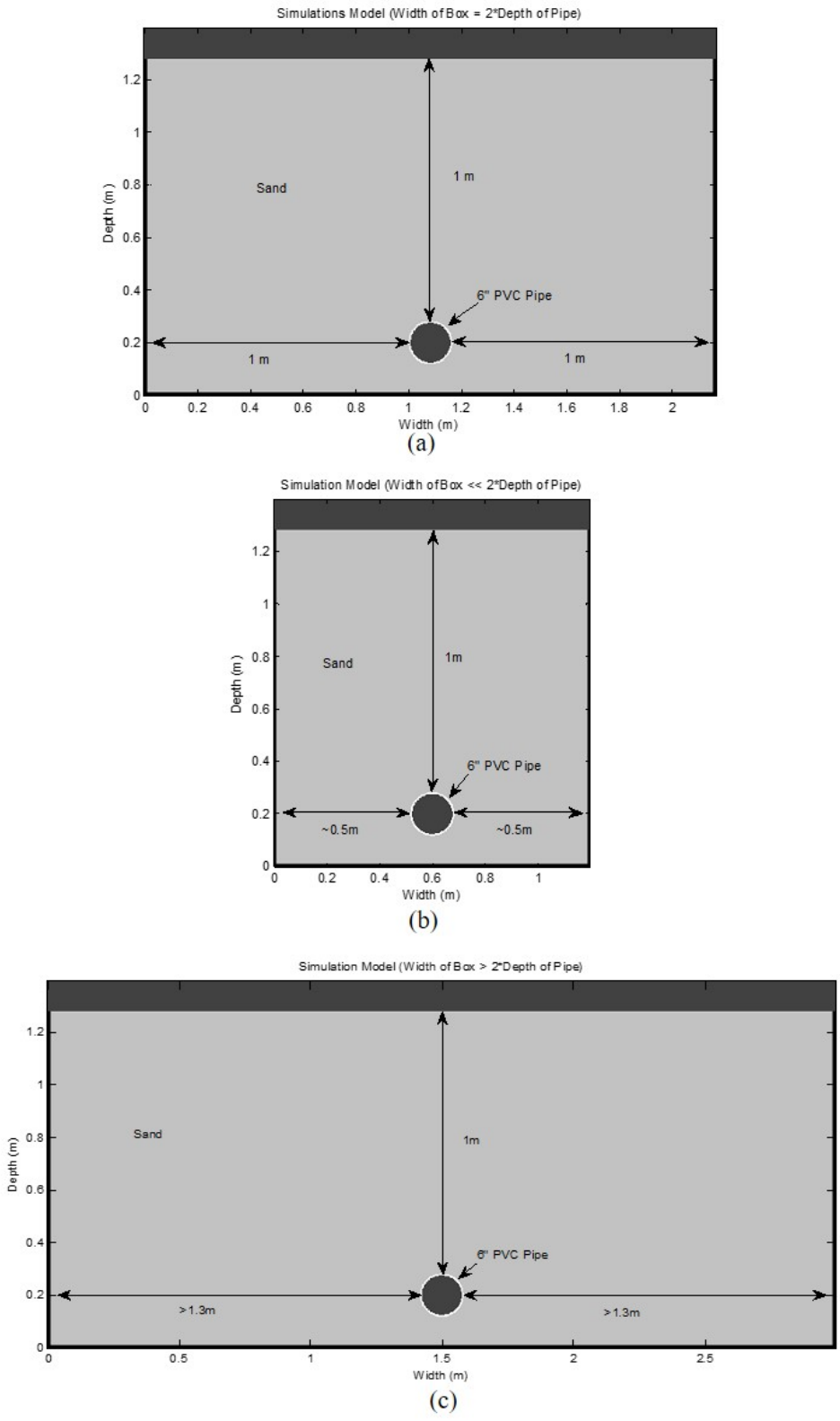

Figure 4.5.: Geometries of simulated models for lab experimental basin size determination

In general, the results of the simulations generated based on the factors above can be expressed as a function of 1) the fabrication material and dimensions of the designed basin and 2) the operating frequencies of the GPR antennae (400 MHz and 900 MHz).

Table 4.2.: Simulation Parameters for Experiment Basin Size Determination

Model	**Descriptions**	**Basin Sidewall Material**	**Antenna Frequency (MHz)**	**Result Figure No.**
A	W = 2D *	Metal	900 MHz	Figure 5-6 (a)
			400 MHz	Figure 5-6 (b)
B	W >2D	Metal	900 MHz	Figure 5-6 (c)
			400 MHz	Figure 5-6 (d)
C	W «2D	Metal	900 MHz	Figure 5-6 (e)
			400 MHz	Figure 5-6 (f)
		Canvas / Dry Wood	900 MHz	Figure 5-6 (g)
			400 MHz	Figure 5-6 (h)

* W = Width of designed basin; D = Depth from surface to the top of target pipe

Simulation results for the different models are shown in Figure 4.6 (a) – (h) as follows.

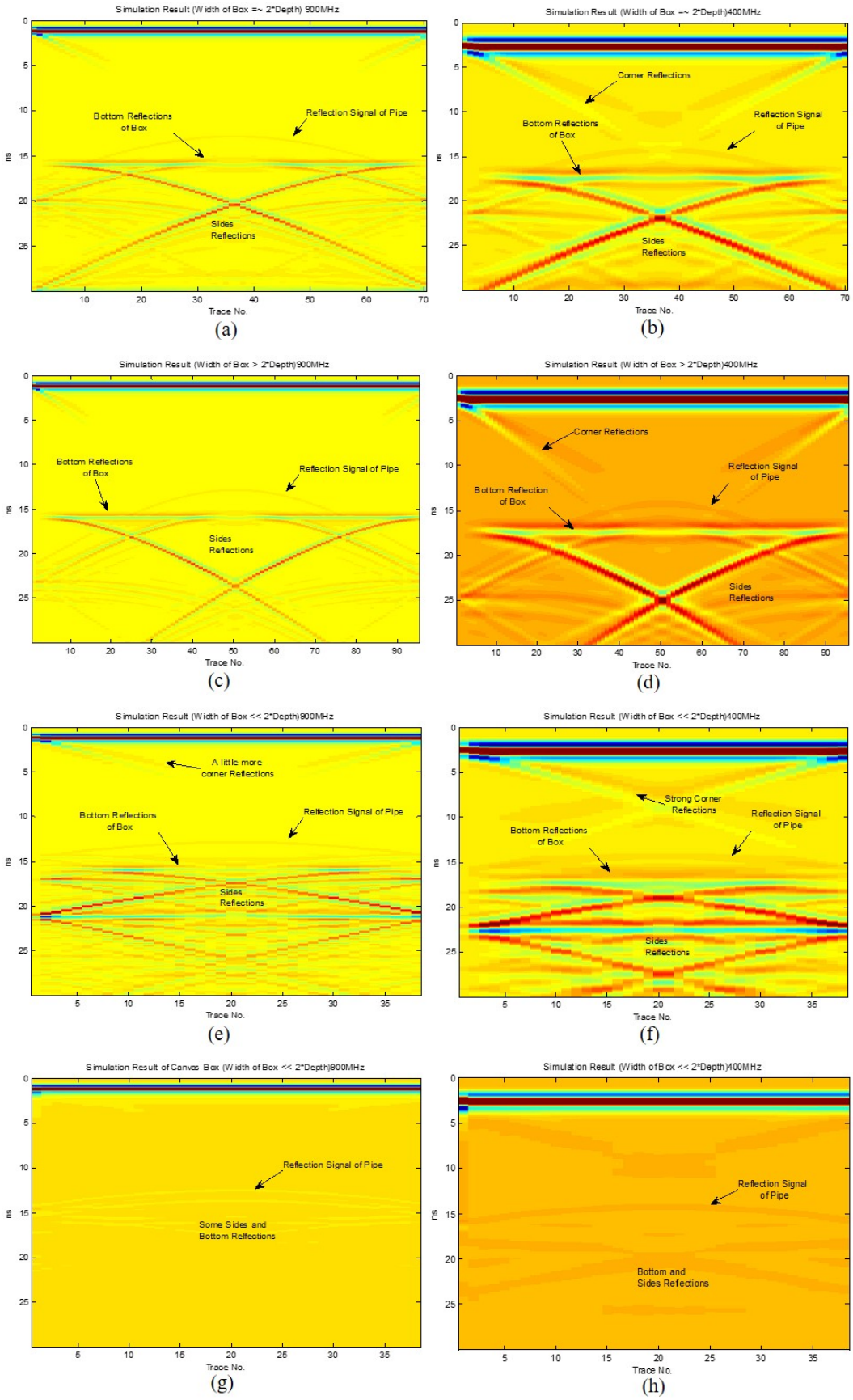

Figure 4.6.: Results of basin size simulations

Several findings are notable from above:

- Recognizing that the EM radiation emitted from the GPR antenna will obey Snell's Law when interacting with an EM reflective surface, the reflections of flat walls and round support bars would be expected to follow very different paths, as discussed in detail in the following paragraphs.

- In nearly all of the simulations, side reflections of emitted EM radiation appear at the transceiver after the bottom reflection since reflections must obey Snell/s Law, and will thus not influence the pipe reflection signal (see Figure 4.7). Even for the smallest basin (Model B), the side reflections still arrive after the bottom reflection, although there is evidence of some convolution when a 400 MHz antenna is employed. The same is true for the signal reflected directly from bottom of the basin.

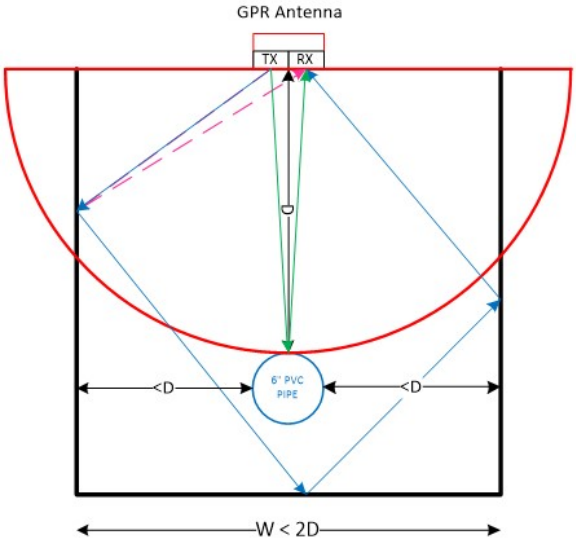

Figure 4.7.: Illustration of side reflections vs. pipe and bottom reflections in test basin simulation

- Comparison of the 400MHz (Figure 4.6 (b) (d) (f) (h)) and 900MHz (Figure 4.6 (a) (c) (e) (g)) antenna simulations indicate that corner reflections are much stronger when the 400MHz antenna is employed. In Figures 4.6 (b) and (d), corner reflections can be observed that are strong enough to influence the return signal from pipe, which

could lead to errors in a real test. This problem is particularly pronounced in Figure 4.6 (d), in which the corner reflections cross above the signal from the pipe – creating a signal that could be misinterpreted as another parabolic reflection from a pipe. These reflections likely stem from the upper structural edge of the test basin.

- The size of the test basin remains as the most important factor in producing a field representative in-lab test setting. For the smallest model (Model C), side reflections are much more complicated than the other two larger sized models, which significantly complicate target signal determination. This problem is compounded with the 400MHz antennae, as shown in Figure 4.6 (e) (f). However, different basin materials can influence the side effect significantly. The wooden or canvas basic reduces these reflections enough to analyze buried pipes based on the smallest size design above (Model C), as shown in Figure 4.6 (g) and (h).

Based on the analysis above, a simple wooden box, slightly elevated above the floor, was used as the lab experimental test basin in this project. Details of this lab test basin will be introduced as necessary in subsequent sections of this thesis.

4.4.2 Test Basin Preparation Procedures

Based on the key parameters indicated above, the test basin must be filled with controlled materials before an experiment is conducted. The general procedures for this activity are as follows.

1. Choose the cross-section of pavement that is to be simulated, such as the shoulder, pavement surface, or side slope;

2. Design this selected cross-section based on the road design manual, employing different materials for the various base layers as required; for example for the side slope of the pavement, drainage pipes would be buried only by soil, but not gravel layers and a top pavement surface;

3. Determine desired water conditions in the soil based on the desired real field conditions; such as saturated after rainy weather, dry conditions in the high temperature period of summer, or intermediate partially saturated conditions;

4. Design pipe positions, depth and line directions; outlet drainage pipes would appear at different positions and depth based on which part of road is simulated; meanwhile, the choice of the pipe line direction in this limited sized basin can be varied to simulate different survey line angles (parallel, perpendicular and angle α);

5. Place all controlled materials into the test basin in the appropriate order: base sand, pipes with defined direction located at determined depth, gravel sub-base, gravel base and top pavement surface (if necessary);

6. The cross-section is now ready for testing.

4.4.3 Test Basin Data Set

The test basin was employed in this work for a variety of proof testing activities and to develop data sets representative of desired field conditions that were not necessarily available or readily accessible in the field. While the majority of analyses discussed herein will focus on actual field data, laboratory acquired data is referenced where additive to the discussion.

4.5 Acquisition of Field Data

Multiple field surveys were performed in this research to acquire data sets from actual roadways in Indiana. For field tests, road cross-sections where the locations of subsurface pipes are well known and also marked were examined to facilitate data interpretation. Three types of drainage conduits can be encountered in the field, (1) transverse pipes, (2) longitudinal edge pipes, and (3) outlet pipes. Figure 4.8 provides a schematic of drainage system geometry and typical survey paths.

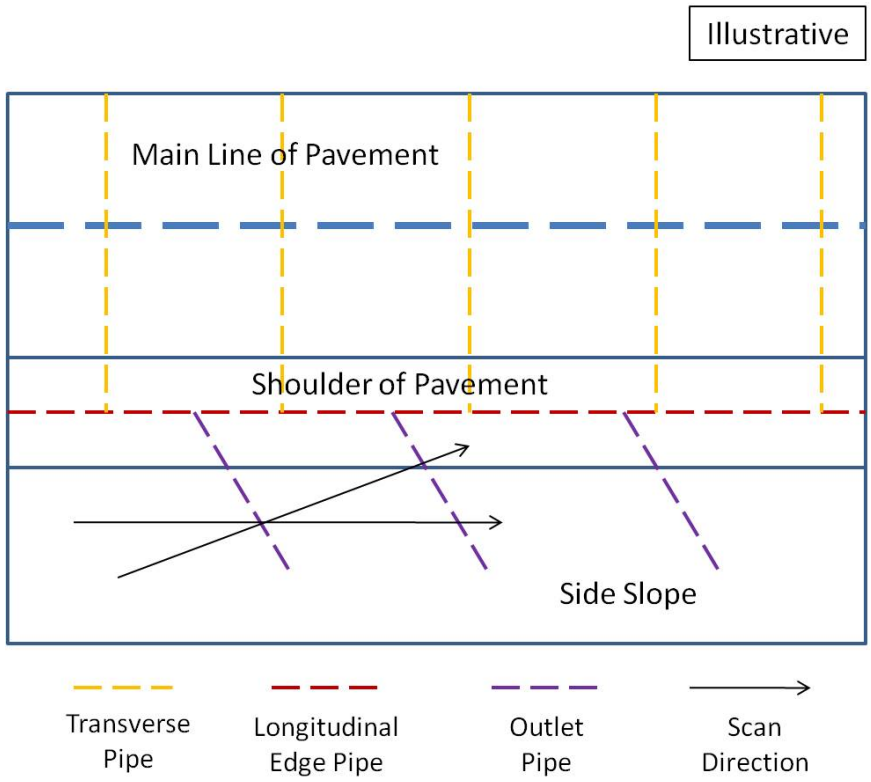

Figure 4.8.: Schematic plan-view illustration of drainage system configurations

The outlet pipes on the shoulder and side slope of the pavement are considered the primary target in this work. Several of these data sets will be employed in this report to illustrate key analyses and findings:

- Route US-231: Here the survey line was about 3/4 miles long. There were 4 PVC pipes (1 $8''$-diameter pipe and 3 $4''$-diameter pipes) involved in this test. Two antennae were used here, one 400MHz antenna and another 900MHz antenna.

- Route I-65: The survey line of this test totals approximately 4.5 miles. Two types of drainage pipes were detected in this test, X-drains (newly installed, shallow PVC pipe) and K-drains (old deeply buried metal pipe). Here 4 antennae were employed, two 400MHz antennae and two 900 MHz antennae.

- New Route US-231: The survey line for this test was about 1/4 mile long. There are two PVC pipes involved. The main purpose of this test was to examine different an-

tennae configurations in the field. Both the original SIR-20 and SIR-30 GPR systems were used during this work. In total three different operating frequencies were tested here, 270MHz, 400MHz and 900MHz. Four antenna configurations were examined in this work as well.

4.6 Summary

In this chapter, an overview of functions, properties and components of the GPR system used in this research is performed in detail. Moreover, the design and operating procedures of laboratory and field experiments are also introduced carefully. Collection of high quality GPR data is the key factor to obtain an accurate detection result in the further analyses, which is highly related to the efficiency of test designs.

5. THEORETICAL SIMULATIONS

5.1 Introduction[1]

In this section, a series of GPR simulations were carried out using GPRMAX2D software (©2005 by Antonis Giannopoulos) – a simulator based on the Finite-Difference Time-Domain (FDTD) method - to explore the influence of road cross-section designs on radar signatures, and evaluate the effectiveness of alternate GPR antennae configurations. Simulations offer the advantage of modeling situations with infinite boundary conditions, which eliminates the influence of even subtle side or bottom reflections that might be encountered in a scaled down laboratory experiment that must inevitably be "contained".

GPR simulation methods have been widely used by researchers in an array of application areas. A number of different methods have been developed, such as ray-based approaches [76,143,144]; frequency-wave-number computations [145], and finite-differencing time-domain (FDTD) methods [134, 146, 147]. The simulation methods have also been applied in many contexts. Zeng and McMechan [134] set up a GPR simulation model for tank/pipe detection employing a ray tracing approach, from which it was possible to define a basic view of pipe detection via GPR including, 1) primary signal shape, 2) key factors affecting detection results and 3) approach of data acquisitions. Bourgeois and Smith [148] compared a full 3D GPR simulation result based on FDTD method with real field measures. And the comparison showed a very positive conclusion with this numerical analysis.

5.2 Simulation Models

Two sub-pavement models were simulated in this work. Both models were designed to represent a Portland cement concrete pavement (PCCP) road cross-section, with a concrete

[1]This chapter is mainly based on the published conference paper "Simulation Analysis For Under Pavement Drainage Detection By Ground Penetrating Radar (GPR)" [142]

layer depth of $\sim 280mm$, a gravel base of $\sim 180mm$, and sand sub-base. The dimensions of the simulated area ($3m(L) \times 2m(D)$) were chosen to be large enough to get all the possible reflections from the pipe target and minimize the influence of boundary conditions. Side and bottom boundary conditions for the calculation area were absolved infinite boundaries. In addition, a free boundary was modelled at the surface.

The first model included a single drainage conduit, with diameter of $4''$, $6''$ or $8''$ ($0.1016m$, $0.1524m$ and $0.2032m$), installed at a depth of $0.6m$, which is a reasonable depth based on typical road cross-section design, as shown in Figure 5.1(a). This was the main simulation model employed to simulate target signals under different test conditions.

The second model, depicted in Figure 5.1(b), was a reference model without any pipe installed. This model was designed as a background condition for comparison with the primary model. The main purpose of this model was to simulate the exact conditions of Model 1 in every simulation group, but without drainage involved, thus providing a background signal at the pipe area that could be used for comparison with the primary model. Effectively, the result of Model 2 was used to subtract background signals from Model 1, so that only the target reflection signals would be left for interpretation.

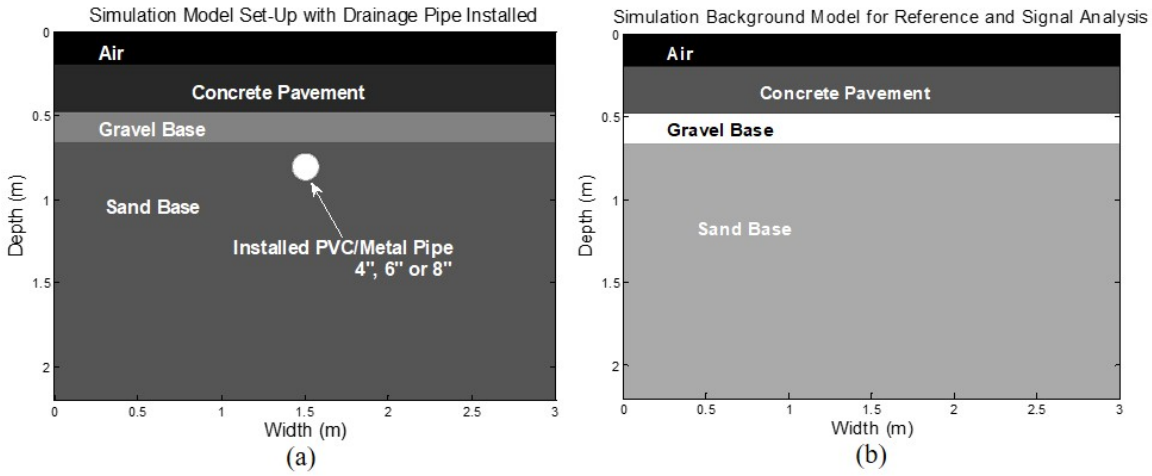

Figure 5.1.: Schematics of Simulation Models: (a) Normal Road Cross Section Model with Drainage Pipe Installed (b) Background Reference Model for Reference

All simulations were performed assuming use of a 400MHz transmitter receiver dipole antenna pair, given the common use of this frequency in practice. The GPR antennae were simulated to move along the ground surface in the simulation models from left to right. Data collection was defined as one trace per 0.0254 meters (about 12 traces per foot). In order to examine the optimal antenna offset under different circumstances, eleven different offsets (along the horizontal direction) between the transmitter and receiver were considered (0m – 1.5m).

While these models were obviously simplified relative to an actual road cross-section, they help to assess fundamental geometric and material impacts on different GPR test configurations. In particular, several groups of simulations were analyzed for each model as described below.

5.3 Analysis Methodology and Approach

Key factors studied in the simulations included: pipe size, pipe material, sand moisture conditions, pipe drainage conditions, and antenna offset. The simulated pipe size was chosen as $4''$, $6''$ or $8''$ ($0.1016m$, $0.1524m$ and $0.2032m$), which are very common drainage pipe sizes installed under highways. Both PVC and metal pipe were analyzed. Although new installed pipes are most often made of PVC, some old pipes are metal and still in service in many highway settings. As noted above, sand was assumed as the sub-base condition in this study, and both dry and wet conditions were analyzed. Two drainage conditions were explored:active (pipe full with water) or inactive (pipe empty). Finally, to explore the optimal offset between the transmitter and receiver under different environmental conditions, the offset was varied to be 0m, 0.1m, 0.2m, 0.3m, 0.4m, 0.5m, 0.6m, 0.7m, 0.8m, 1.0m and 1.5m.

To explore the above key factors, a number of simulations were performed. For example, one simulation of Model 1 employed the following factor values: 400MHz GPR operation frequency; 0.1m offset between transmitter and receiver; $6''$ PVC pipe with no water being drained; dry sandy soil around installed pipe. In order to get the accurate detection

signal from this simulation, a reference background simulation of Model 2 was analyzed as well, which employed similar factor values but without any pipe installed: 400MHz GPR operation frequency; 0.1m offset between transmitter and receiver; dry sandy soil around installed pipe. Every simulation of Model 1 was paired with a background simulation of Model 2 for reference and further analysis.

In order to get the best understanding of GPR performance for target detection, four quantitative metrics were calculated based on the simulated GPR results. The four metrics were: 1) signal to background ratio (SBR) in dB; 2) signal to receiver noise ratio (SNR) in dB; 3) signal energy in Volts; and 4) average signal band power in Watts. Several steps were taken to calculate these metrics.

Step 1: Perform the simulation based on Model 1

Perform a simulation with selected environmental factors and analysis information based on Model 1 with a pipe (target) installed. Obtain the signal matrix which includes both pipe reflection signals and background environmental signals in the analyzed area, which can be written as matrix $[S]$.

Step 2: Perform the simulation based on Model 2

Perform the paired simulation based on Model 2 without the drainage pipe (target) installed, but keep all other factors the same as in the paired Model 1, such as antenna frequency, antenna offset, soil type and moisture condition, ensuring that the obtained signal matrix was exactly the same size as that obtained from Model 1 Obtain another signal matrix which includes only the background environmental signals, which can be written as matrix $[B]$.

Step 3: Subtract the background signals from the general received signals

In order to obtain the signals caused only by the target pipe (target), the background signals were subtracted from the general signal matrix, which can be expressed as a new matrix $[TS]$, where,

$$[TS] = [S] - [B] \tag{5.1}$$

Step 4: Calculate four metrics of the target signals

As introduced above, there were four metrics used to assess GPR performance: 1) signal to background ratio (SBR) in dB; 2) signal to receiver noise ratio (SNR) in dB; 3) signal energy in volts; and 4) average signal band power in watt.

Now, based on the target signal matrix $[TS]$, the four factors were calculated column by column (signal by signal). Then four factor matrices would be generated at the end of calculation. The calculation details for each metric are as follows.

1. signal to background ratio (SBR) in dB;

   First, calculate the average single column of signal based on the background signal matrix $[B]$.

   $$(b_j) = mean([B(:, j)]) \tag{5.2}$$

   Second, subtract the average background signal (b) from every trace (column) of the background signal matrix $[B]$ to generate a new subtracted background signal matrix $[NB]$, such that,

   $$[NB] = [B(:, j) - (b_j)] \tag{5.3}$$

   Finally, calculate the signal to background ratio (SBR) column by column (signal by signal) based on average signal band power, and generate the $[SBR]$ vector.

   $$[SBR(j)] = Power([TS(:, j)])/Power([NB(:, j)]) \tag{5.4}$$

2. signal to receiver noise ratio (SNR) in dB

   As introduced, the operating frequency of the simulated antenna was 400MHz in this study. The receiver noise power (np) was estimated based on a 400MHz Ricker pulse; consider the noise bandwidth about 400MHz with 10dB at 300K degree, which should be the normal specifications for receiver noise bandwidth. Then, the signal to

receiver noise ratio (SNR) was calculated column by column (signal by signal) based on average signal band power, to generate the $[SNR]$ vector.

$$[SNR(j)] = Power([TS(:,j)])/np \tag{5.5}$$

3. signal energy in Volts

   Based on the target signal matrix $[TS]$, the energy of every single column (signal) was calculated. Then, an energy vector $[ES]$ was built for this target signal matrix.

$$[ES(j)] = sum([TS(:,j)]^2) \tag{5.6}$$

4. average signal band power in Watts.

   Based on the target signal matrix $[TS]$, the average band power of every single column (signal) was calculated. Then, an average power vector $[PS]$ was built for this target signal matrix.

$$[PS(j)] = bandpower([TS(:,j)]) \tag{5.7}$$

Step 5: Calculate the maximum value of each analyzing factor

In order to easily compare the GPR performance under different circumstances, the maximum values of each metric for each simulation were selected to facilitate the final analysis and discussion.

5.4 Simulation Results and Discussion

As introduced above, four key metrics were calculated to describe GPR performance in the investigated under pavement pipe detection scenarios. Figure 5.2 shows signal strength metrics for different pipe sizes, soil conditions and antenna offsets, which highlight the optimal offset of transmitter and receiver under different GPR performance situations.

Based on the plots in the above figures, several findings can be highlighted:

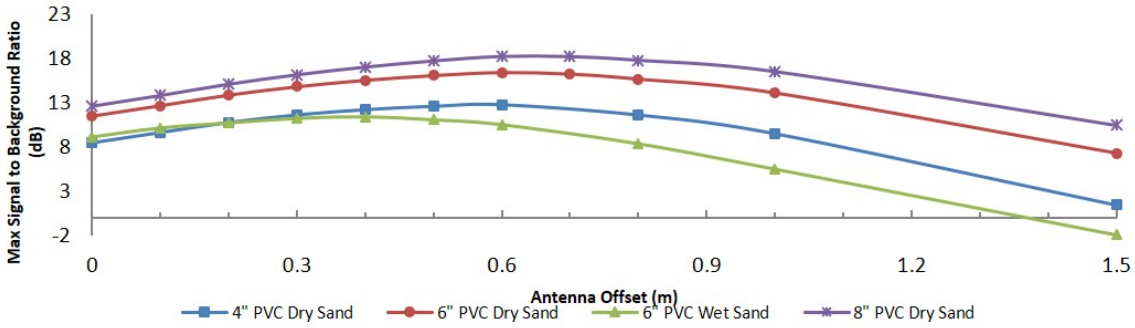

Figure 5.2.: Max Signal to Background Ratio (SBR) at Different Antenna Offset

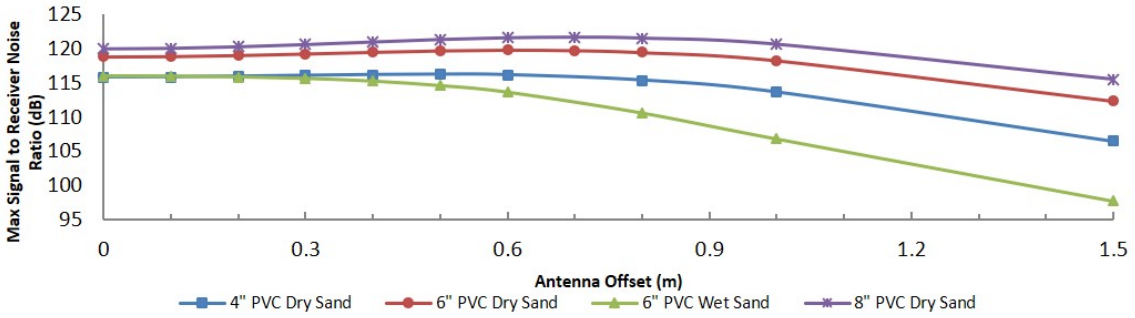

Figure 5.3.: Max Signal to Receiver Noise Ratio (SNR) at Different Antenna Offset

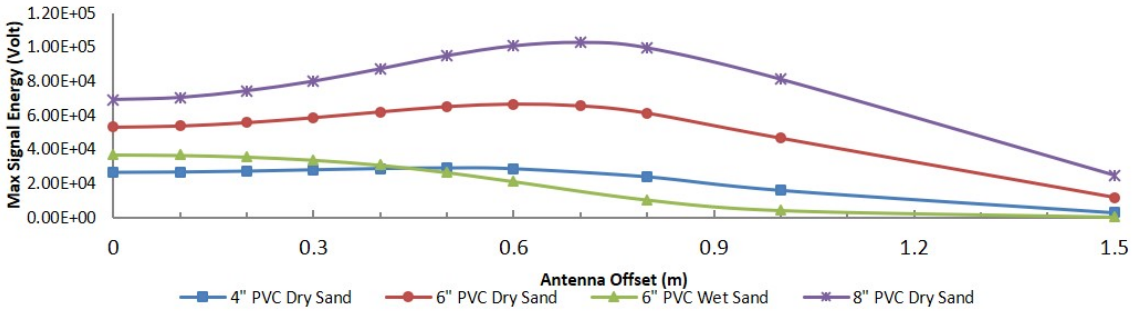

Figure 5.4.: Max Signal Energy Level at Different Antenna Offset

- Detection signals are stronger when the soil surrounding the buried conduit is dry than when the soil is wet, because the EM wave was hard to transmit into the wet materials.

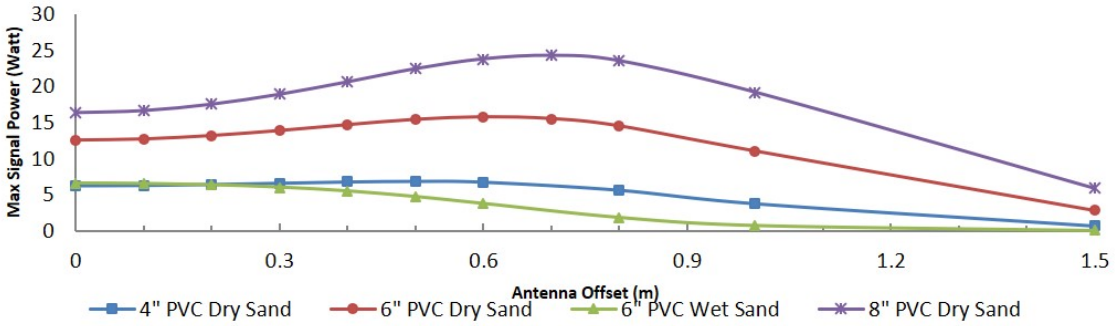

Figure 5.5.: Max Average Signal Band Power at Different Antenna Offset

- Increased target size obviously improved target signal strength. Furthermore, the size of target also influenced the optimal offset at the same environmental conditions. From the signal energy and power plots (Figure 5.4 and 5.5), it could easily be determined that the optimal antenna offset increases when the target size is larger. As shown, for the dry sand condition, the optimal detection offset for $4''$ pipe detection was about 0.5m; the optimal detection offset for $6''$ pipe detection was about 0.6m; and the optimal detection offset for $8''$ pipe was about 0.7m.

- The moisture level of soil surrounding a buried conduit also significantly changes the optimal offset. For instance, for the $6''$ PVC pipe under dry sand condition, the optimal detection offset was about 0.6m. But when the $6''$ PVC pipe was in the wet sand condition, the optimal detection offset dropped significantly. Based on the Signal to Background Ratio, the optimal offset for the wet condition was about 0.4m. And based on other three factors, the optimal offset dropped to around $0 \sim 0.1m$.

Besides the analysis of antenna offset, the influence of pipe material and drainage conditions (empty or full with water) was also explored herein. Take a simulation example of $6''$ pipe with 0.1m antenna offset to discuss the above aspects. And several interesting findings could be generated as follows:

- Not surprisingly, the signal from metal pipe is much stronger than from the PVC pipe. As shown in Figure 5.6, for the condition of dry sand with an empty drainage

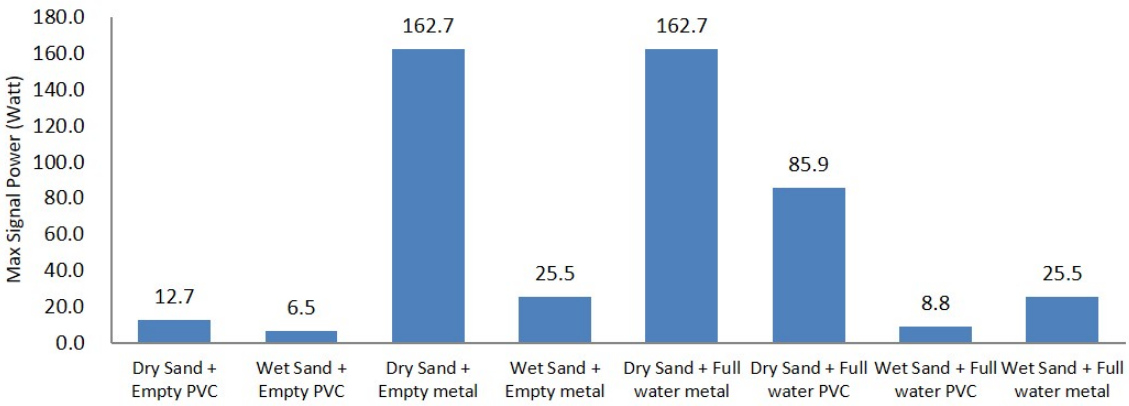

Figure 5.6.: Simulation Results of different subsurface conditions ($6''$ pipe and 0.1m antenna offset)

pipe, the power of the PVC pipe signal was about 12.7 Watts, while the power of the metal pipe signal increased to /162.7 Watts.

- The water condition of soils surrounding a conduit can significantly influence signal power levels. For example, the signal power from metal pipe in dry sand was about 162.7 Watts. But this value decreased to 25.5 Watts in the wet sand condition.

- Pipe drainage condition (empty or full with water) has a significant impact on detection of PVC pipes, but has little impact on detection of metal pipes. As shown in the figure, for the wet sand condition, when the pipe was full of water, the signal power was 8.8 Watts versus a value of 8.8 Watts with an empty pipe, a moderate change. This influence was more significant when the surrounding soil condition was dry. The values would become 85.9 Watts (dry sand + full drained water) and 12.7 Watts (dry sand + empty pipe). In the case of the metal pipe, the drainage condition had no influence - whether the pipe was full of water or empty, the signal power stayed at the same level.

5.5 Summary

Several simulations of sub-pavement drainage conditions similar to common settings found in the field were performed and analyzed in this section. According to the descriptions above, key conclusions are as follows:

1. The presence of water is a key factor in determining the potential to detect sub-pavement drainage conduits in the field using GPR, and can drive a significant reduction in sensitivity.

2. The optimal antenna offset for pipe detection is influenced by the target pipe size; the larger the target pipe, the greater the optimal offset.

3. Surrounding soil moisture levels significantly change the optimal antenna offset value.

4. Pipe material has a significant effect on detection signal strength. The signal from metal pipe detection is likely to be much stronger than the value for a PVC pipe, under the same environmental conditions.

5. Pipe drainage condition (empty or full with water) plays an important role in the detection of PVC pipes, but has little impact in the detection of metal pipes.

6. BACKGROUND REDUCTION METHOD TO LOCATE UNDERGROUND PIPES

6.1 Introduction[1]

This chapter builds on the comprehensive study discussed above that highlighted potential avenues to improve GPR detection of sub-pavement drains [150] and puts forward a novel background noise and clutter reduction method for GPR to enhance target signals in what amounts to a constructed environment that tends to have more consistent subsurface properties than one might encounter in a general setting. Within this technique, two major algorithms are employed. Algorithm 1 is the core of this method, and plays the role of reducing background noise and clutter. Algorithm 2 is supplementary, and helps eliminate anomalous discontinuous returns generated by the equipment itself, which could otherwise lead to false detection indications in the output of Algorithm 1. Instead of traditional 2-D GPR images, the result of the proposed algorithms is a 1-D plot along the survey line, highlighting a set of "points of interest" that could indicate buried drain locations. Details of the method and its application to the analysis of GPR surveys conducted on stretches of highway in Indiana in the United States are presented below.

6.2 Overview of background noise and clutter reduction methodology

One advantage of GPR is the potential to detect non-metallic targets. However, the strength of the reflection signals from non-metallic targets is significantly weaker than that obtained from metallic targets of equivalent dimension and position. Further, useful information about the target may be obscured by the background signal, typically termed clutter and noise in radar theory. Background clutter and noise normally includes three compo-

[1]This chapter is mainly based on the published peer reviewed journal paper "Improved background and clutter reduction for pipe detection under pavement using Ground Penetrating Radar (GPR)" [149]

nents: the breakthrough signals directly from transmitters to receivers; the reflections from the air-ground interface as well as the interfaces of different layers in the pavement and subsurface; and the scattered signals from other non-related targets, such as rocks, air voids or unknown discontinuities in the subsurface [151]. As a result, one of the key problems addressed in the work presented herein is differentiation of the scattered signal of potential targets from background interference, because the targets here are primarily non-metallic (PVC or clay) drainage pipes.

In order to reduce the clutter information and enhance target detection in the GPR field survey, several approaches have been put forward. Some involve physical alteration of the antenna system. For example, rather than using a traditional single transmitter and receiver antennae, a number of researchers improved the GPR signal and reduced the background noise by employing different antenna configurations. Cedrina et al. [152] presented a detailed study to improve the continuity and amplitude level of a GPR signal using a synthetic emitter array; Bai and Sinfield [45] introduced another approach to enhance the signal strength by using a group of frequency shifted antennae; Liu et al. [153] developed a hybrid dual-polarization GPR system, which makes use of one circularly polarized transmitting antenna and two linearly polarized receiving antennas to improve the detection of an elongated pipe-like target and to estimate its orientation angle. Alternatively, other researchers have focused on signal processing methods for background clutter and noise reduction in GPR data sets, such as: simple mean scan subtraction [154]; complex average subtraction [155]; moving average background removal [156]; a Kalman Filter-Based approach to Target-Background Separation [157]; background removal using Singular Value Decomposition (SVD) (SVD) [151], Eigenvalues [158]; the likelihood ratio test [154, 159]; the whitening filter [160]; the median filter [156]; the fuzzy weighted background removal and target energy function approach [161, 162]; the method of generalized S transformation with optimized parameters to enhance the signal level [163]; and the wavelet-based method [164, 165]. These methods are certainly valuable for general data sets but do not capitalize upon material and structural consistencies typically present in constructed systems, as discussed herein.

Plastic pipes, the primary targets in this research, have long been considered a detection challenge in of field GPR. Ayala-Cabrera et al. [118] introduced an approach to automatically locate plastic pipes by rebuilding a GPR image to clean and improve radargrams based on wave amplitude values (WAV) which enabled auto-selection of image zones indicating plastic pipes through multi-agent processing. Relatedly, Curioni et al. [111] conducted a comparison study of GPR signal levels and noise characteristics of plastic utility pipes under varying seasonal conditions to inform detection decisions.

Further, Rashed and Harbi [166] presented a matrix background subtraction method to improve the single average subtraction method; and Montiel-Zafraetal. [167] generated a background noise removal method based on the similarity of non-neighboring regions. In contrast to the above, the algorithm used in this effort is a unique variant of a moving average background subtraction method, which is developed as outlined below to take advantage of the unique characteristics of constructed pavements and associated embankments to enhance target detection.

In this chapter, two signal processing algorithms are employed: First, a moving window background and clutter reduction method is applied to collected GPR data; second, a matrix data element analysis is employed to reduce the influence of data anomalies. The first algorithm, Algorithm 1, is a variant of a background and clutter reduction (subtraction) method which is focused on interpretation of 1-D GPR results derived from the original 2-D GPR image data collected along the survey line as a function of distance. While notably less complex than 2-D image analysis, it is believed that this treatment provides an improved indication of the presence of underground conduits below constructed pavement, which due to common engineering practice involve somewhat consistent preparation of subsurface materials. In addition, the second algorithm, Algorithm 2, is actually a statistical analysis intended to reduce anomalous signals collected in the original GPR images. This algorithm examines the original 2-D GPR data set as a matrix and examines the percentage change in neighboring horizontal elements and the cumulative standard deviation of whole neighboring columns of data. In a manner similar to the first algorithm, the output of the second algorithm is plotted in 1-D as a function of distance along the survey line. The

final result of a GPR scan is thus the combination of the outputs obtained by these two algorithms. Figure 6.1 represents a general flowchart of introduced algorithms.

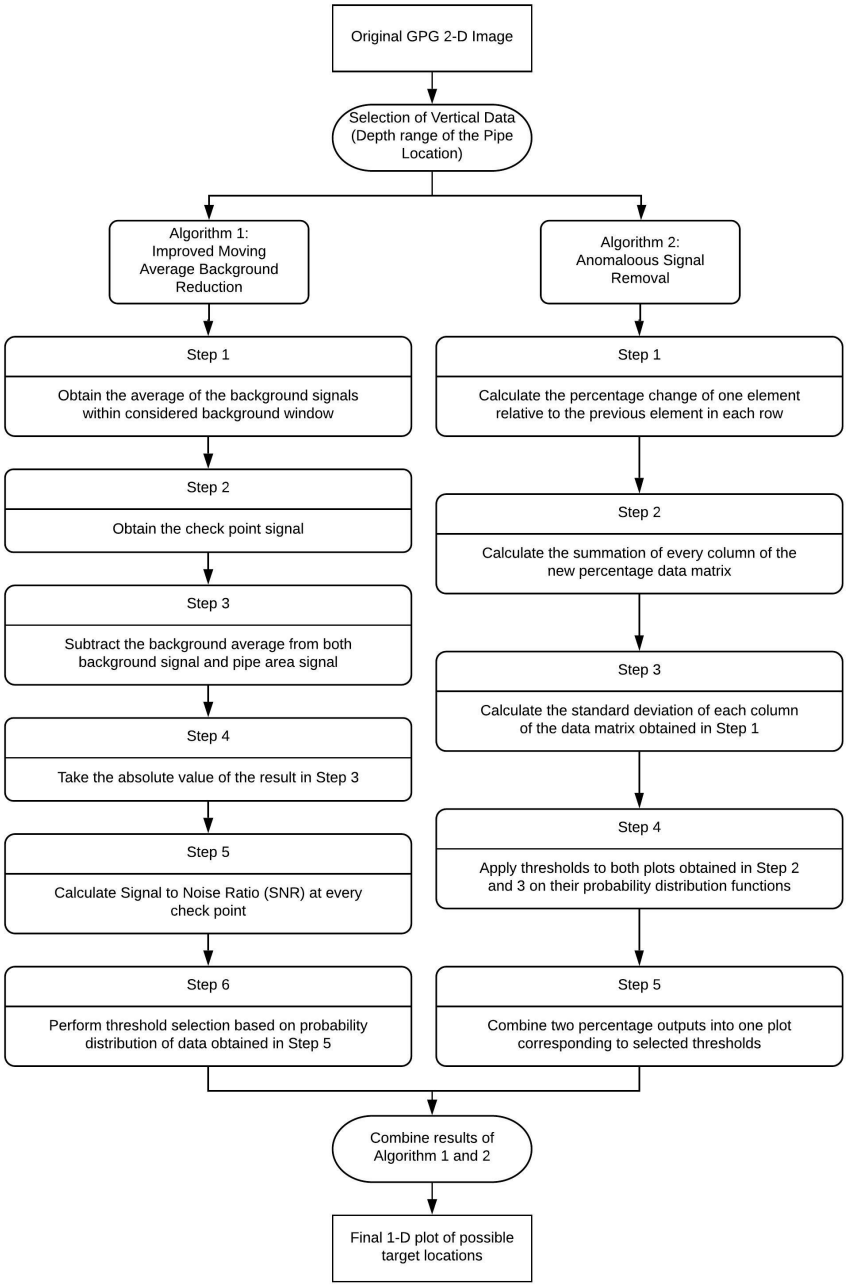

Figure 6.1.: Flowchart of Improved GPR Background Reduction Algorithms

The above outlined data interpretation methodology has been implemented through the development of a custom data analysis program. The program produces two major types of output based on the different algorithms: 1) GPR signal to noise ratio (SNR) values and 2) vertical sums of the percentage change in the GPR signal at measurement points along the horizontal survey line. By considering the probability distribution of obtained results, a detection threshold that effectively establishes the sensitivity of the system is defined. Numbers of detected target conduits and false alarms in a given GPR survey line are also compared in sets of lab and field data to obtain preliminary views of optimal program parameters. Finally, multi-frequency results obtained along the same survey line are compared and combined in order to provide a final pipe position output with higher probability along any given survey line than searches for 2-D hyperbolic signals alone. Details of this methodology and related analyses are described in the following sections.

6.3 Pre-Processing and Selection of Vertical Data Analysis Interval

GPR data is normally obtained in the form of a B-Scan radar image (Figure 6.2), and can be interpreted as a matrix. Each column of the matrix is a digitized single trace of a scan, which is a so called A-Scan in Radar theory. Figure 6.2, illustrates a typical GPR reflection signal from a scan of a sub-pavement drain performed along a survey line orthogonal to a buried pipe. The hyperbola shape located approximately halfway across the upper 1/3rd of the image indicates the position of the buried conduit. Importantly, the drain is likely to be detected in a very specific range of depth below the pavement assuming drainage pipe placement has been guided by accepted design principles. Consequently, only a limited vertical interval of a GPR data set must be analyzed to detect conduit targets in a sub-pavement analysis scenario. While this of course varies based on the design of a specific roadway, normally, drainage pipes are buried 0.5m to 1m under the surface of pavement in order to properly perform their intended function. Thus the uppermost region of the data (the pavement and base layers), and data below a depth of approximately 1m can be ignored. For example, in Figure 6.2, the pipe is detected around 10ns along the

vertical axis, which corresponds to a depth of 0.5m. Furthermore, each A-Scan of a data set is digitized into 512 samples. In other words, there are 512 rows in the final data matrix, which could be plotted in a 2-D image as shown. Thus for each A-Scan, only samples 50-200 (row 50-200) are selected from the data set and used in the analysis performed herein, which is shown as the range between the two dashed horizontal lines in Figure 6.2.

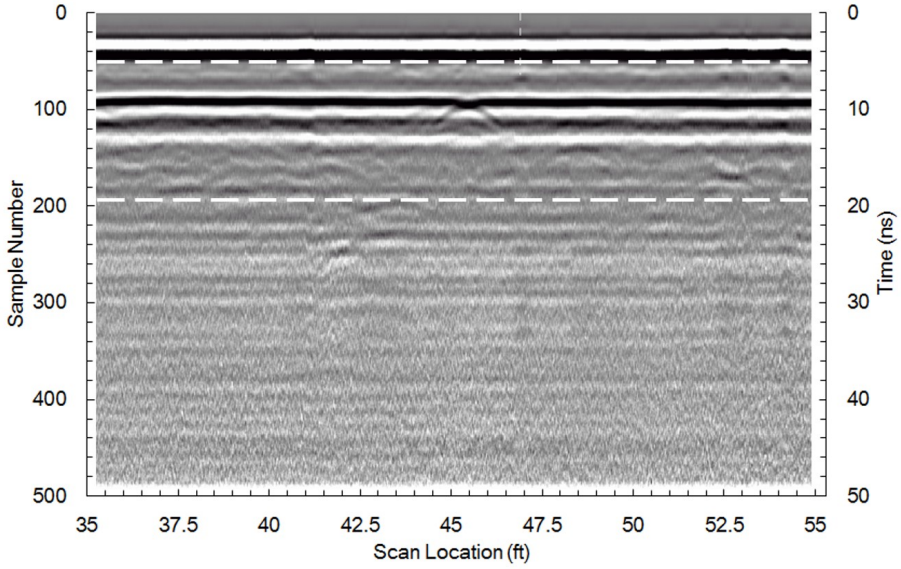

Figure 6.2.: Vertical data selection in a typical GPR image

6.4 Algorithm 1: Improved Moving Average Background Reduction

6.4.1 Overview of Algorithm 1

The method presented here is a moving average background subtraction approach as mentioned above. In this approach, at any given point of signal analysis along a survey line, a point termed the "check point", an averaged A-scan background signature, is subtracted from the A-scan at that point to reveal the signal of interest. The "average" background signature is developed by examining data (a series of A-scans) in a region of finite length, w, along the survey line that is located a fixed column distance, d, behind the check point. This region is called the background window. As the check point is moved forward along

the survey line, the background window remains a fixed column distance, d, behind the checkpoint, trailing the check point in a manner that enhances its local relevance to the ground conditions in the region of the checkpoint. As a result, there are two key parameters related to this method, the size of the window employed to develop a background signature (i.e., the background window size), w, and the column distance between the check point and the end of the background window, d. A conceptual representation of this algorithm is shown as a related mathematical formulation in Equation (6.1).

$$\text{Matrix of GPR data} \Rightarrow \overbrace{\begin{bmatrix} b_{11} & b_{12} & \cdots & \cdots & b_{1w} \\ \vdots & \vdots & \ddots & & \vdots \\ \vdots & \vdots & & \ddots & \vdots \\ b_{n1} & b_{b2} & \cdots & \cdots & b_{nw} \end{bmatrix}}^{\text{size w}} \overbrace{\begin{bmatrix} \ddots & & & \\ & \ddots & & \\ & & \ddots & \\ & & & \ddots \end{bmatrix}}^{\text{checking distance d}} \begin{bmatrix} s_1 \\ s_2 \\ \vdots \\ s_n \end{bmatrix} \cdots\cdots \tag{6.1}$$

(moving direction ⇒; background window)

For any given run of the signal processing algorithm, a set of values for w and d are tested. The parameters w and d are selected based on iterative trial in a scan area containing a known target. Starting values are defined by the likely lateral influence of the response of the maximum anticipated target size (here the width and the depth of the largest drain likely to be encountered).

During the test, the background window starts from the beginning of the data matrix, and the average of the signals within this window is subtracted from a target signal d columns from the end of the background window. Then another window starts from the second column, the target is also moved to the next column, and the same calculation is repeated. The background window and target signal are advanced along the survey line until the entire data set has been analyzed.

6.4.2 Detailed Procedures of Algorithm 1

The main purpose of this algorithm is to find an optimal combination of w and d. Although the whole algorithm contains several loops to perform this calculation, only one entire loop needs to be considered step by step to understand the algorithm.

Step 1 Obtain the average of background signals, $\overrightarrow{b}_m$, within the considered background window.

$$\overrightarrow{b}_m = \begin{bmatrix} \frac{1}{w}\sum_{i=1}^{w} b_{1i} \\ \frac{1}{w}\sum_{i=1}^{w} b_{2i} \\ \vdots \\ \frac{1}{w}\sum_{i=1}^{w} b_{ni} \end{bmatrix} \tag{6.2}$$

The result of the operation above provides a generalized background signature representative of an area that does not contain a pipe, as shown in Figure 6.3(a). Given that the distance between buried pipes in practice greatly exceeds the width, w, of the background window, there is no danger of incorporating a pipe signature in the background that is ultimately subtracted from a target trace.

Step 2 Obtain the check point signal.

The signal at the check point mentioned above is located d columns away from the last trace (column) of the selected background window and will move together with the background window column by column over the entire data set. To illustrate the concept of the proposed algorithm, here a check point signal located in the pipe detection area is selected for illustration purposes (note that this will hereafter be referred to as the pipe area signal for simplicity, although it of course represents only a potential pipe location in actual application). An example of the resulting signal is shown in Figure 6.3(b). Comparing Figures 6.3(a) and 6.3(b), little difference can be seen even when a large pipe (8 in) is detected, before further analysis steps are applied.

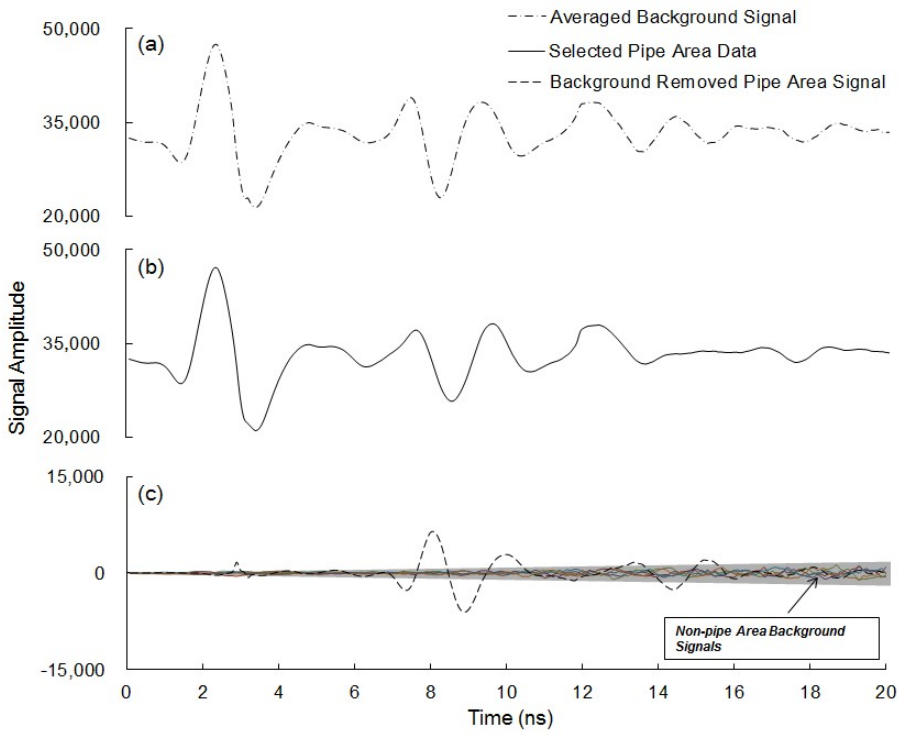

Figure 6.3.: Background Subtraction and Signals Comparison

Step 3 Subtract the background average from both the background signal and the pipe area signal.

$$B' = \underbrace{\left[\overrightarrow{b}_1 - \overrightarrow{b}_m \cdots\cdots \overrightarrow{b}_w - \overrightarrow{b}_m\right]}_{\text{background signals - averaged background signal}} \tag{6.3}$$

$$\overrightarrow{s}' = \underbrace{\left(\overrightarrow{s}_1 - \overrightarrow{b}_m\right)}_{\text{check point signal - averaged background signal}} \tag{6.4}$$

After calculation of the background average, this value is subtracted from each background signal in the current calculated background window and also from the check point signal. As shown in Figure 6.3(c), a new background is produced which displays a reduced amplitude after average subtraction, (shaded area). In contrast, the pipe signal with the background average removed is shown as a dashed line in figure 6.3(c). A significant

difference is clearly seen between the pipe signal and the non-pipe background, compared with the results in Step 2.

Step 4 Take the absolute value of the result in Step 3.

In order to simplify future calculations, absolute values of the results in Step 3 are considered, and the mean value and standard deviation of the absolute new background are also calculated for each row.

The absolute value of the pipe area signal with background removed is given by:

$$\overrightarrow{s}''_m = |\overrightarrow{s}'| \tag{6.5}$$

The averaged absolute value of new background signals with background removed is thus given by:

$$\overrightarrow{b}''_m = \frac{1}{w}\sum_{i=1}^{w}\left[|\overrightarrow{b}_1 - \overrightarrow{b}_m| \cdots\cdots |\overrightarrow{b}_w - \overrightarrow{b}_m|\right] \tag{6.6}$$

Step 5 Calculate Signal to Noise Ratio (SNR) at every check point.

The Signal to Noise Ratio (SNR) is a measure of electrical signals that compares the level of the desired signal to the background noise. A position along the survey line with higher SNR value is considered as a possible detected target in the algorithm.

Based on the definition of SNR, the mean SNR value at a certain location, each check point column, can be determined as follows:

$$SNR = \frac{mean\left(s''^2_m(i)\right)}{mean\left(b''^2_m(i)\right)} \tag{6.7}$$

$$SNR_{dB} = 10\log_{10}\left[\frac{mean\left(s''^2_m(i)\right)}{mean\left(b''^2_m(i)\right)}\right] dB \tag{6.8}$$

SNR_{dB} is used for all SNR calculations. At this point, an original 2-D radar image is converted to a 1-D plot of SNR_{dB} versus horizontal position along the survey line.

Step 6 Perform threshold selection based on probability distribution of data obtained in Step 5.

Based on the SNR_{dB} values defined as a function of horizontal positions, a histogram can be generated showing the distribution of every SNR_{dB} value. Analysis of field data indicates that these values tend to be normally distributed, and thus a normal distribution function has been selected to fit the histogram of SNR_{dB} values. Several probability thresholds can then be selected based on estimates of the probability of target presence, which can be expressed as the possible number of targets per unit length along the survey line. According to the distribution function fitted in the histogram, the related thresholds of SNR_{dB} values can be back calculated and applied on the previous results.

At this point, a unique threshold cannot be determined. Instead, a group of thresholds are tested. Additional comparisons with the results of Algorithm 2, as described below, need to be applied to finalize an optimal threshold value.

6.5 Algorithm 2: Anomalous Signal Removal

6.5.1 Overview of Algorithm 2

GPR images are often plagued by anomalous discontinuous scan traces, as shown in Figure 6.4. Such anomalous traces could provide false high peaks in the SNR_{dB} plots mentioned above, which might generate an inaccurate detection result for the entire survey line. While causes of these anomalies vary, Liu et al. [168] assessed the stability of GPR systems, and highlighted that their performance can degrade with use and aging, and is particularly vulnerable to antenna vibration among other variables, reinforcing the importance of managing trace instabilities. In order to avoid the influence of these anomalous lines in the data processing, an additional algorithm based on signal (row by row) rate of change is developed.

Because the anomalous traces tend to cross through the entire vertical range of GPR images, changes in the GPR signal along any horizontal data row crossing the lines should show a significant change in value at all vertical positions. Based on this assumption,

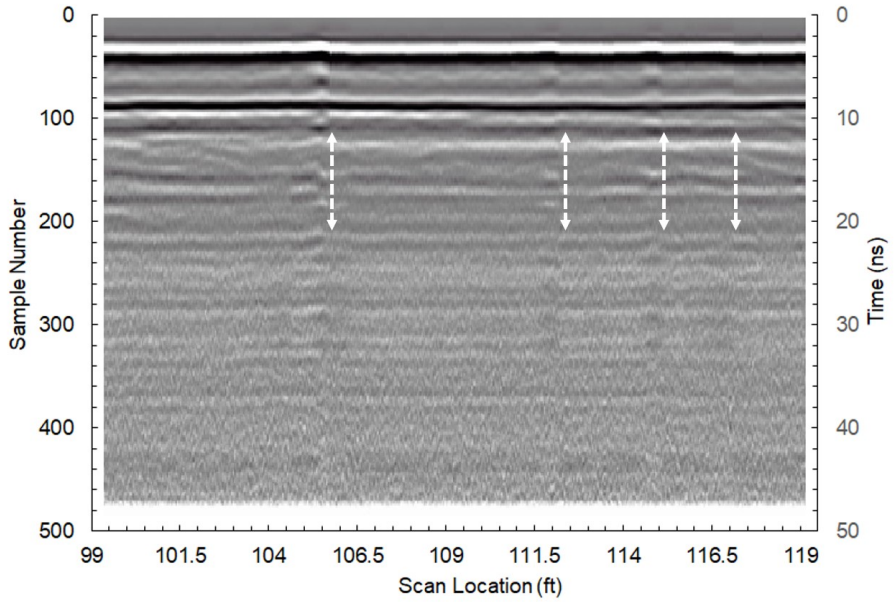

Figure 6.4.: Anomalous Scan Traces in GPR Images (white dashed double arrow lines)

the percentage change in the signal amplitude of every element relative to the previous element in every row of GPR data is calculated. This calculation is repeated row by row and column by column until the entire dataset is processed. However, even if there is a value jump across the anomalous lines; it is still not necessarily large enough to be noticed at the individual row level. Thus, a summation of the percentage changes for each row in a data column is calculated. Finally, the original 2-D GPR image is also converted into a 1-D plot of this percentage change versus horizontal position, which allows the output from this algorithm to be removed from the output of Algorithm 1.

6.5.2 Detailed Procedures of Algorithm 2

The main purpose of this algorithm is to eliminate the influence of anomalous lines in GPR images. To implement this algorithm, procedures introduced below are followed.

Step 1 Calculate the percentage change of one element relative to the previous element in each row.

As introduced previously, the original GPR image can be considered a 2-D matrix data set. In order to implement Algorithm 2, the percentage change of every element relative to its horizontal (row direction) previous element must be calculated. As shown below, the original GPR data is converted into a new matrix data set based on equation (6.9). Each element of this new matrix is the calculated percentage change value.

$$\text{Original GPR Data Matrix} \Rightarrow \begin{bmatrix} d_{11} & d_{12} & \cdots & d_{1,j-1} & d_{1,j} & \cdots & d_{1,n-1} & d_{1,n} \\ \vdots & \vdots & \vdots & \vdots & \vdots & \vdots & \vdots & \vdots \\ d_{i,1} & d_{i,2} & \cdots & d_{i,j-1} & d_{i,j} & \cdots & d_{i,n-1} & d_{i,n} \\ \vdots & \vdots & \vdots & \vdots & \vdots & \vdots & \vdots & \vdots \\ d_{m,1} & d_{m,2} & \cdots & d_{m,j-1} & d_{m,j} & \cdots & d_{m,n-1} & d_{m,n} \end{bmatrix}$$

$$\begin{aligned} p_{i,1} &= 0; \\ p_{i,j} &= \tfrac{d_{i,j}-d_{i,j-1}}{d_{i,j-1}} \times 100\%; \end{aligned} \tag{6.9}$$

$$\text{Converted Matrix of Percentage Values} \Rightarrow \begin{bmatrix} 0 & p_{12} & \cdots & p_{1,j-1} & p_{1,j} & \cdots & p_{1,n-1} & p_{1,n} \\ \vdots & \vdots & \vdots & \vdots & \vdots & \vdots & \vdots & \vdots \\ 0 & p_{i,2} & \cdots & p_{i,j-1} & p_{i,j} & \cdots & p_{i,n-1} & p_{i,n} \\ \vdots & \vdots & \vdots & \vdots & \vdots & \vdots & \vdots & \vdots \\ 0 & p_{m,2} & \cdots & p_{m,j-1} & p_{m,j} & \cdots & p_{m,n-1} & p_{m,n} \end{bmatrix}$$

Step 2 Calculate the summation of every column of the new percentage data matrix.

Although it is assumed that there will be a value jump in every row of the original GPR 2-D image when crossing the anomalous lines, the percentage value obtained per row in the last step is still not necessarily readily identified. Thus, a summation of each column of

the new converted percentage data matrix is calculated. At this point, the original 2-D GPR data is also converted into a 1-D plot comparable to that developed with the first algorithm.

$$sp_j = \sum_{i=1}^{m} p_{i,j} \tag{6.10}$$

Step 3 Calculate the standard deviation of each column of the data matrix obtained in step 1.

Based on 2-D GPR images, it is clear that a jump in signal values in a vertical row of the data matrix could result not only from anomalous lines, but also from target detection. The anomalous lines, however, normally cross through the entire vertical data set. As a result, the value jumps caused by anomalous lines always occur in all the rows at that position. Instead, the value jumps caused by possible target detection only happen in a vertical range consistent with the target position. So the standard deviation of each column of the percentage change data matrix can be employed as another useful criterion to eliminate the unwanted anomalous lines. Based on this assumption, both anomalous lines and target detection could cause a notable spike in the percentage change summation. However, the standard deviation of the columns where anomalous lines are present should be small compared with the locations of a target, as the change in the case of the anomalous line will be consistently significant over the entire vertical range.

To this end, standard deviation values of each column of the matrix in Step 1 are also plotted in the form of a 1-D figure.

$$stdp_j = \text{std}\left[p_{i,j}\right]_{i=1}^{m} \tag{6.11}$$

Step 4 Apply thresholds to both plots obtained in Step 2 and 3 based on their probability distribution functions.

This step is similar to Step 6 introduced in the first algorithm. The histograms of the results obtained in the previous two steps are generated. Then the resulting histograms are fit with a probability distribution function. Instead of selecting a normal distribution as with

the first algorithm, a gamma distribution function is selected here as most representative of the distribution of standard deviation.

Again, several probability thresholds are chosen based on the confidence sought in determining the targets along the survey line. According to the distribution function fitted to the histogram, the related thresholds of percentage values can be back calculated and applied to the previous results.

Just as for Algorithm 1, a unique threshold cannot be selected at this point. An optimal threshold will be determined in additional comparison steps.

Step 5 Combine two percentage outputs into one plot corresponding to selected thresholds.

After a group of thresholds is applied in the last step, a comparison of the percentage summation plot with the percentage standard deviation plot of each selected threshold is performed. Peaks present in both plots are left in the final result of the current algorithm. Peaks that only appear in one plot are ignored.

6.5.3 Combination of Two Proposed Algorithms

As mentioned previously, a group of thresholds are selected based on the probability distribution function of both results of the proposed algorithms. In other words, each selected threshold corresponds to two output plots for each algorithm mentioned above.

The results of the two algorithms need to be combined into a single output. Peaks present in the output of both algorithms are chosen to be shown in the combined result. Peaks only shown in one algorithm's result are ignored. Thus, each selected threshold level has a combined result for one input data set at this point.

6.5.4 Comparison of Multi-Frequency Results

GPR data collected with different frequency antennae could provide complementary information that reinforces confidence in a detection signal. For example, in the field appli-

cation of this methodology detailed below, two operating frequencies have been considered, 400MHz and 900MHz.

To compare the results obtained with different frequency antennae, the most important step is to align both results at the same horizontal starting point, to make sure the detected pipe signals appear at the correct horizontal locations. Then the plots of the final results obtained at different frequencies can be depicted in the same figure. The peaks shown in both frequency results could be considered as more likely locations of target pipes.

6.6 Field Data Analysis Based on Proposed Algorithms

6.6.1 Overview

Based on the methodology introduced previously, two field surveys are analyzed in the following sections.

The first field test was performed on a section of highway US-231 in central Indiana, in the United States, near the intersection of US-231 and INDIANA-25 involving 4 PVC outlet pipes. The average depth of the target pipes was about 0.6m-0.9m (2-3 feet), and the pipes had a diameter of 8 inches ($\sim$0.2m) (Pipe No. 1) or 4 inches ($\sim$ 0.1m) (Pipe No. 2-4). The GPR system used in this test was equipped with two antennas having frequencies 400MHz and 900MHz. The total survey traverses approximately $400m$ ($1300ft$), and the data was collected on the paved shoulder of the constructed pavement.

The data analysis procedures mentioned above were applied to this field data to check the effectiveness of the proposed algorithms. A final analysis result is presented at the end of this section.

6.6.2 US-231 Field Data Analysis

In this section, field test data is analyzed following the procedures introduced above and employing the two different proposed algorithms. As shown in figures 6.5 (900MHz) and 6.6 (400MHz), only pipe No.1 (Figure 6.5(a)) can be readily seen via visual inspection in

the original 900MHz GPR images. The other 3 smaller pipes cannot be readily visualized in the 900MHz data or the 400MHz data.

In the following sections, the field data is analyzed following the procedures introduced in the previous sections. Because the data processing procedures are the same for both 900MHz and 400MHz data prior to the final combination of different frequency outputs, only 900MHz processed results are presented in the discussion below. At the end of the discussion, the final combination of two frequency results is performed in order to make the final detection decision for this field survey test.

As described in Figure 6.3 previously, the signal at the target point and the signals at the non-target area sometimes look very similar and are difficult to differentiate based on the original GPR observations. As a result, even a target may not be visualized as a hyperbola shape in the original 2-D radar image, which is a routine indicator of target detection in GPR applications. However, the difference between these two areas can be readily determined after the background (clutter) signals have been removed using the proposed moving window background removal algorithm as discussed below.

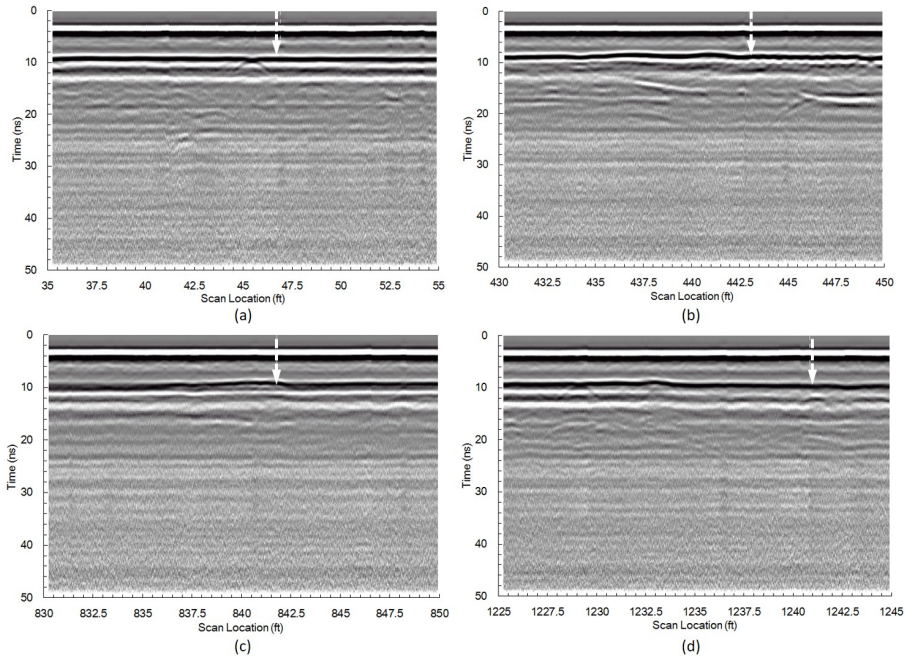

Figure 6.5.: Original GPR Data set of 900MHz Frequency

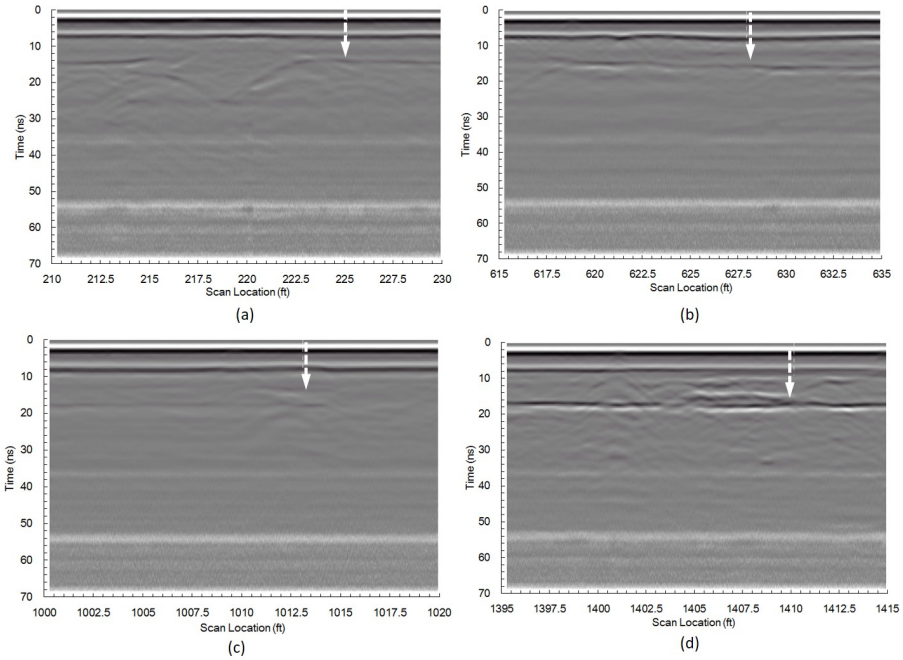

Figure 6.6.: Original GPR Data set of 400MHz Frequency

900MHz Results of Algorithm 1 Moving Background Reduction

SNR_{dB} **Values Plot** As introduced earlier, the major result provided in this algorithm is a 1-D SNR_{dB} plot versus horizontal survey position, which is shown on the right side of Figure 6.7(a). The moving window size in this data set analysis was selected as $w = 10traces$ and the checking point distance was selected $d = 5traces$.

Histogram with Distribution Fit of SNR_{dB} **Results** Based on the obtained SNR_{dB} results, a histogram figure is generated for future threshold selection, shown on the left side of Figure 6.7(a). Together with the histogram plot, a probability distribution function is also fit to the results. A normal distribution function is selected to characterize the data.

900MHz Results of Algorithm 2 Anomalous Signal Removal

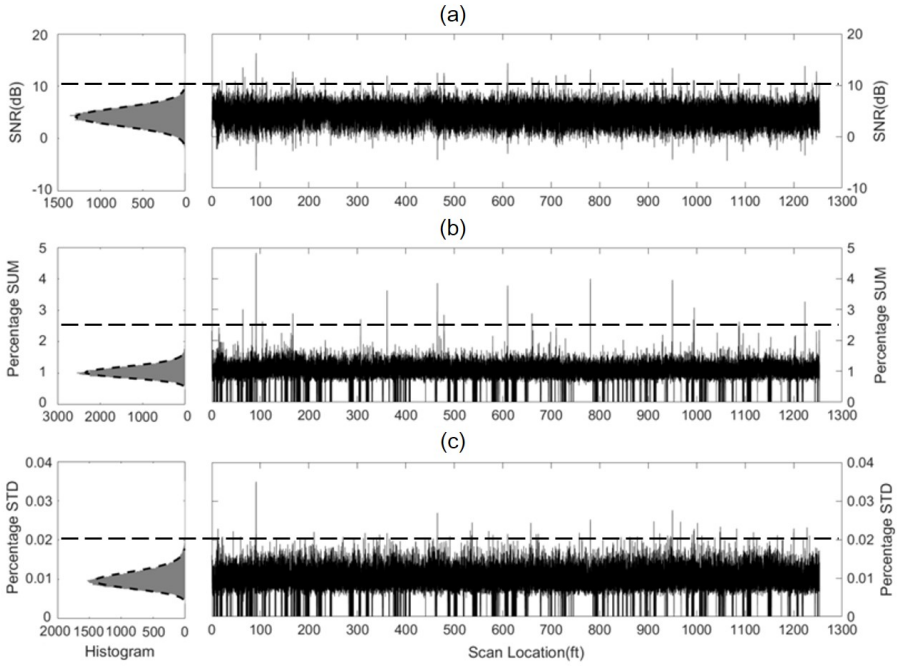

Figure 6.7.: (a) 900MHz result of algorithm 1; (b) 900MHz result of algorithm 2 – percentage summation; (c) 900MHz result of algorithm 2 – percentage standard deviation

As described above, two major output results are provided from this analysis procedure, a percentage summation plot (Figure 6.7(b)) and a percentage standard deviation plot (Figure 6.7(c)).

Similarly, histograms of both the percentage summation and standard deviation plots are generated herein, together with suitable distribution functions. Instead of selecting a normal distribution as with algorithm 1, a gamma distribution is more appropriate here.

Threshold Selection for both Algorithms As described earlier, selection of thresholds for both algorithms is based on their probability distribution functions. A group of probability thresholds is used in the whole analysis procedure. Real number thresholds for a single case can be back calculated by their corresponding probability distributions. Due to the fact that the number and dimension of pipes in the entire survey line is extremely small compared to the total survey length; a group of high probability thresholds is selected in this analysis procedure. Trial analysis is performed for all the thresholds; subsequent anal-

ysis provides an optimal threshold value. The trial group of probability thresholds is listed below.

$$T_P = [T_{P1}, T_{P2}, T_{P3}, T_{P4}, T_{P5}] = [99\%, 99.9\%, 99.99\%, 99.999\%, 99.999\%]$$

Combination of Results of Two Algorithms with Thresholds applied In this section, each threshold in the list above is first applied to all the results obtained in Figures 6.7(a), 6.7(b) and 6.7(c) separately. Then the results of both algorithms are combined into one data set retaining only peaks present in both plots. Finally, a pipe interval searching procedure is applied, effectively helping to further enhance detection likelihood by recognizing typical design spacing ranges for sub-pavement drains. The final results of the 900MHz survey correlated to every tested threshold level are then generated. Figure 6.8 shows the results of 900MHz data with probability thresholds T_{P1} to T_{P5}.

Based on prior information of known pipe locations (the four dotted vertical lines in the plots), the figures illustrate that the threshold levels of T_{P1} and T_{P2} provide results with large numbers of false alarms along the detection line. On the other hand, the threshold levels of T_{P4} and T_{P5} provide results that are likely over-selective, and thus fail to detect most major targets. Thus, the threshold level of $T_{P3} = 99.99\%$ is considered as the optimal threshold level that should be applied in this analysis procedure, with those potential target locations not known prior to the analysis serving as sites that should be investigated manually in the field.

Combination of Results Obtained by Two Frequencies In order to obtain a more accurate detection result, the comparison between results of two different frequencies is pursued. With the optimal threshold level of $T_{P3} = 99.99\%$, a final detection result is presented in Figure 6.9. As shown in this figure, 4 dotted vertical lines indicate the actual known pipe positions along the highway survey line; peaks in Figure 6.9(a) are the possible pipe detection locations from the 900MHz result; and peaks in Figure 6.9(b) are the possible pipe detection locations from the 400MHz result. Considering this final result, 3

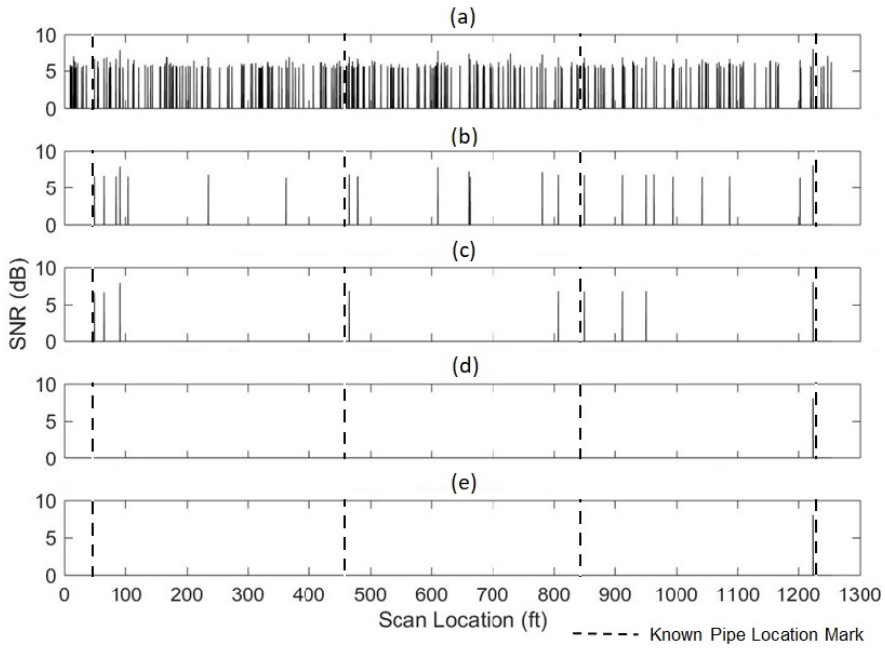

Figure 6.8.: 900MHz Final Result at Threshold Level of $(a)T_{P1} = 99\%; (b)T_{P2} = 99.9\%; (c)T_{P3} = 99.99\%; (d)T_{P4} = 99.999\% and (e)T_{P5} = 99.9999\%$

pipes could be detected by the proposed analysis procedures, but there are a few additional alarms presented, which could be previously unknown pipes or false alarms.

6.6.3 Target Detection Coding

To facilitate interpretation of the final results obtained using the introduced algorithms, a detection code was defined to categorize the points of interest highlighted through the analysis. There are several parameters that affect final detection decisions. First of all, the SNR indicators shown in figure 6.9 serve as the primary results obtained by the introduced algorithms. The location of such indicators are considered "points of interest" that can be compared to the original field GPR images to make further decisions. Second, as there are typically three possible situations that could cause the "points of interest" in the final results shown in Figure 6.9, 1) the point of interest is associated with a hyperbola signal that is normally considered as a scattered reflection from underground objects, 2) the point

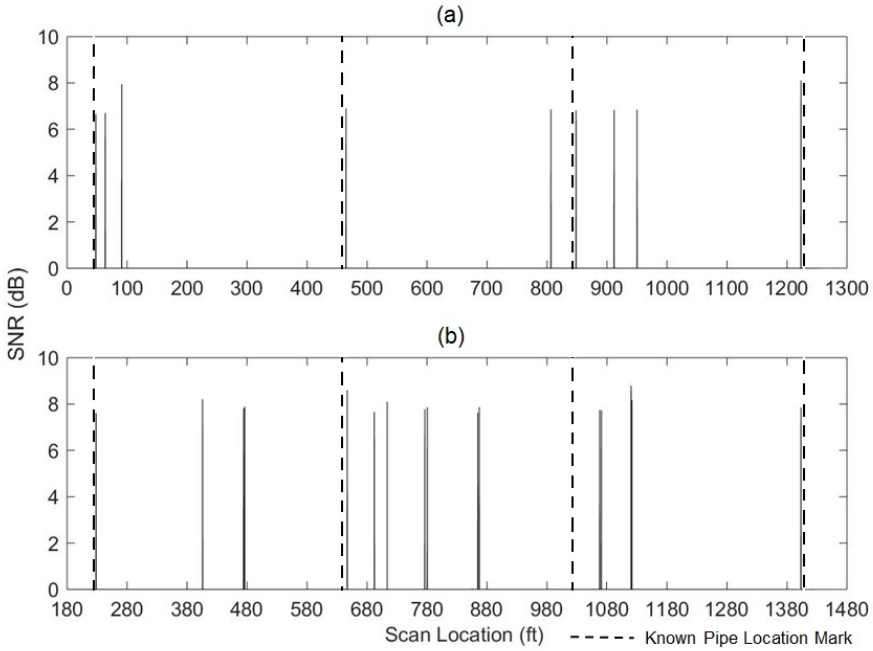

Figure 6.9.: Final detection result of $US-231$ field test with a Threshold level of $T_{P3} = 99.99\%$, (a) 900MHz, (b) 400MHz

of interest is an anomaly which is always considered noise and 3) the point of interest occurs where there is no obviously identified 2D signal. Finally, in addition to the above parameters, there is often some prior information on known target locations, like those analyzed in previous sections.

Based on all the above parameters, a target detection code was introduced to help evaluate the detection effectiveness of the introduced algorithms. As described in table 6.1, there are five different code numbers to indicate the above outlined detection situations. A) the code "-2" represents the situation of a missed detection of a known target, which means that at a pre-known target location, there were neither 1D signals obtained by the introduced algorithms nor 2D original GPR hyperbola signals; B) the code "-1" represents the situation of a false alarm, which means that at the specific point of interest derived from the 1D signals obtained by the algorithms there is a clear anomaly in the original 2D GPR images; C) the code "0" represents the situation of an undetermined target location or

Table 6.1.: Detection Code Parameters and Rating Key

Detection Code	Hyperbola Reflections Observed in 2D Original GPR Image	Anomalous Signals Observed in 2D Original GPR Image	1D Signals Observed in Final Results of Algorithms Output	Positions of Pre-Known Targets	Remark
-2	N	N	N	Y	Miss Detection
-1	N	Y	Y	N	False Alarm
0	N	N	Y	N	Possible Target Position
1	N	N	Y	Y	Target Detected
2	Y	N	Y	N	Target Detected
3	Y	N	Y	Y	Target Detected

possible target detection, that requires further investigation and, that at the specific location of the 1D point of interest, there were neither hyperbola reflection signals nor anomalous signals in the 2D images. At this location, it is highly possible that there is an unknown target in the sub-pavement and the original GPR signal was hidden in the background signals; D) the code "1" represents a detected target (case 1), which means that at the specific location of the 1D point of interest obtained by the algorithms, there were neither hyperbola reflection signals nor anomalous signals, however, these locations were the locations of pre-known targets; E) the code "2" represents a detected target (case 2), which means that at the specific locations of the 1D point on interest signal obtained by the algorithms, hyperbola reflection signals can be clearly observed but no prior target location information was available; and, F) the code "3" represents a detected target (case 3), which means that at the specific location of the 1D point of interest signals obtained by the algorithms, hyperbola reflection signals can be clearly observed and these locations were pre-known target locations.

Figure 6.10 presents the final results of the US-231 analysis from Figure 6.9, in the form of the above outlined detection codes for each of the identified points of interest. It is shown that all 4 pre-known PVC pipes were detected in the 900MHz results obtained via the introduced algorithms, although only one could be recognized in the original GPR images. Further, only one known pipe was missed in the 400MHz results based on this approach, even though all were missed in the original 400MHz GPR images. Collectively, three known pipes were successfully detected by the algorithms. In addition to the successful

target detection at the known pipe locations, there were also some of false alarms (detection code -1) captured and other possible targets (detection code 0 and 2) discovered as well.

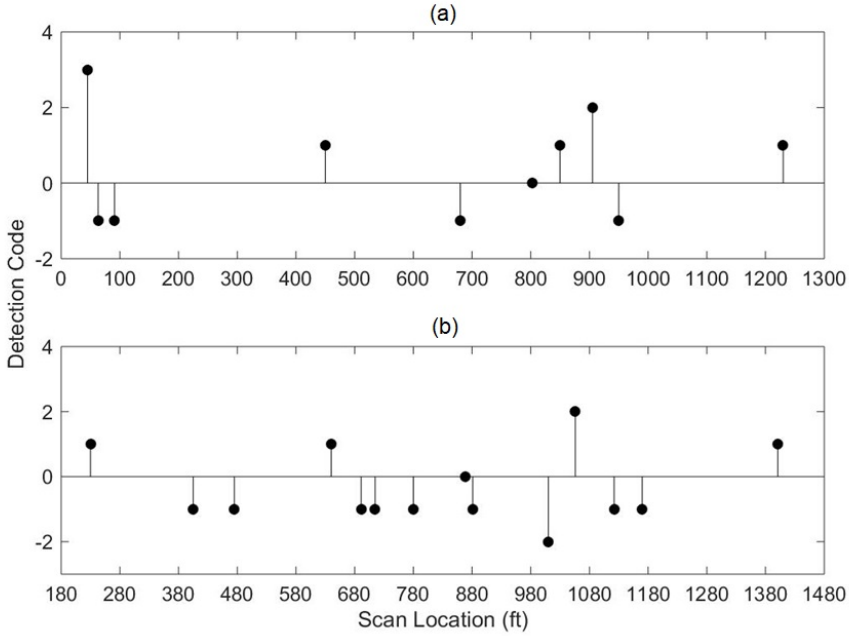

Figure 6.10.: Detection code plot based on the results obtained in Figure 6.9 (a) detection code of 900MHz results (b)detection code of 400MHz results

6.6.4 Target Detection Effectiveness

Target detection effectiveness for the introduced algorithm relative to visual inspection of the original GPR images (i.e., “observation”) for the US 231 data can be described in terms of detection successes (detection code 1 and 3), missed targets (detection code -2), inferred targets (detection code 0 and 2), and false alarms (detection code -1). Figure 6.11 provides a histogram of the detection codes for the 900MHz and 400MHz results and illustrates that system effectiveness varies based on antenna operating frequency. Use of the developed algorithm on the combined frequency data improved detection substantially over both visual observation and individual antenna analyses. Although false alarms still occur when using the algorithm, it is important to note that even when visually interpreting

the original GPR images, there are typically false alarms, and given the consequences of a missed drain, it is still better to have some false alarms than to miss a pipe.

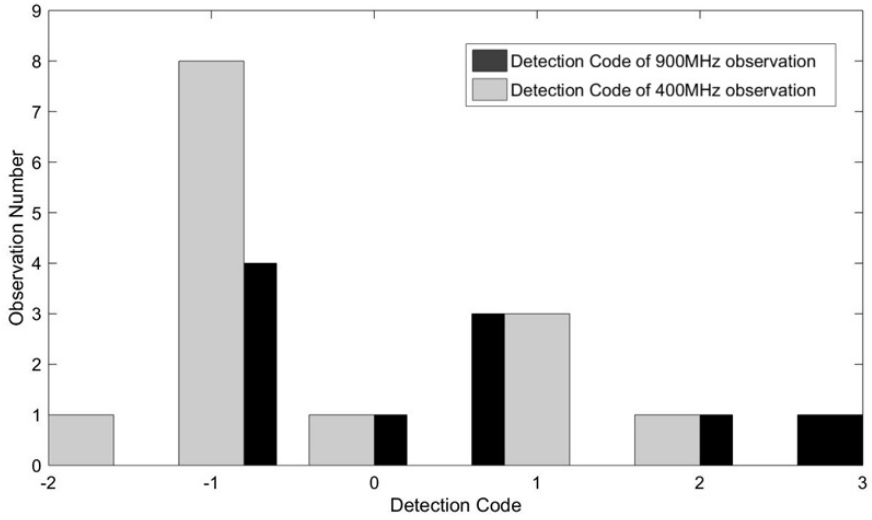

Figure 6.11.: US-231 Field Data Detection Effectiveness

6.6.5 I-65 Large Field Data Set Analysis

In addition to the field data analyzed above, another 8 km (5-miles/25000ft) field data set was also analyzed using the proposed algorithms in order to test the effectiveness of this method. The field data was obtained between mile markers 142 and 147 on Interstate-Highway-65-North (I-65N) in the U.S. state of Indiana. Tests were performed at 400MHz. The detection codes obtained along the survey line are plotted in figure 6.12. The detection effectiveness can be interpreted by examining figure 6.13 which presents a histogram of detection codes (similar to figure 6.11) for all "points of interest" obtained by the introduced algorithms.

Along this survey line, there were 26 known PVC pipes under the pavement (referred to as X-drains by the local department of transportation), which can be detected in both the original GPR images and the results generated by the algorithms presented herein.

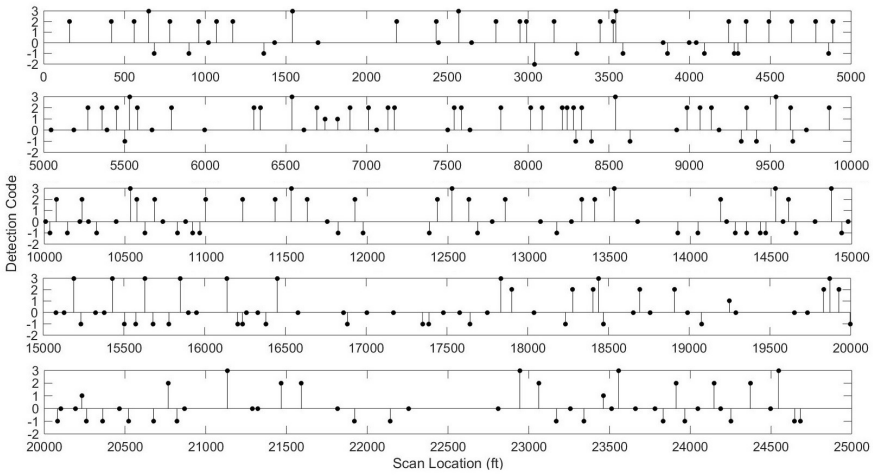

Figure 6.12.: I-65N detection code results (400MHz) between 142-mile and 147-mile

As introduced in section 6.6.3, all of these detected X-Drains were given the detection code 3 to indicate the confidence of target detection. Besides the known X-drains, there were several known old buried pipes (K-Drains) and one large transverse pipe along this survey line, the total number of these drains was 7. Among these pipes, only one K-Drain was identified in the original GPR images (at location 21,132ft (code 3) in figure 6.12), the other 6 pipes could not be identified in the original GPR images. However, based on the results obtained by the introduced algorithms, 5 of the otherwise missed known pipes were successfully detected in the final results (detection code 1 plotted in figure 6.12 at locations 6,741ft (K-Drain), 6,821ft (Large transverse pipe), 19,249ft (missed detected pipe), 20,232ft (K-Drain) and 23,462ft (K-Drain)). Only one known K-Drain could not be detected in both the GPR images and the results obtained by the algorithms (detection code -2 at location 3,040ft).

Figure 6.13 presents the histogram of all detection codes at all "points of interest". Based on the prior known information, it is clearly shown that most of the K-Drains and other known pipes can be identified successfully in the results generated by the introduced algorithms, many of which cannot be detected in the original GPR images. Meanwhile, there are 93 points of interest in the final results from the introduced algorithms that can be

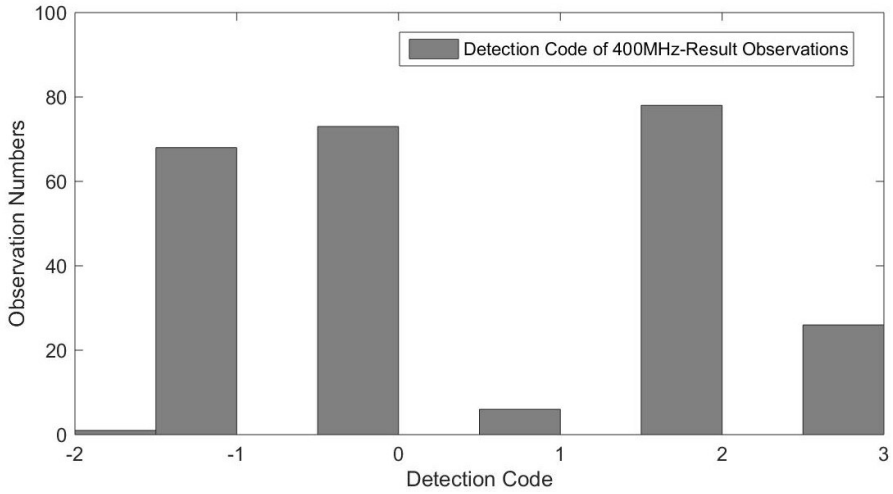

Figure 6.13.: I-65N detection effectiveness results (400MHz) between mile marker 142 and 147

matched with the hyperbola signals in the original GPR images, which can be interpreted to be detection code 2. Other points of interest in the final results of the algorithms were interpreted to be detection code 0, meaning that there were neither significant hyperbola signals nor obvious anomalous noise signals in the original GPR images; these points require further field inspection. Finally, the detection code -1 represents false alarms indicative of clear anomalies observed in the original GPR images, which can be eliminated from consideration by simple visual inspection of the data and thus do not require costly in-field evaluation. The definition of detection introduced in section 6.6.3 provides a straightforward way to convey the confidence of target detection which could help an on-site surveyor plan focused site inspection to help improve the efficiency of locating sub-pavement drains.

6.7 Summary

This chapter introduced a novel background and clutter reduction method to enhance buried pipe detection signals in constructed environments. Generally, there are two major algorithms included. Algorithm 1 is focused on reducing the effects of background noise and clutter. Algorithm 2 is focused on eliminating anomalous signals received by the GPR

equipment itself. The results obtained through the above 2 algorithms are combined together in order to get an optimal output for any given GPR operating frequency. Results can be further validated through multi-frequency analysis in which the results of different frequencies can be compared.

Compared with the original 2-D GPR images, the results obtained in this analysis significantly improved sub-pavement drain detection. The results show significant improvements in both the US-231 survey and long survey data of I-65N. In the original US-231 field data, only the largest PVC pipe (8") could be identified based on the 2-D GPR image out of a total of 4 pipes. By contrast, in the final result obtained by the proposed algorithms, the number of detected pipes increased to 3 out of 4 in 400MHz result and 4 out of 4 in 900MHz result. In addition, the algorithms successfully located 5 out the 6 previously missed known pipes along the 5-mile I-65N survey.

Overall, the proposed algorithms have the potential to enhance the effectiveness and efficiency of search operations conducted to locate sub-pavement drains along great lengths of highway. Although the false alarm rate remains high with the presented algorithms, the very low missed target rate is highly valuable to departments of transportation that wish to offset the risks associated with unmaintained sub-pavement drains, and isolation of select points of interest minimize the expense and safety concerns associated with exposure of their personnel to manual search activities. Further, the output of this method yields an easy to interpret 1-D plot along the survey line which clearly represents the horizontal positions of drains, increasing the ease and efficiency of field search activities where needed.

7. PATTERN RECOGNITION METHOD TO LOCATE UNDERGROUND PIPES

7.1 Introduction

Pattern recognition is another approach that can be employed to analyze data obtained via GPR scans. As is well known, the typical GPR signal returned by a buried drainage pipe takes the form of a hyperbola. With this in mind, the signal processing method pursued in this part of the work is focused on enhancing the collected hyperbola signals in order to identify potential targets.

In contrast to the improved background reduction method introduced in the previous sections, this analysis is still performed on the 2D data set rather than a 1D variant. The primary purpose of this method is to recognize the signature pattern – a hyperbolic shape – of potential drainage targets in order to facilitate detection. After processing data via Methods 1 (improved background reduction) and 2 (anomalous signal removal), several potential target areas are flagged. These areas can then be explored by employing a pattern recognition algorithm, hereafter referred to as Method 2 (pattern recognition), to search for hyperbolic shapes in the original GPR image. Verified by this pattern recognition technique, the results obtained by Method 1 could be more accurate and reliable.

To gain benefit from a pattern recognition method, unclear hyperbolic shapes in the original GPR image must be enhanced so that they can be recognized by an edge detection or shape recognition algorithm. Typically, there are three steps to this process: 1) The mean value of the entire potential checking area is removed in order to reduce unwanted background and noise; 2) the signal difference is improved by calculating the square of observed values; and 3) the original image is converted into a binary image by applying selected grey scale thresholds. The details of this technique will be introduced in the following sections.

7.2 Related Background

Pattern recognition is a popular image processing approach to identify particular shapes in a given image. This method can be used to detect various curves and shapes appearing in an image, such as straight lines, circles, and triangles, or in the case of GPR, the hyperbolic return resulting from a buried pipe. Confirmation of a hyperbolic return signal is a high confidence indication of a successfully detected target.

Several researchers have done a lot of work in GPR image pattern analyses. Al-Nuaimy, et al. [169] introduced an automatic detection method for buried objects using neural networks and pattern recognition; Delbo, et al. [170] introduced a fuzzy shell clustering approach to recognize the hyperbolic signatures in GPR images; Pasolli,et al. [78] introduced a pattern recognition approach to automatically analyze the GPR images. The core of these methods involve scomparison of the hamming distance between candidate hyperbolic shapes and data points in an enhanced binary GPR image.Others have expanded on this basic approach. For example, Milisavljevi, et al. [171] introduced a hyperbola detection technique using a randomized Hough transformapplied to high potential region selections. Ehret [172] introduced an artificial neural networks (ANN)- andsupport vector machines (SVM)-based pattern recognition approach to analyze geophysical data.

In this chapter, emphasis is placed on preparing a data set for application of a pattern recognition algorithm. This involves two key stages of analysis: 1) Select potential target areas using the method of improved background reduction discussed earlier; 2) Within the selected potential target areas, enable improved hyperbola recognition by improving the contrast and definition of the original image.

7.3 Data Analysis Procedures

As introduced above, the main method discussed herein is focused on enabling hyperbolic shape recognition in the original GPR images. Before applying the pattern enhancement method to the entire set of data, potential areas with targets are selected using the method of improved background reduction (Method 1). Because most of the data obtained

from a roadway scan does not contain a drainage pipe, there is little value in searching the entire data set to identify hyperbolas. Method 1 will produce a plot indicating potential drainage pipe positions as a function of horizontal location in the data set. The detailed procedures of this method have been discussed in Section 6 of this report and will not be repeated here.

Based on every marked potential pipe location, a range of data to the left and to the right is selected as the analysis area for the pattern enhancement method (Method 2). This method involves the following steps.

1. Step 1: Pre-selection of vertical data

   Just as outlined for Method 1, along the vertical depth of an A-scan, it is unlikely that data received at delay times greater than 30ns is of any value, as noise is typically stronger than the transmitted radar pulse in this range. Thus, to accelerate calculations, only the data received before 30ns is considered in the analysis (this cutoff can be modified as needed for specific field circumstances).

2. Step 2: Remove the average signal from the entire selected analysis area

   In order to enhance the received hyperbola signals and also remove some of the unwanted background and noise, such as horizontal pavement layer reflections and random noise, a simple background reduction technique is applied here. Normally, this procedure will not destroy the hyperbola signatures and may increase the contrast of the useful signals.

3. Step 3: Enhance the signal contrast by taking the square of the result obtained in step 2.

   Normally, the hyperbolic shapes in the original data set are not clear enough to be identified easily. One possible reason could be the magnitude difference between the hyperbolic signal and background is too low. Thus the contrast in the image may not be large enough to facilitate separation and the result is an unclear hyperbolic shape. Squaring the signal values in the background reduced matrix improve the contrast significantly.

4. Step 4: Convert the image matrix obtained in step 3 to a binary image based on selected threshold

   Even though step 3 could significantly increase the signal contrast in the GPR image, the signature shape of a hyperbola may not be easily identified. Thus, in order to perform automatic detection, the image obtained in step 3 is converted into a binary image based on user selected signal thresholds.

7.4 Field Data (I-65N) Analysis and Comparison

7.4.1 Introduction of Field Test on I-65N

A two day field data collection effort was performed in May 2012 on the side of Interstate road I-65N. The purpose of this test was to locate both X-Drains and K-drains on the side of the interstate. X-drains are newly installed PVC pipes under the pavement layer, while K-drains are old existing metal pipes located more deeply under the pavement. Figure 7.1 provides a picture of the equipment setup before the test. As seen in this picture, there are 4 antennae involved in this test, two 400MHz antennae and two 900MHz antennae with different polarization directions.

The data collected in this test represents a survey that is about 5 miles long, thus only a portion of the data analysis is presented here, that is the first 1000ft starting from I-65N mile marker 146.Physical observations confirm that there is at least one X-drain present at the horizontal location of 558ft and a K-drain present at the horizontal location of 910ft.

7.4.2 Data Analysis

In order to assess the effectiveness of the previously described pattern enhancement technique, only 400MHz data is analyzed here.

1) Results obtained by Method 1

As introduced in the previous sections, Method 1 was fist carried out on the data to obtain potential pipe location areas. The detailed analysis procedure was introduced in

previous sections of this report and will not be repeated here. The results from Method 1 are summarized in in Figure 7.2 and Figure 7.3.

Figure 7.1.: GPR Equipment set up on the side of I-65N

Based on the obtained results, the total number of potential targets could be 9 when applying an SNR threshold of 95%. When the threshold is set higher, the number of potential targets decreases because of the strict selection factors. Within the 9 potential targets, number 5 is the known X-drain located at about 558ft, and number 9 is the known K-drain located at about 910ft. The other 7 potential targets still could not be definitively declared detects or false alarms at this point in the analysis.

2) Hyperbola Signature Recognition in the potential regions

After obtaining the potential target regions, the hyperbola signature enhancement method was performed following the procedures introduced above. The hyperbola recognition results shown in Figures 7.4 – 7.12. There are 4 subplots in each result figure for each potential target zone. On the top left is the original received GPR image over the check range; on the top right is the simple background reduction enhanced GPR image; on the

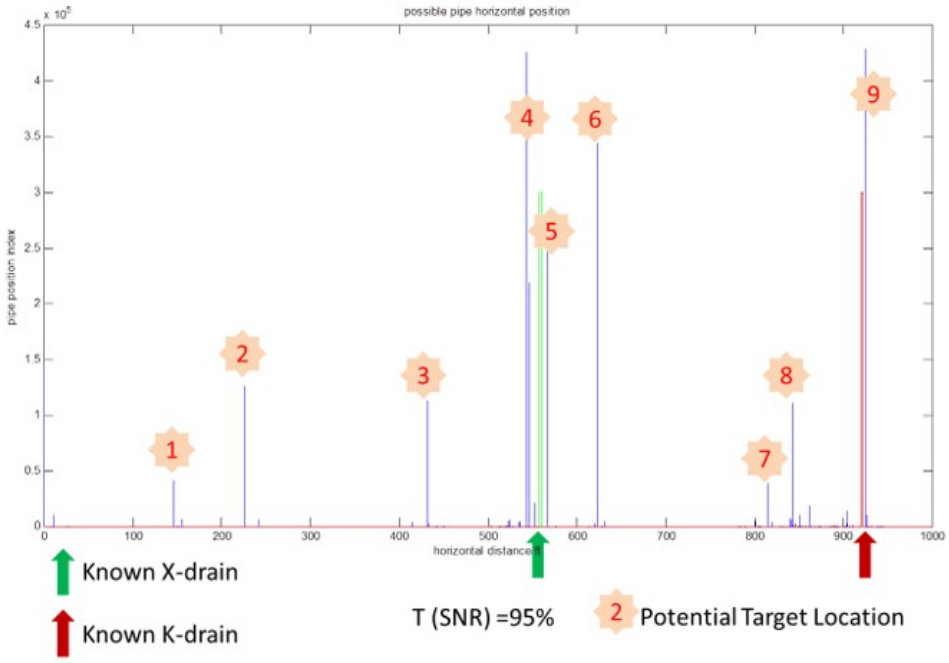

Figure 7.2.: Potential Target locations (9 in total) obtained by Method 1 with SNR threshold T=95%

bottom left is the squared value image based on background removed GPR image; on the bottom right is the converted binary image used to recognize hyperbola signatures. (Note that the check range here is narrower than the 30 ft used in the field simply to facilitate presentation and make the hyperbolic returns more easily visible in the figures).

Based on the results described above, targets 4, 5 and 7 can be defined as detection zones. Even though no drain was pre-identified at locations 4 and 7, they are clearly worth close inspection as both employed signal processing algorithms indicate the presence of a buried conduit.The remaining targets would require further investigation. It is important to note that the absence of a hyperbolic return cannot be used as a means to define a false alarm, as results presented earlier for the background reduction algorithm confirm that the statistical approach can identify drains even when no hyperbolic return is evident. Thus the shape enhancement and related shape recognition activities serve mainly as a means to enhance certainty associated with detection zones.

3) K-Drain detection based on selected layer analysis using Method 1

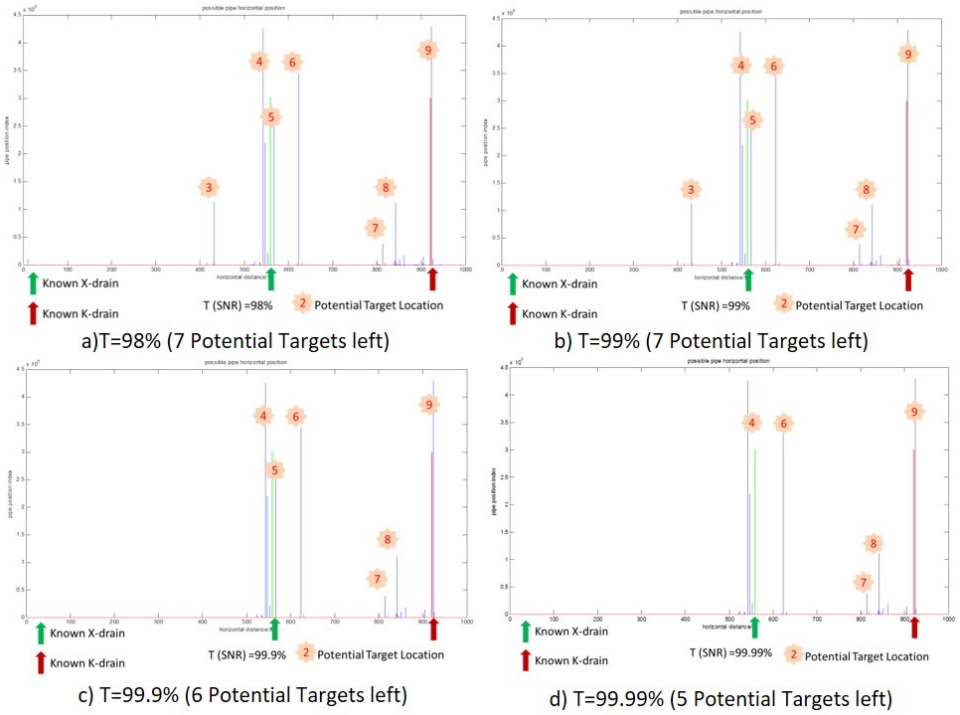

Figure 7.3.: Potential Target locations from by Method 1 as a function of SNR threshold

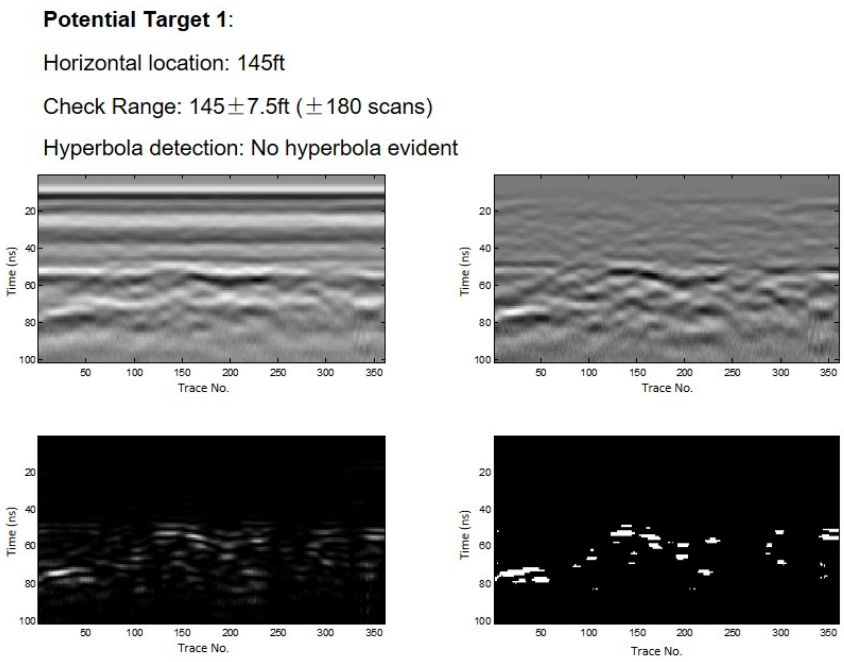

Figure 7.4.: Potential Target 1

Potential Target 2:

Horizontal location: 230ft

Check Range: 230±7.5ft (±180 scans)

Hyperbola detection: No hyperbola evident

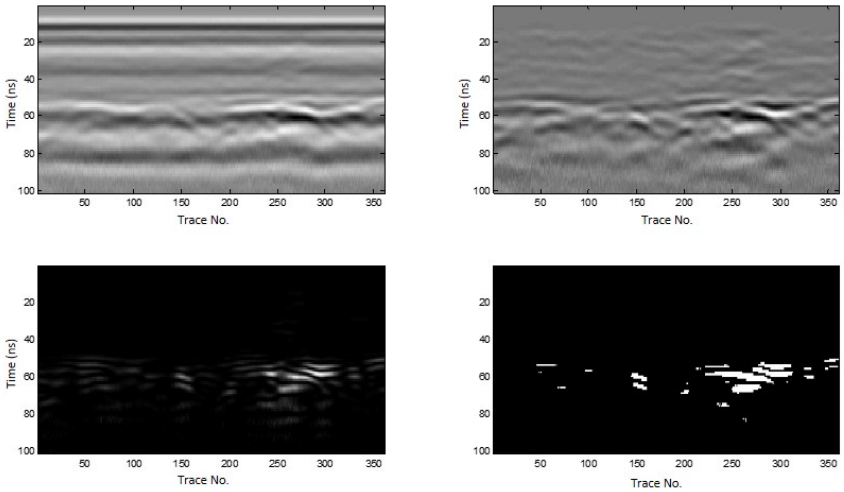

Figure 7.5.: Potential Target 2

Potential Target 3:

Horizontal location: 410ft

Check Range: 410±7.5ft (±180 scans)

Hyperbola detection: No hyperbola evident

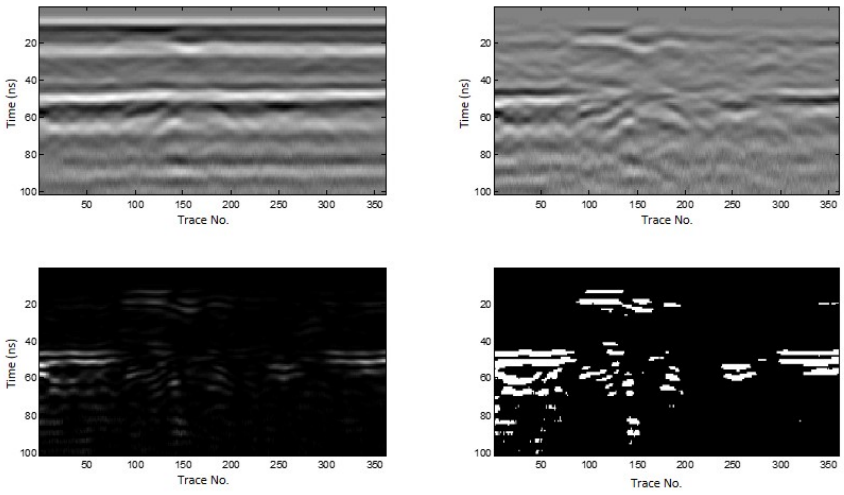

Figure 7.6.: Potential Target 3

Potential Target 4:

Horizontal location: 522ft

Check Range: 522±7.5ft (±180 scans)

Hyperbola detection: Hyperbola evident (Very Clear)

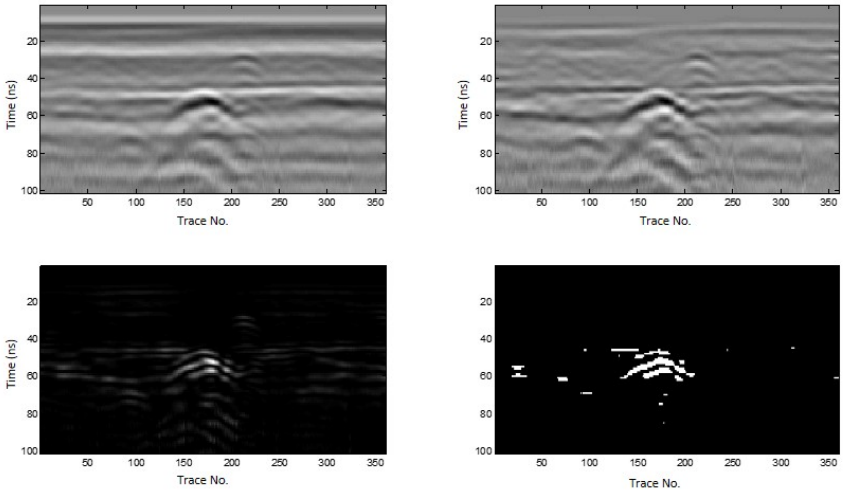

Figure 7.7.: Potential Target 4

Potential Target 5 (Known X-drain):

Horizontal location: 557ft

Check Range: 557±7.5ft (±180 scans)

Hyperbola detection: Hyperbola evident (Very Clear)

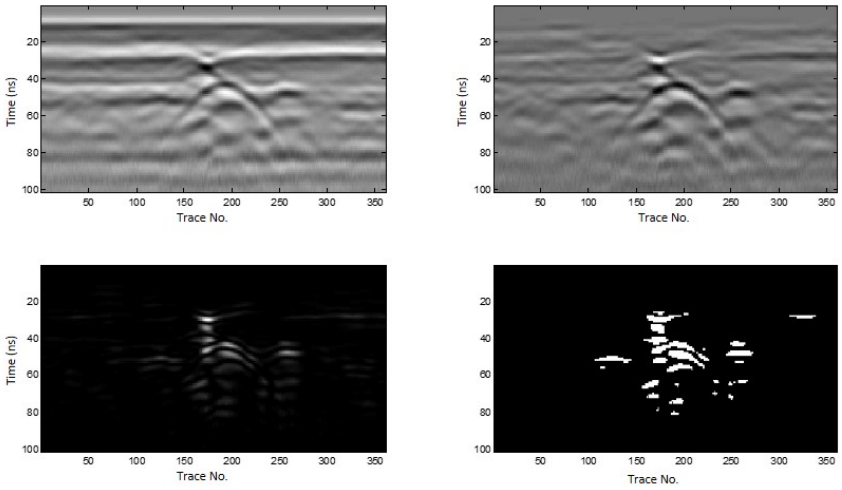

Figure 7.8.: Potential Target 5

Potential Target 6:

Horizontal location: 620ft

Check Range: 620±7.5ft (±180 scans)

Hyperbola detection: No hyperbola evident

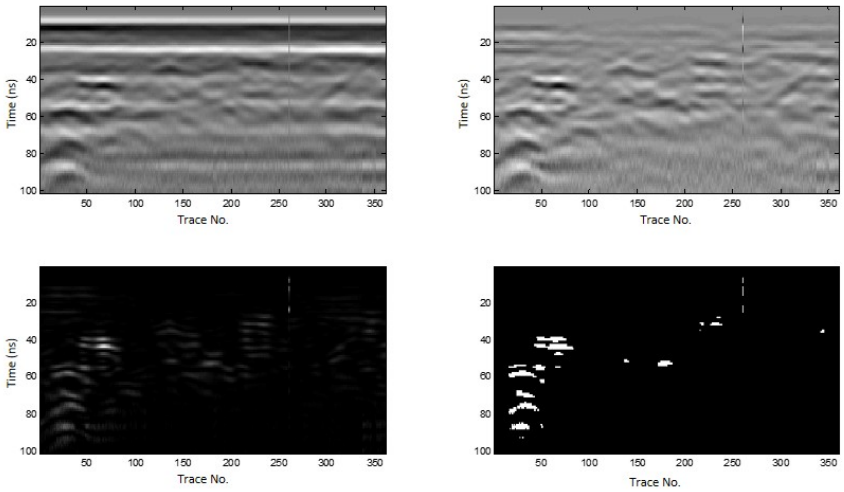

Figure 7.9.: Potential Target 6

Potential Target 7:

Horizontal location: 820ft

Check Range: 820±7.5ft (±180 scans)

Hyperbola detection: Hyperbola evident (Clear)

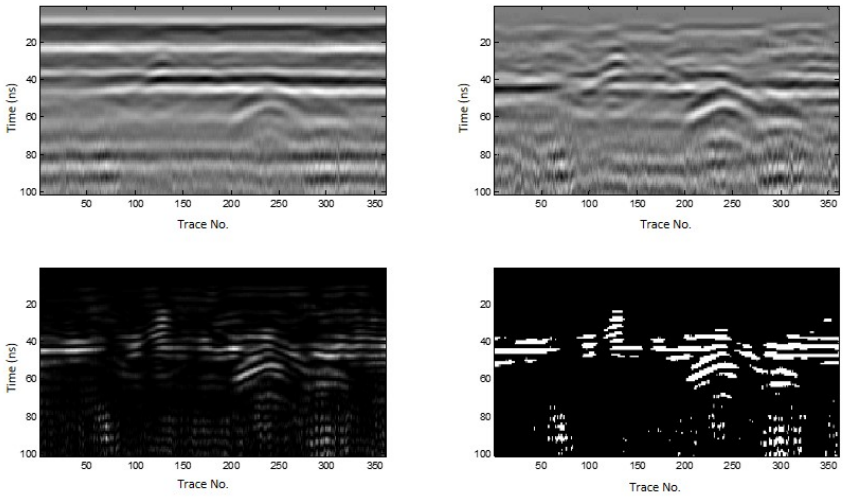

Figure 7.10.: Potential Target 7

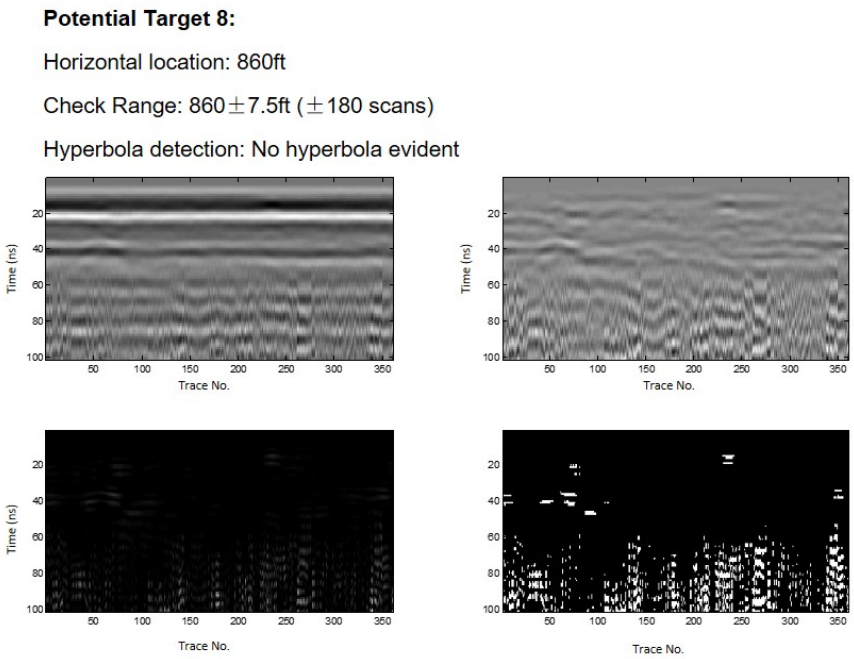

Figure 7.11.: Potential Target 8

The I-65N field test was unique in that the study area contained 3 known K-drains (as well as a large transit pipe). K-drains are metal pipes or clay conduits associated with old pavement systems and are typically buried beneath modern, renovated pavement layers. When roads are reconstructed, the K-drains are often left in place. Over time, if not maintained, K-drains can retain soil, vegetation, and water, which in turn leads to serious pavement damage. Unfortunately, these drains are very difficult to locate as they are often associated with poorly documented construction operations from many years ago and can be hidden by vegetation as shown in Figure 7.13. With this in mind, effort herein was also made to locate K-drains in the I-65N data set. In total approximately 2 miles of data was analyzed, from I-65N mile marker 143 to 144, and from mile marker 146-147.

In order to locate K-drains using the analysis algorithms described earlier, a vertical region of the GPR image data is isolated that is likely to contain the K-drains. Based on the discussion above, K-drains were normally buried under new pavement system layers. Consequently, the only area in the original image that should be considered is the area

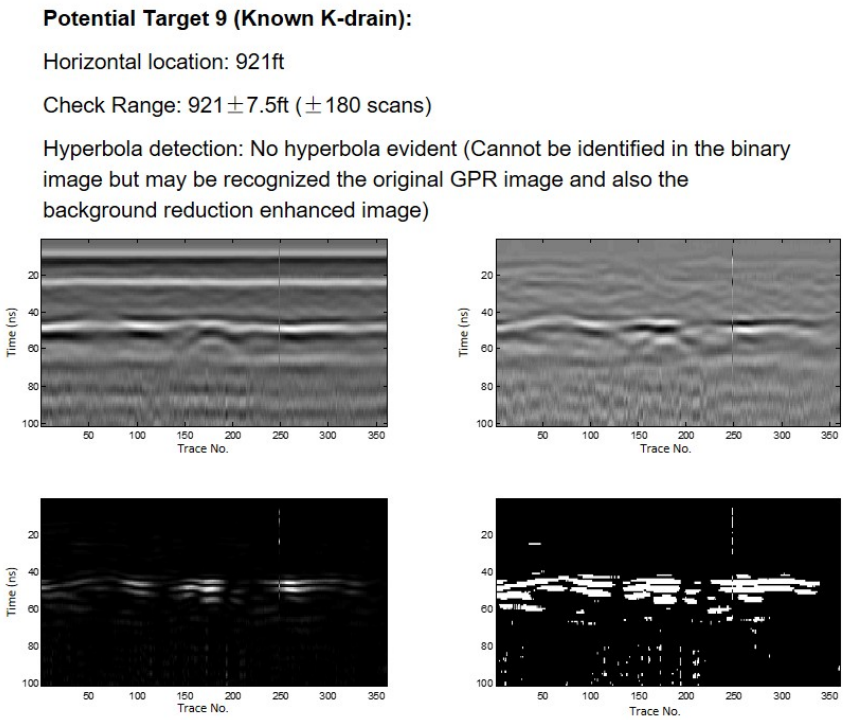

Figure 7.12.: Potential Target 9

Figure 7.13.: Buried K-Drains on the side slope of I-65N

deeper than all the pavement layers, including the X-drain layer, which is normally located in the base layer of pavement.

With this in mind, the signal processing method is then applied to a vertical range of the GPR data from the 2-mile I-65N field exercise that extends from 1 – 2 meters below

the ground surface. Following the same analysis procedures introduced above for Method 1, the final output of possible K-drain locations is shown in Figures 7.14 and 7.15.

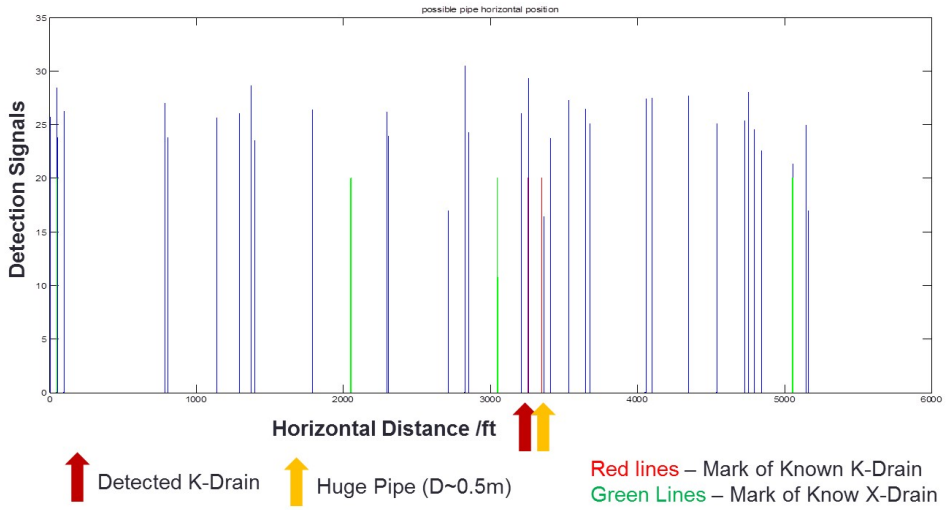

Figure 7.14.: Possible K-drain locations determined by Method 1 (I65N 143-144mi)

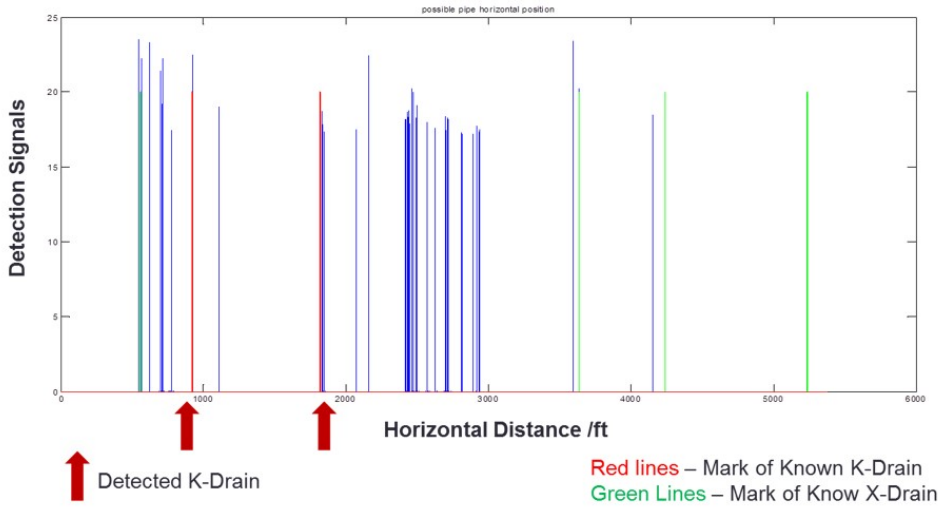

Figure 7.15.: Possible K-drain locations determined by Method 1 (I65N 146-147mi)

The locations of the known K-drains in the Figures 7.14 and 7.15 are marked by red arrows and red lines. The green lines in the figures indicate locations of known X-drains. The blue lines represent possible target locations resulting from the data analysis. As shown, all 3 known K-drains were successfully detected by the employed algorithm. However, there

are also a significant number of “potential” false alarms. These are described as “potential” false alarms because no field work has been completed to check if there actually is a K-drain at the additional locations identified. Also, it is important to note that conduit spacing rules cannot be applied here as there is no evidence that older construction operations employed uniform spacing for the drains. Thus, some of the inferred targets may indeed be buried conduits, and others, of course, may truly be false alarms. Nonetheless, the fact that all known K-drains were detected is encouraging. Future work should likely be focused on gathering additional validation information, and on reducing false alarms in the K-drain analysis.

8. EFFECTS OF GPR ANTENNA CONFIGURATION ON SUBPAVEMENT DRAIN DETECTION BASED ON THE FREQUENCY-SHIFT PHENOMENON

8.1 Introduction[1]

As discussed earlier, the success of GPR detection is highly dependent upon underground media conditions, such as the type and water content of the subpavement soils as well as the selected configuration of the GPR antennas. Antenna configuration is also known as antenna diversity [173], and includes such parameters as polarization diversity (antenna orientation and angles), spatial diversity (antenna offset), and transmit/receive diversity (antenna set-up mode and adaptive arrays). Thus, in GPR practice, the antenna configuration represents an important variable that can significantly influence final detection results.

Numerous researchers have studied the polarization diversity of antennas. For example, Roberts and Daniels [174] presented a detailed theoretical study of GPR polarization phenomena with regard to both planar interfaces and cylindrical targets. In order to understand the polarization effects of cylindrical objects, Radzevicius and Daniels [175] simulated and conducted experimental survey work using linearly co-pole and cross-pole antennas, which led to their conclusion that the scattering properties of cylinders (such as pipes) were strongly dependent on polarization. Also, Radzevicius and Daniels [175] observed maximum amplitudes when crossed dipoles were oriented at 45°to the pipe. Porsani et al. [176] performed an on-site full-scale experiment to compare the detection results of both steel and concrete targets. Their tests were based on perpendicular and parallel configurations whereby the co-pole antennas are 90°or 0°to the longest axis of the target. The Porsani et

[1]This chapter is mainly based on the published peer reviewed journal paper "Effects of GPR antenna configuration on subpavement drain detection based on the frequency-shift phenomenon" [45]

al. [176] results showed that the steel pipe targets were highly dependent upon the antenna polarization configurations and returned much stronger signals during perpendicular testing. By contrast, efforts to detect concrete tubes yielded better resolution images during parallel testing than in perpendicular testing. Other previous work includes studies of, for example, antenna polarization performance based on different angles between the transmitter and receiver (referred to above where 0°is the co-pole set-up and 90°is the cross-pole set-up) [177, 178]; improved migration techniques and algorithms based on multi-antenna configuration of GPR detection [179, 180]; and multi-antenna configuration GPR measurements for geostructure (fracture) characterization [181], and mine detection [182].

The separation between the transmitter and receiver, known as antenna offset or spatial diversity, is considered to be another main antenna configuration factor. Gurel and Oguz [183] and Bai and Sinfield [142] conducted studies to determine the optimal separation distance between transmitters and receivers based on simulations. It was observed that after a particular separation of the antennas, which was considered as the optimum value, the received energy of the antennas started to drop significantly. It was also observed that different GPR detection modes had different optimal antenna separation distances. Multi-offset approaches to GPR, involving observations at multiple variations of transmitter – receiver separation, have also been applied in migration/tomography studies to analyze key wave properties in the subsurface, such as travel velocity using multi-fold acquisition [184].

The combination of transmitters and receivers (or transmit/receive diversity) represents another fundamental set-up consideration that can be varied to enhance multi-antenna configuration GPR surveys for different GPR applications. In addition to paired transmitter and receiver combinations, which could be parallel-polarized or cross-polarized with zero or non-zero offset, combinations of multiple transmitters and receivers are also widely used in practice. For example, a transmitter-receiver-transmitter (TRT) configuration (at single frequency) that has been introduced and simulated in past work leads to the cancellation of direct signals (the direct coupling signal from transmitters to receivers) and yields only the total received signals that are due to target scatter [183, 185].

In this chapter, an alternative configuration of multiple transmitters and receivers is introduced to enable the study of a multi-frequency configuration that is based on a receiver-transmitter-receiver (RTR) set-up, which has been successfully applied in practice (in both lab and field tests). Specifically, the two receivers have different center frequencies. One receiver has a high frequency that is the same as the frequency of the middle transmitter, but the other receiver has a different and lower frequency than the other receiver and transmitter. The reason for this configuration is that it allows a frequency-shift phenomenon to be observed when GPR waves travel in underground materials [44, 186–188]. In this phenomenon, the frequency of a GPR signal transmitted through geomaterials shifts downwards to a lower frequency as it propogatesthrough the medium.

Several researchers have performed studies in order to better understand this phenomenon. For example, Benedetto and Tosti [44] conducted research to analyze GPR spectra for subsurface clay content based on the frequency-shift phenomenon. Their results indicate that the recorded GPR peak frequency moves towards lower frequencies as the clay content increases. Moreover, this frequency-shift property of transmitted waves in underground media also has been used to facilitate radar attenuation tomography [186] and seismic attenuation tomography [187]. Further, Zhu et al. [189] presented a new migration algorithm by incorporating attenuation to enhance the resolution of GPR images. Based on radar theory, in most geomaterials the attenuation rate increases with frequency [190]. In other words, higher frequency signal components attenuate more rapidly than lower frequency signal components. Thus, the center frequency of transmitted signals experiences a downshift, which can be used to reconstruct the radar signature in attenuation tomography [186]. Water content is another key factor that affects the velocity and frequency of transmitting signals and thus has been evaluated using this frequency-shift method [188]. Changes in frequency also have been observed to be associated with changes in layer thickness and moisture content in asphalt pavements [191]. As noted from these aforementioned studies, the frequency of the transmitting GPR signal shifts towards lower frequencies because of attenuation as 1) the clay content or water content increases and 2) the travel distance in the media increases.

The purpose of this chapter is to describe a study aimed to improve GPR detection results based on multi-antenna configurations and the frequency-shift phenomenon. Both full-scale laboratory experiments and on-site field tests were performed to accomplish this work. First, a full-sized pavement experiment was set up in an indoor laboratory at an Indiana Department of Transportation (INDOT) Research Division facility. Second, a group of field tests were also conducted along the newly-built US-231 highway near Purdue University Airport. Three operating frequencies were employed in these experiments and tests: 270 MHz, 400 MHz, and 900 MHz. The RTR configuration was established and employed in this study to compare the detection results based on the frequency down-shift phenomenon. Specfically, two RTR configurations were developed and implemented: 1) receiver (400 MHz) - transmitter (900 MHz) - receiver (900 MHz) and 2) receiver (270 MHz) - transmitter (400 MHz) - receiver (400 MHz).

8.2 THEORETICAL BACKGROUND

The frequency of a GPR wave traveling through the subsurface is affected by the complex dielectric constant of the surroundings that, in turn, are affected by variations in the water content of the subsurface medium (among other variables). An increase in the water content can increase the loss factor and attenuation of a GPR wave, leading to a shift in the centroid/peak frequency of the wave to lower frequencies .

Quan and Harris [187] presented a linear attenuation model for seismic waves. A brief overview of their in-depth development of the model is presented here for completeness to provide the fundamental background underlying the frequency shift phenomenon observed in the experimental findings outlined in Section 8.4. First, fundamental material and wave properties are introduced to establish the link between attenuation, wave velocity, electric permittivity, magnetic susceptibility, and electric conductivity. Then, the linear system model is introduced to develop an analytical expression of the frequency shift phenomenon that highlights the experimentally observed transition to lower frequencies.

8.2.1 Material and Wave Properties

The frequency range for GPR is normally from 10 MHz to 2 GHz. The applications for GPR typically are focused on non-magnetic and resistive earth materials. Specifically, wave propagation is controlled mainly by spatial variations of dielectric permittivity ϵ in the subsurface [135]. For most dry geological materials, the dielectric constant typically falls in the range of 3 to 8 ($\epsilon_r \sim 3-8$). However, water has an anomalously large dielectric constant that is around 80 ($\epsilon_r \sim 80$). Thus, saturated soils, sand, and rocks have significantly higher dielectric constant values ($\epsilon_r \sim 10-40$) than dry materials ($\epsilon_r \sim 3-8$) [136], and the dielectric constant ϵ_r is highly sensitive to the pore-scale microstructure and volume fractions of the solid and water phases [135]. Thus, for lossy and wet earth materials, the most important factor that is needed to determine the dielectric constant ϵ_r is the volumetric water content, θ_w . Several researchers have performed experiments and/or developed models to establish the relationship between the dielectric constant ϵ_r of different soil types and their water contents θ_w and these works can be readily accessed (e.g., Topp et al. [139] for clays and loams; Carcione et al. [192] for sands containing water and LNAPL). Recognizing the influence of water in subsurface GPR applications, it's possible to look more generally at radar wave properties, as outlined below. Note that some theory from Chapter 2 is repeated here to facilitate a clear discussion of attenuation and the frequency shift phenomenon employed in this portion of the research study.

The velocity of electromagnetic (EM) waves that travel through a material can be expressed by Equation (8.1) [131].

$$v = 1/\sqrt{\mu\epsilon} \tag{8.1}$$

Specifically, the velocity of EM waves in free space, which is also known as the speed of light, is calculated as shown in Equation (8.2).

$$c = \frac{1}{\sqrt{\mu_0\epsilon_0}} = 3 \times 10^8 m/s \tag{8.2}$$

where

μ_0 is the absolute magnetic susceptibility of free space, $\mu_0 = 1.26 \times 10^{-6} Hm^{-1}$

ϵ_0 is the absolute electric permittivity of free space, $\epsilon_0 = 8.86 \times 10^{-6} Fm^{-1}$

μ is the absolute magnetic susceptibility of the medium, $\mu = \mu_0 \mu_r$

ϵ is the absolute electric permittivity of the medium, $\epsilon = \epsilon_0 \epsilon_r$

and the relative permittivity, also known as the dielectric constant, can be shown as Equation (8.3),

$$\epsilon_r = \frac{\epsilon}{\epsilon_0} \tag{8.3}$$

and the relative magnetic susceptibility, shown as Equation (8.4)

$$\mu_r = \frac{\mu}{\mu_0} \tag{8.4}$$

is 1 for non-magnetic geologic materials ($\mu_r = 1$).

Further, the EM wave velocity in a non-magnetic medium is given approximately by Equation (8.5) [25, 135, 136].

$$v = \frac{c}{\sqrt{\epsilon_r}} \tag{8.5}$$

The wavelength λ is calculated as Equation (8.6).

$$\lambda = \frac{v}{f} \tag{8.6}$$

where

λ is the wavelength when traveling in a medium (m)

v is the wave velocity when traveling in a medium (m/s)

f is the center frequency of the wave (Hz)

Attenuation α can then be expressed as a function of electric permittivity, magnetic susceptibility, and electric conductivity as in Equation (8.7).

$$\alpha = \frac{\mu \sigma v}{2} = \frac{1}{2} \sigma \sqrt{\frac{\mu}{\epsilon}} \tag{8.7}$$

where

σ is defined as electric conductivity

EM fields normally propagate as spatially damped waves when electrical losses are small. The signal amplitude decays exponentially in the direction of field translation, the β direction (the unit of β distance is meters), and the rate of decay is normally expressed as $e^{-\alpha\beta}$. In most natural earth materials, GPR wave attenuation can be primarily related to wave frequency. The attenuation generally increases with frequency. The high-frequency components of the GPR signals are attenuated more rapidly than lower-frequency components [186, 187].

In addition, the transition frequency of a GPR wave in a simple material – that is the frequency that must be exceeded to allow wave propagation (displacement currents exceed conduction currents)-can be expressed as Equation (8.8).

$$f_t = \frac{\sigma}{2\pi\epsilon} \tag{8.8}$$

In typical earth materials, the electrical and magnetic properties are normally frequency dependent and there will be a tendency for electric permittivity to decrease and electric conductivity to increase with increasing frequency [135].

Combining Equation (8.1), (8.7) and (8.8), the transition frequency can be expressed as Equation (8.9).

$$f_t = \frac{\alpha v}{\pi} \tag{8.9}$$

Then, the wave attenuation α can be expressed as a function of frequency as Equation (8.10).

$$\alpha = \frac{f_t \pi}{v} \tag{8.10}$$

8.2.2 Frequency-Shift Phenomenon Development

Linear Propagation System Model Setup

To develop an understanding of the fundamental drivers of the frequency shift phenomenon observed in the experiemental work reported herein, wave propagation in the subsurface and related attenuation can be characterized by employing a linear system model. The spectra of an incident wave (transmitted wave) and received wave, can be defined as $T(f)$ and $R(f)$, respectively. The instrument/medium response can then be characterized by $I(f)A(f)$, where

$I(f)$ accounts for geometric and instrument effects, and

$A(f)$ represents the effects of the test medium as an attenuation filter.

This system can be generally expressed as Equation (8.11) in the frequency domain [187].

$$R(f) = I(f)A(f)T(f) \tag{8.11}$$

As noted in Equation (8.10), an attenuation coefficient α_0 can be defined as

$$\alpha_0 = \frac{\pi}{v} \tag{8.12}$$

Therefore, the wave attenuation can be described as a linear model of frequency to be

$$\alpha = \alpha_0 f \tag{8.13}$$

Several studies indicate that the attenuation is usually proportional to frequency and the attenuation filter $A(f)$ can be expressed as Equation (8.14) [187, 193].

$$A(f) = \exp\left(-f \int_{ray} \alpha_0 dl\right) \tag{8.14}$$

To simplify this problem for the purposes of illustrating the frequency shift phenomenon, the factor $I(f)$ can be assumed to be independent of frequency, and will be expressed as I. Thus, Equation (8.11) can be simplified to be

$$R(f) = IA(f)T(f) \tag{8.15}$$

Frequency-Shift Phenomenon Resulting from Attenuation

To analyze the general frequency-shift phenomenon caused by attenuation along the travel path of the transmitted wave, consider the incident spectrum simply to be Gaussian in nature, so that $T(f)$ can be expressed by Equation (8.16).

$$T(f) = \exp\left[-\frac{(f - f_T)^2}{2\sigma_T^2}\right] \tag{8.16}$$

where

f_T is defined as the centroid frequency of the transmitted signal $T(f)$;

σ_T^2 is defined as the variance of the transmitted signal.

Then, employing Equations (8.15) and (8.14), the spectrum of the received signal can be calculated as

$$\begin{aligned}
R(f) &= IA(f)T(f) \\
&= I\exp\left[-\frac{(f-f_T)^2}{2\sigma_T^2} - f\int_{ray}\alpha_0 dl\right] \\
&= I\exp\left[-\frac{f^2 - 2ff_T + f_T^2 + 2\sigma_T^2 f\int_{ray}\alpha_0 dl}{2\sigma_T^2}\right] \\
&= I\exp\left[-\frac{f^2 - 2f(f_T - \sigma_T^2\int_{ray}\alpha_0 dl) + f_T^2}{2\sigma_T^2}\right] \\
&= I\exp\left[-\frac{f^2 - 2f(f_T - \sigma_T^2\int_{ray}\alpha_0 dl) + (f_T - \sigma_T^2\int_{ray}\alpha_0 dl)^2 - (\sigma_T^2\int_{ray}\alpha_0 dl)^2 + 2f_T\sigma_T^2\int_{ray}\alpha_0 dl}{2\sigma_T^2}\right] \\
&= I\exp\left[-\frac{[f - (f_T - \sigma_T^2\int_{ray}\alpha_0 dl)]^2 - (\sigma_T^2\int_{ray}\alpha_0 dl)^2 + 2f_T\sigma_T^2\int_{ray}\alpha_0 dl}{2\sigma_T^2}\right]
\end{aligned} \tag{8.17}$$

Now, define

$$f_r = f_T - \sigma_T^2\int_{ray}\alpha_0 dl \tag{8.18}$$

and

$$f_p = -(\sigma_T^2\int_{ray}\alpha_0 dl)^2 + 2f_T\sigma_T^2\int_{ray}\alpha_0 dl \tag{8.19}$$

Thus,

$$\begin{aligned}
R(f) &= I\exp\left[-\frac{f_p}{2\sigma_T^2}\right]\exp\left[-\frac{(f-f_r)^2}{2\sigma_T^2}\right] \\
&= A_R\exp\left[-\frac{(f-f_r)^2}{2\sigma_T^2}\right]
\end{aligned} \tag{8.20}$$

where

$$A_R = I\exp\left[-\frac{f_p}{2\sigma_T^2}\right] \tag{8.21}$$

Examining Equation (8.20), and its development in Equations (8.16) to (8.19), it is clear that the received signal, $R(f)$, in this situation will be Gaussian, and can be defined by Equation (8.22)

$$R(f) = A_R \exp\left[-\frac{(f - f_R)^2}{2\sigma_R^2}\right] \tag{8.22}$$

where

f_R is defined as the centroid frequency of the received signal $R(f)$, and

$$f_R = f_r = f_T - \sigma_T^2 \int_{ray} \alpha_0 dl \tag{8.23}$$

σ_R^2 is defined as the variance of the received signal, and $\sigma_R^2 = \sigma_T^2$;

A_R represents that amplitude of the received signal, showed as Equation (8.21).

Thus, shown as Equation (8.23), the centroid/peak frequency of the received signal will shift to a lower frequency by an amount controlled by the attenuation factor of the GPR wave, which is influenced by both electric permittivity and conductivity.

Based on this theoretical analysis, it is suggested that GPR waves that were transmitted from a higher frequency antenna might be received by a lower frequency antenna with better results. Lab and field experimental data which demonstrate this point are discussed in detail in Sections 8.3 and 8.4.

8.3 On-site Test Methodology and GPR Equipment

8.3.1 On-site Experiments

In order to analyze and evaluate the frequency shift of GPR waves as the waves are transmitted through subsurface media, a dual-frequency configuration that is composed of two receivers and one transmitter is introduced in this study. The order of these antennas is receiver (Rx) - transmitter (Tx) - receiver (Rx). Among these three antennas, the transmitter has the highest frequency, one of the two receivers has the same high frequency as the transmitter, and the other receiver has the lower frequency. Both lab experiments and

field surveys were performed in this study. The lab experiments were set up on a full-sized pavement structure in the Acceleration Pavement Test (APT) laboratory at the INDOT Research Division facility in West Lafayette, Indiana. The GPR antennas in this lab test were configured as shown in Figure 8.1. Additionally, a set of similar field tests was also performed along the side of US-231 close to Purdue University Airport in order to test the effects of this frequency-shift phenomenon on GPR detection of subpavement drains even further. The GPR antenna configuration for the field tests is shown in Figure 8.2.

There are two types of detectable targets –plate targets, and drainage pipes – incorporated in the laboratory experimental setup employed in this work, which are contained in a full depth flexible pavement structure (32 cm (12.5 inches) of bituminous pavement, 32 cm (12.5 inches) of subgrade soils) representative of a roadway cross-section. The targets are all spatially separated, so no interference is anticipated between the targets. For the purposes of the work reported herein, the primary target is a 7.6 cm (3-inch) diameter PVC drainage pipe, located at a depth of 64 cm (25 inches), and oriented perpendicular to the direction of the GPR survey line. The water content at different depths in the pavement structure was measured before the test was performed. The volumetric water content in the paved layers was around 7% (measured at depth 18 cm (7 inches) and 25 cm (10 inches)). The volumetric water content of the filled soils under the pavement was also measured. At 32 cm (12.5 inches) under the pavement, the volumetric water content of the soil was 13.7%, and at 40 cm (15.5 inches), was 16.8%. As noticed, the water content of soil under the pavement increased with depth. Thus, the dielectric constant of the soil increased along the path of the transmitted GPR signal.

Furthermore, the targets involved in the field tests included a group of double PVC drainage pipes (two pipes work together at the same location). The diameter of each pipe was 15.2 cm (6-inches). They were located 61 cm (2 feet) under the pavement and in the soil base layers. While testing, the pipes were empty with no water inside. According to the geotechnical report from the road construction, the soil water content under the pavement was in the lower twenty percent range. This field test was performed on June 17 and 18, 2013. There were several rainy days in the week before this test according to weather

records. And on June 13, 2013, precipitation of 1.7 cm (0.68) inches was recorded in the area. As a result, the soil under the pavement on the date of testing likely had elevated moisture levels.

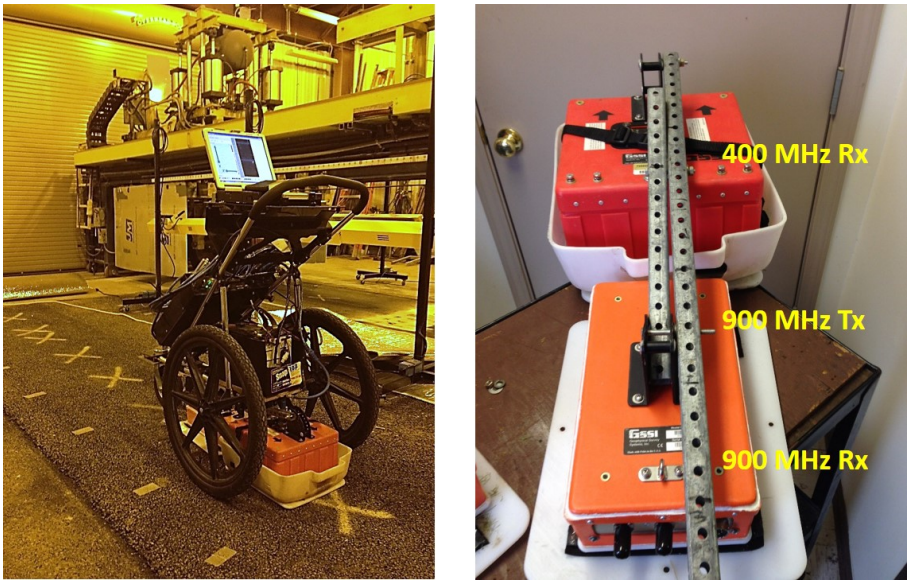

Figure 8.1.: Dual-frequency GPR antenna configuration in the INDOT APT lab.

Figure 8.2.: Field testing at new US-231 highway near Purdue University Airport.

8.3.2 GPR Equipment

The GPR equipment used in both the lab and field experiments conducted in this study is the SIR-20 system from Geophysical Survey Systems, Inc. (GSSI). The major advantage

of this system is its ability to support multi-channel and multi-frequency antennas. This study employed three antennas, the frequencies of which were selected to be 270 MHz, 400 MHz, and 900 MHz. The frequency range chosen here is known to be a popular range for underground pipe detection applications. Each antenna has both a transmitter and receiver enclosed inside the box, as shown in Figure 8.1. To conduct the dual-frequency test described in section 8.3.1, two different frequency antennas were required. For the higher frequency antenna, both the transmitter and receiver inside this antenna were kept active during the tests. However, for the lower frequency antenna, only the receiver was required to be active and the transmitter was disabled during the entire test. As shown in Figures 8.1 to 8.3, the physical orientation of these two antennas ensures that the configuration is Rx-Tx-Rx.

In the lab experiments, one set of dual-frequency (Rx-Tx-Rx) set-ups was considered. The two frequencies used were 900 MHz and 400 MHz. So, the antenna set-up mode can be expressed as Rx(400)-Tx(900)-Rx(900) for lab testing. In the field tests, an additional set of combinations was tested using the two frequencies of 400 MHz and 270 MHz. Thus, this field set-up mode can be expressed as Rx(270)-Tx(400)-Rx(400). In Figure 3 only the first mode (Rx(400)-Tx(900)-Rx(900)) is illustrated, but the second mode (Rx(270)-Tx(400)-Rx(400)) is similar. As noted, in order to establish this dual-frequency configuration, the transmitter of the lower frequency antenna must be disabled and the receiver of this antenna needs to be allowed to receive signals from other channels. The GSSI SIR-20 system can provide all the functions described herein.

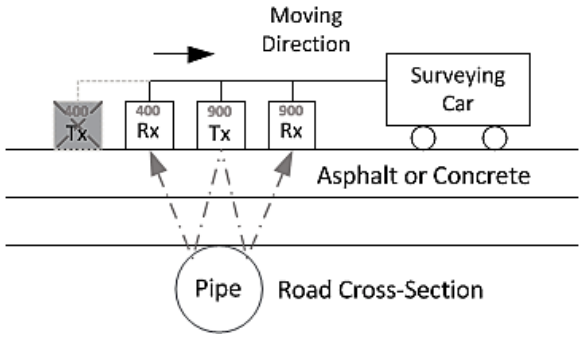

Figure 8.3.: Illustration of dual-frequency system (900 MHz and 400 MHz).

8.3.3 Antenna Frequency Bandwidth

There were three antennas involved in this study with three different center frequencies (900 MHz, 400 MHz and 270 MHz). The wavelet transmitted by these antennas is known as a Ricker Pulse or Ricker wavelet [194]. The duration of the pulse for each antenna was introduced based on the design manual and can be listed as: (a) 900 MHz antenna Ricker pulse duration:1.1 ns; (b) 400 MHz Ricker pulse duration: 2.5 ns; (c) 270 MHz Ricker pulse duration: 3.6 ns. The pusle signal in the time domain for each antenna is shown in Figure 8.4(a). The frequency band of each antenna can be obtained as a frequency spectrum by Fast Fourier Transform (FFT) as shown in Figure 8.4(b). Thus, Figure 8.4(b) illustrates that each antenna's frequency band overlaps with the lower frequency antenna's frequency band. As a result, when the frequency of a GPR signal shifts to a lower frequency when transmitted through the subpavement, it can be picked up by a lower frequency antenna.

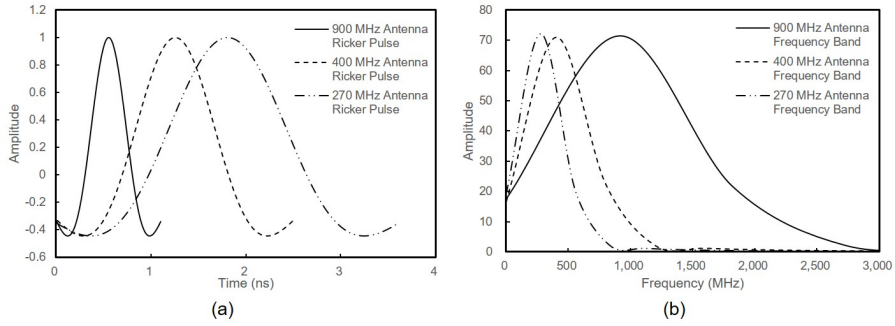

Figure 8.4.: Antenna Pulse and Frequency Bandwidth (a) Antenna Transmitted Ricker Pulse (b) Antenna Frequency Bandwidth.

8.4 Analysis of On-site GPR Tests with Dual-Frequency Antenna Configurations

8.4.1 Data Interpretation Methodology

The center frequency of a GPR wave has significant potential to shift to a lower value when the wave travels through subsurface materials. This phenomenon is described herein as the frequency-shift phenomenon, and the theoretical development outlined in Section

8.2 shows that this phenomenon has a sound foundation and, if accommodated, can be beneficial for underground target detection. The on-site detection data can be interpreted in the frequency domain to obtain a clear understanding of the center frequency shift. Several steps of analysis must be taken to reach the final result, as follows.

Obtain GPR waves in the time domain: Initial GPR waves are recorded based on the time delay that is due to the scattering of incident energy by potential targets or subsurface boundaries. In this study, the GPR reflection wave to be analyzed was selected at the location of a known target. Figure 8.5(a) presents the time domain representation of the signal.

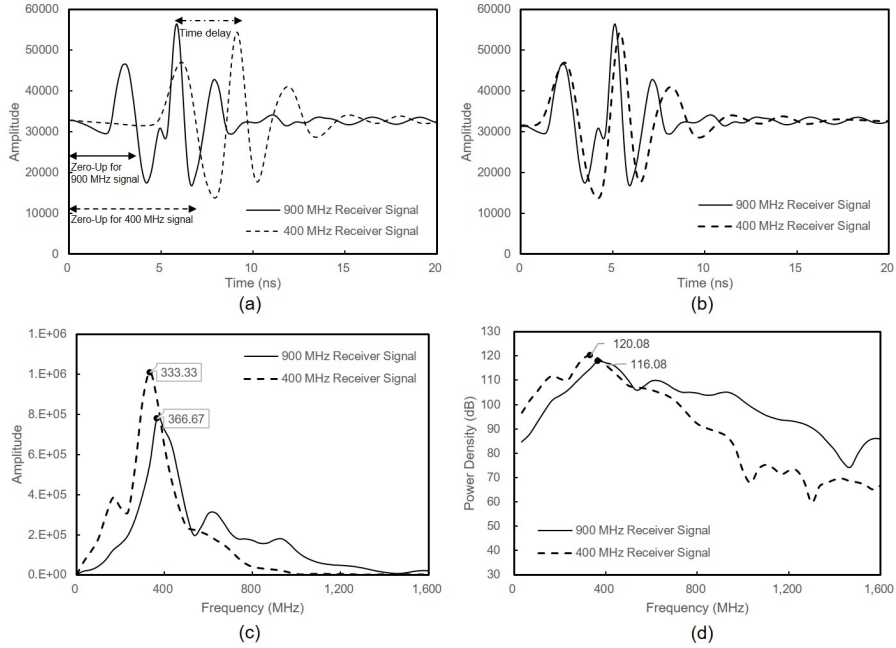

Figure 8.5.: GPR signals received by 900 MHz receiver and 400 MHz receiver at target locations under the laboratory test pavement: (a)Time domain signals; (b) Zero-up adjusted time domain signals; (c) Frequency domain signals; (d) Power spectra of signals. (Excitation at 900 MHz)

Remove the direct wave from the transmitter to the receiver: The first reflection recorded in a GPR receiver is referred to as the 'direct wave' in GPR theory. This signal is

transmitted directly from the transmitter to the receiver. Normally, in the analysis of GPR results, the direct wave needs to be removed in order to avoid possible confusion. This algorithm is also known as a zero-up algorithm in GPR data processing. Due to the effects of the direct wave of the GPR signals and the offset between the two installed antennas, the zero-up algorithm was applied to adjust the zero point of each signal. Thus, the two signals at both frequencies aligned simultaneously, as shown in Figure 8.5(b).

Transfer the time-domain data into the frequency domain by fast Fourier transform (FFT): In order to analyze the center frequency values recorded by both receivers in each set of experiments, the original time-domain data can be transferred to the frequency domain using the fast Fourier transform (FFT) method, which is shown in Figure 8.5(c). The peak value of the curve is the center/peak frequency of the recorded signal.

Obtain the power spectrum of the analyzed signal: To evaluate the power density of the signal that is being analyzed, the power spectrum of each signal should be obtained as well. The power spectrum gives a view of the portion of a signal's power (energy per unit time) that falls within given frequency bins. This plot also can be generated using FFT. Figure 8.5(d) presents the power spectra of the processed signals in dB units.

8.4.2 Lab Testing Analysis

As discussed in Section 8.3.1, on-site tests were performed on a full-sized pavement in the APT lab at the INDOT Research Division facility. As part of this testing, the dual-frequency antenna configuration, Rx(400MHz)-Tx(900MHz)-Rx(900MHz), was employed to evaluate the frequency-shift phenomenon discussed in Section 8.2.2. The experiments, set up as shown in Figure 8.1, were performed at a test location where a 7.6 cm (3-inch) diameter PVC pipe (64 cm (25-inches) deep) underneath the pavement could be analyzed. Figure 8.5(a) shows the time domain signals received by both the 900 MHz receiver and the 400 MHz-receiver, while Figure 8.5(b) shows the time domain signals after the zero-up algorithm.

Next, FFT was applied to both signals obtained from the previous steps. Frequency domain analysis was performed; Figure 8.5(c) presents the frequency spectra of the received signals. The solid line represents the frequency spectrum of the signal received by the 900 MHz receiver, whereas the transmitted signal was 900 MHz originally. However, as shown in Figure 8.5(c), the peak frequency of the signal received by the 900 MHz receiver was 366.67 MHz, which indicates a significant frequency drop during transmission under the pavement, compared to the dashed line in this figure, which represents the frequency spectrum of the signal received by the 400 MHz receiver, where again the transmitted signal is 900 MHz. On this dashed line, the peak frequency is 333.33 MHz and the amplitude is higher than that of the 900 MHz receiver signal.

The power spectra also were plotted in Figure 8.5(d) to show the power density of each signal. As indicated in this figure, the peak power density value in the signal received by the 400 MHz receiver is 120.8 dB and the peak power density value in the signal received by the 900 MHz receiver is 116.08 dB. Thus, the scattered component of the signal (target reflection) from the same original transmitted source is picked up more easily from the lower frequency antenna than the higher frequency antenna due to the frequency-shift phenomenon observed in this study.

In this case, the original transmitted 900 MHz signal shifted downwards to around 350 MHz, which made this signal more easily received by a low frequency antenna (400 MHz in this case). Moreover, this lower frequency receiver successfully received the signal transmitted from the higher frequency transmitter (900 MHz). The dashed line is evidence of this occurrence.

As shown in Figures 8.5(a) to 8.5(d), two observations can be made from these tests:

- The frequency of a signal transmitted through earth materials (moist materials) can display an obvious downwards frequency shift.
- A lower frequency receiver can more easily receive this frequency-shifted signal and obtain a higher energy level for the scattered signal component.

8.4.3 Field Test Results

In addition to the APT lab tests, other on-site tests were performed in the field at a section of US-231 near Purdue University Airport. Figure 2 shows the equipment that was set up along the paved shoulder of the roadway. Dual-frequency receiver tests also were performed during this study. In addition to the same configuration that was used in the lab (400Rx-900Tx-900Rx), a similar configuration also was tested to investigate a greater penetration depth (270Rx-400Tx-400Rx) with a lower frequency range. A similar analysis approach was applied to these field data, where a pair of known 15.2 cm (6-inch) pipe targets location was selected to be the interest point. The depth of this target was about 61 cm (2 feet). The pipes were empty at the time of testing.

The frequency-domain signal analysis results for these two sets of field tests are shown in Figure 8.6 and Figure 8.7. Figure 8.6 shows the frequency analysis of the signals received by both a 400 MHz receiver and 900 MHz receiver based on the 400Rx-900Tx-900Rx configuration. These results indicate that the original 900 MHz center frequency shifted down to a peak frequency for both signals of around 360 MHz, which is close to the lower frequency receiver's center frequency. Furthermore, the amplitude of the signal captured by the lower frequency receiver is higher than the amplitude captured by the higher frequency receiver. Specifically, the signal received by the lower frequency receiver clearly has a higher power density value at the peak frequency point.

Figure 8.7 presents similar analysis results for the 270Rx-400Tx-400Tx configuration. In this case, the original signal transmitted with 400 MHz center frequency has shifted down to around 240 MHz. Again, the signal received by the lower frequency receiver (270Rx) has higher power density values at the peak frequency point.

In summary, both the lab and field test results show clear evidence that the frequency of GPR waves has high potential to shift down to a lower frequency when the waves are being transmitted through subsurface materials. This phenomenon provides an opportunity to detect the frequency-shifted signal with a lower frequency receiver with higher energy. This observation implies that the lower frequency antenna has the potential to observe targets at

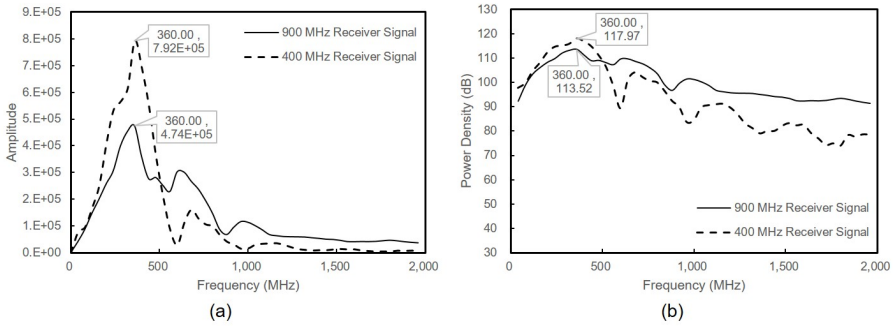

Figure 8.6.: Frequency domain analysis results for 400Rx-900Tx-900Rx configuration: (a) frequency spectra of signals and (b) power spectra of signals.

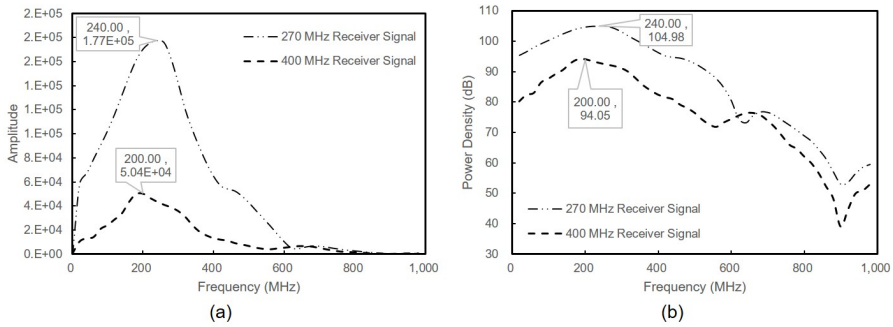

Figure 8.7.: Frequency domain analysis results for 270Rx-400Tx-400Rx configuration: (a) frequency spectra of signals and (b) power spectra of signals.

greater distance, of a smaller scale, and/or in a more noise clouded environment than would otherwise be successfully detected by a receiver with a center frequency matching that of the transmitter. A full discussion and analysis of these possibilities requires more complex field scenarios than presented herein, as well as comprehensive presentation of the signal and data processing algorithms used to define target detection. However, the authors have conducted such a study which indicated up to a 3.3 fold increase in SNR_{db} values for the 400 MHz receiver relative to the 900 MHz receiver in a 400Rx-900Tx-900Rx configuration, discernible target detection on roadway edges with the 400 MHz receiver that could not be identified by the 900 MHz receiver, and improvement from non-detect of known targets under an active roadway using traditional 400 MHz analyses to successful detection following signal processing of the 400Rx-900Tx-900Rx data using a newly developed

background clutter reduction algorithm. For further details of this study, the reader is referred to Sinfield and Bai [150]. Overall, the dual-frequency configuration introduced in this chapter has the potential to serve as a beneficial alternative to standard GPR antenna configurations that can facilitate improved target detection in the field.

8.5 Summary

This chapter discusses the frequency-shift phenomenon that occurs when signals are transmitted through earth materials that contain moisture, such as soil, clay, or gravel. Based on the analysis and results presented, several conclusions can be drawn from this study.

1. When GPR signals are transmitted through wet subsurface materials, the frequency of the transmitted signal can shift downwards to a lower frequency. This phenomenon was demonstrated both through theoretical formulation and on-site experiments, including lab experiments and field tests.

2. The magnitude of the frequency shift is highly dependent upon the dielectric constant, electric conductivity, and magnetic susceptibilty of the materials and related wave attenuation rate. The condition of materials in the subsurface is typically difficult to predict precisely. Thus, the exact amount that the transmitted frequency may shift is hard to determine prior to field work. However, the possible range can be estimated based on the known material properties of the subsurface using established relationships between soil types and key properties affecting wave propagation, which can be helpful in antenna selection for a dual-frequency system.

3. A novel dual-frequency antennae configuration is introduced in this study. This type of configuration can be expressed as Rx(low frequency)-Tx(high frequency)-Rx(high frequency). This configuration was applied successfully in both lab experiments and field tests, the results of which demonstrated the frequency-shift phenomenon described by theory. As the peak return frequency shifted close to the center frequency

of the lower frequency receiver, this signal could be observed more easily from this lower frequency receiver with greater power density than was achievable with the receiver having the same center frequency as the transmitter.

9. CONCLUSIONS AND RECOMMENDATIONS

[1]As noted earlier, the work carried out in this program involved a two-pronged approach to improve GPR-based sub-pavement drainage system evaluation. Two major avenues were explored to achieve improvements in GPR detection success: 1) software-based signal processing and 2) modifications of hardware test configurations.

Two complementary sets of signal processing approaches were developed in this work, referred to herein as Methods 1 and 2. Method 1 involves two signal processing algorithms that are designed to reduce background clutter and noise by taking advantage of the somewhat uniform nature of the strata underlying constructed pavements and to systematically remove anomalous signals. The output of this method is a 1-D plot of potential target locations as a function of distance on the survey line along the roadway. This method proved to be very effective at identifying buried pipes even when a hyperbolic signal return could not be observed in the 2-D data. Generally all X-drains are routinely identified (with only occasional exceptions), with 3 to 4 false alarms per successful detection. Similarly, all known K-drains in the studied field test regions were successfully identified even though none could be observed in the original GPR images, although each successful detection was accompanied by a significant number of potential false alarms. While these false alarms all require field investigation, the effort associated with these investigations is likely substantially less than the effort required to manage the consequences of undetected, and thus unmaintained, K-drains. The reliability of Method 1 was shown to improve when scans obtained with two antennae are compared, and when routine drain spacing is employed as a filter. These additional screens help to reduce false alarms to roughly 2 to 3 per successful detection for X-drains. Note that accurate false alarm statistics could not be developed for K-drains, because the total number of K-drains in the field test area is not known.

[1]This chapter is mainly from the published JTRP report (Report Number: FHWA/IN/JTRP-2013/25) "Nondestructive Evaluation of the Condition of Subsurface Drainage in Pavements Using Ground Penetrating Radar (GPR)" [150]

Method 2 focuses on enhancing 2-D image quality to facilitate recognition of hyperbolic signal returns indicative of a drain detection. When this method reveals a hyperbola, there is a clear "detect" outcome and thus the approach can clarify interpretation of potential targets identified via Method 1. It is important to note however, that lack of a hyperbolic return in the 2-D image is not conclusive in declaring a "false alarm" as the statistical algorithms of Method 1 routinely detected pipes when no hyperbolic return was visible. Thus, in practice, it is likely important to investigate all potential target zones identified by Method 1. Overall, Method 2 would likely be most valuable if incorporated in an automated data processing system to help rapidly identify clear "detects" and thus limit the focus of in-field investigative study to only truly uncertain target zones.

Field experiments were also carried out in this work to assess the potential for alternative antenna configurations to enhance the detection success. Five different antenna configurations were tested. These tests reveal several conclusions that can be generalized as follows:

1. Survey line selection has a significant influence on the quality of obtained GPR images. In all cases,images obtained on the gravel side slope of roads provided clearer, higher SNR, images of buried drains relative to images obtained in the middle of the shoulder of the roadway, and more frequently displayed the characteristic hyperbolic returns expected from a buried conduit. For example, as described in association with the test of the dual-parallel 270MHz antennae, the signal to background ratio (SNR_dB) on the gravel slope was 11dB and on the shoulder decreased to 9.5dB. While in this particular case, both survey lines resulted in a detection, an enhanced SNR provides the opportunity to detect pipes that may be more deeply buried or in less favourable ground conditions and thus the survey line that routinely provides the greatest SNR should always be sought. It is believed that this result stems from the reduced surface cover over the drains on the gravel slope which permits more energy to reach the target zone. It is also worth noting that while operating on the gravel slope has some challenges in terms of maintaining the stability of the antennae, a survey line well off the roadway adds to the safety of the overall scanning operation.

With this in mind, there is likely value in developing a robust outrigger setup that can facilitate antenna coupling with the ground on the gravel slopes beside roadways.

Tests carried out at the pavement shoulder – gravel slope interface repeatedly yielded poor results. The interface between the pavement edge and the gravel is highly heterogeneous and limits coupling of energy into the subsurface. In addition, it is difficult to obtain a reliable background signal in this region. Survey lines at the pavement shoulder – gravel slope interface should therefore be avoided.

2. Test configurations involving two antennae facilitate more reliable detection strategies than single antennae configurations. As highlighted earlier, the potential to compare results from two antennae along a shared survey line helps to distinguish background clutter and anomalies from actual pipe detections and facilitates signal averaging that can be employed to reduce the net background interference in post-processing. The benefits of this logic likely increase to a limit as additional antennae are added to the test setup. Some researchers have demonstrated the value of employing large antenna arrays, however these types of systems (which can cost hundreds of thousands to millions of dollars to develop (see for example Project ORFEUS being pursued by the European Community)) were cost prohibitive to explore in this study.

3. In tests conducted with a transmitter and dual receivers operating at different frequencies (e.g., 900 Tx and 900/400 Rx; or 400 Tx and 400/270 Rx), higher input frequencies yielded higher SNR_dB results than lower input frequencies. However, at any given input frequency results obtained with the lower frequency receiver of the studied pair tended to provide higher SNR_dB returns, indicating some loss in energy of the returned signal combined with a beneficial reduction in sensitivity to noise.

4. Cross polarized configurations generally provided good results but did not yield a benefit that justified the added complexity of operating the cross polarized system. It is important to note that only configurations involving a cross-polarized receiver oriented perpendicular to the transmitter and direction of travel and vice versa were

pursued in this work. Other orientations of the entire cross-polarized setup (e.g., 45°relative to the direction of travel), may warrant future investigation.

Based on the tests and data analyses performed herein, the following recommendations are provided to guide future deployments of GPR for subsurface drainage detection under pavements:

1. Implement the background reduction and anomaly detection algorithms developed in this work (Method 1) in a user friendly software application that can be employed to process GPR data

2. Implement the shape enhancement algorithms developed in this work (Method 2) to facilitate evaluation of potential target zones via a an automated shape recognition routine

3. Enhance on-board computing power employed in the field vehicle used to pull the GPR antennae so that data can be processed in real-time, thereby enabling target zone marking during the GPR scanning operation (vs. post data processing)

4. Develop a robust GPR unit outrigger capable of negotiating the gravel slopes alongside roadways to maximize energy coupling into the subsurface and enhance detection sensitivity

5. Deploy (at least) two antennae in any survey operation to improve background management and facilitate results comparison that can increase the probability of successful detection and false alarm rejection

6. Utilize configurations involving one transmitter and dual-frequency high-low receiver pairs to optimize energy input into the subsurface and minimize received noise. (Note the simulations indicated that a dual-transmitter shared frequency system would be promising but equipment limitations prevented field study of this configuration).

Beyond these recommendations, this study also identified several issues that likely warrant future research, such as:

1. Instead of a fixed threshold selected in the moving background clutter removal algorithms in Chapter 6, a changing threshold can be generated based on constant false alarm rate (CFAR) detection theory. In this case, the threshold level is raised and lowered to maintain a constant probability of false alarm. CFAR techniques have already been successfully performed in GPR applications, especially in landmine detection applications [195–198]. Threshold selection based on Cell-Averaging CFAR or other newly developed CFAR approaches could potentially improve the detection results of the background reduction method proposed in this research and reduce the false alarm rates, and thus likely merits investigation.

2. Increasing the offset between transmitters and receivers of the same frequency. Simulations carried out in this study showed improvements in detection sensitivity with an offset between the Tx and Rx antennae. Unfortunately, due to the design of the equipment utilized in this study, this configuration change could not be evaluated and may prove helpful in challenging detection circumstances.

3. Employing unique sensing techniques to overcome the challenges posed by water in the soil. As noted throughout this report, it is hypothesized that some sub-pavement drains may be positioned in clay layers that also tend to retain moisture, thus limiting propagation of electromagnetic radiation at typical GPR frequencies, which makes it challenging to detect their location. With this in mind, two avenues of future research may be helpful to enhance the pipe detection rate and reduce false alarms in these difficult conditions:

    (a) It may be useful to combine the GPR unit with a commercial grade metal detector in an attempt to increase effectiveness in locating metal K-drains by inducing and subsequently monitoring for changes in magnetic field;

(b) It may also be helpful to exploit recent research on propagation of electromagnetic waves through water in the frequency range of 3-100MHz to minimize the influence of water, which may be especially common in clay layers.

4. Significantly refining the hardware design of the GPR system to enable step frequency analysis and/or the use of dielectric focusing elements to enhance energy coupling with the ground.

Overall, the advances made in this work have provided insights that have been directly translated into practice and it is hoped that this work serves as a foundation for continued improvement in the effectiveness and ease of use of the GPR technique.

REFERENCES

REFERENCES

[1] Hyung Seok Jeong, Carlos A Arboleda, Dulcy M Abraham, Daniel W Halpin, and Leonhard E Bernold. Imaging and locating buried utilities. *Joint Transportation Research Program,*, Publication FHWA/IN/JTRP-2003/12, 2003.

[2] BJ Allred, NR Fausey, L. Peters Jr, C. Chen, JJ Daniels, and H. Youn. Detection of buried agricultural drainage pipe with geophysical methods. *Applied Engineering in Agriculture*, 20(3):307–318, 2004.

[3] R.P. Szuch, J.G. White, M.J. Vepraskas, and J.A. Doolittle. Application of ground penetrating radar to aid restoration planning for a drained carolina bay. *Wetlands*, 26(1):205–216, 2006.

[4] O. Hunaidi, P. Giamou, et al. Ground-penetrating radar for detection of leaks in buried plastic water distribution pipes. In *Seventh International Conference on Ground Penetrating Radar (GPR'98)*, pages 783–786, 2010.

[5] E. Rmeili and T. Scullion. Detecting stripping in asphalt concrete layers using ground penetrating radar. *Transportation Research Record: Journal of the Transportation Research Board*, 1568(-1):165–174, 1997.

[6] U.B. Halabe. Detection of sub-surface anomalies in concrete bridge decks using ground penetrating radar. *ACI materials journal*, 94(5), 1997.

[7] C. Maierhofer. Nondestructive evaluation of concrete infrastructure with ground penetrating radar. *Journal of materials in civil engineering*, 15:287, 2003.

[8] D. Devaru, U.B. Halabe, B. Gopalakrishnan, and S. Agrawal. Ground penetrating radar (GPR) based system for nondestructive detection of interior defects in wooden logs. *International Journal of Manufacturing Research*, 3(4):425–451, 2008.

[9] L Crocco, G Prisco, F Soldovieri, and NJ Cassidy. Early-stage leaking pipes gpr monitoring via microwave tomographic inversion. *Journal of Applied Geophysics*, 67(4):270–277, 2009.

[10] A Cataldo, R Persico, G Leucci, Egidio De Benedetto, Giuseppe Cannazza, L Matera, and L De Giorgi. Time domain reflectometry, ground penetrating radar and electrical resistivity tomography: a comparative analysis of alternative approaches for leak detection in underground pipes. *NDT & E International*, 62:14–28, 2014.

[11] Gary R Olhoeft. Maximizing the information return from ground penetrating radar. *Journal of Applied Geophysics*, 43(2-4):175–187, 2000.

[12] INDOT. *Road Design Manual*, 2010.

[13] D.A. Harris. *Pavement thickness evaluation using ground penetrating radar*. PhD thesis, Purdue University, 2006.

[14] J. Mallela, L. Titus-Glover, and M.I. Darter. Considerations for providing subsurface drainage in jointed concrete pavements. *Transportation Research Record: Journal of the Transportation Research Board*, 1709(1):1–10, 2000.

[15] M.G. Hagen and G.R. Cochran. Comparison of pavement drainage systems. *Transportation Research Record: Journal of the Transportation Research Board*, 1519(-1):1–10, 1996.

[16] H.F. Hassan and T.D. White. Locating the drainage layer for bituminous pavements in indiana. 1996.

[17] H.H. Ridgeway. Pavement subsurface drainage systems. *NCHRP Synthesis of Highway Practice*, (96), 1982.

[18] G.W. Ring III. Drainage of concrete pavement structures. In *International Conference on Concrete Pavement Design*, 1977.

[19] Z. Ahmed, T.D. White, and P.L. Bourdeau. Pavement drainage and pavement-shoulder joint evaluation and rehabilitation. 1993.

[20] G. AASHTO. 'guide for design of pavement structures. *American Association of State Highway and Transportation Officials, Washington, DC*, 1993.

[21] H.F. Hassan, T.D. White, R. McDaniel, and D. Andrewski. Indiana subdrainage experience and application. *Transportation Research Record: Journal of the Transportation Research Board*, 1519(-1):41–50, 1996.

[22] G.W. Stimson. *Introduction to airborne radar*. SciTech Pub., 1998.

[23] A. Loulizi. *Development of Ground Penetrating Radar Signal Modeling and Implantation for Transportation Infrastructure Assessment*. PhD thesis, Virginia Polytechnic Institute and State University, 2001.

[24] B.N.O. Attoh-Okine. *Engineering-Economic Assessment of Paved Road Thickness Using Ground Penetrating Radar (GPR)*. PhD thesis, University of Kansas, 1993.

[25] D.J. Daniels. *Ground penetrating radar*. Wiley Online Library, 2005.

[26] Katerina Zajícová and Tomas Chuman. Application of ground penetrating radar methods in soil studies: A review. *Geoderma*, 343:116–129, 2019.

[27] Maurizio Ercoli, Lucio Di Matteo, Cristina Pauselli, Paolo Mancinelli, Stefano Frapiccini, Lorenzo Talegalli, and Andrea Cannata. Integrated gpr and laboratory water content measures of sandy soils: From laboratory to field scale. *Construction and Building Materials*, 159:734–744, 2018.

[28] Christian N Koyama, Hai Liu, Kazunori Takahashi, Masanobu Shimada, Manabu Watanabe, Tseedulam Khuut, and Motoyuki Sato. In-situ measurement of soil permittivity at various depths for the calibration and validation of low-frequency sar soil moisture models by using gpr. *Remote Sensing*, 9(6):580, 2017.

[29] Yizhu Lu, Wenlong Song, Jingxuan Lu, Xuefeng Wang, and Yanan Tan. An examination of soil moisture estimation using ground penetrating radar in desert steppe. *Water*, 9(7):521, 2017.

[30] Colby M Steelman and Anthony L Endres. Assessing vertical soil moisture dynamics using multi-frequency gpr common-midpoint soundings. *Journal of Hydrology*, 436:51–66, 2012.

[31] Mohammad Reza Mahmoudzadeh Ardekani. Off-and on-ground gpr techniques for field-scale soil moisture mapping. *Geoderma*, 200:55–66, 2013.

[32] RA Van Overmeeren, SV Sariowan, and JC Gehrels. Ground penetrating radar for determining volumetric soil water content; results of comparative measurements at two test sites. *Journal of Hydrology*, 197(1-4):316–338, 1997.

[33] Julien Minet, Patrick Bogaert, Marnik Vanclooster, and Sébastien Lambot. Validation of ground penetrating radar full-waveform inversion for field scale soil moisture mapping. *Journal of Hydrology*, 424:112–123, 2012.

[34] Francois Lavoué, Romain Brossier, Ludovic Métivier, Stéphane Garambois, and Jean Virieux. Two-dimensional permittivity and conductivity imaging by full waveform inversion of multioffset gpr data: A frequency-domain quasi-newton approach. *Geophysical Journal International*, 197(1):248–268, 2014.

[35] CP Oden, GR Olhoeft, DL Wright, and MH Powers. Measuring the electrical properties of soil using a calibrated ground-coupled gpr system. *Vadose Zone Journal*, 7(1):171–183, 2008.

[36] Anh Phuong Tran, Patrick Bogaert, François Wiaux, Marnik Vanclooster, and Sébastien Lambot. High-resolution space–time quantification of soil moisture along a hillslope using joint analysis of ground penetrating radar and frequency domain reflectometry data. *Journal of Hydrology*, 523:252–261, 2015.

[37] L Weihermüller, JA Huisman, Sébastien Lambot, M Herbst, and H Vereecken. Mapping the spatial variation of soil water content at the field scale with different ground penetrating radar techniques. *Journal of Hydrology*, 340(3-4):205–216, 2007.

[38] Zelimkhan Khakiev, Vladimir Shapovalov, Alexander Kruglikov, Andrey Morozov, and Victor Yavna. Investigation of long term moisture changes in trackbeds using gpr. *Journal of Applied Geophysics*, 110:1–4, 2014.

[39] Kaijun Wu, Gabriela Arambulo Rodriguez, Marjana Zajc, Elodie Jacquemin, Michiels Clément, Albéric De Coster, and Sébastien Lambot. A new drone-borne gpr for soil moisture mapping. *Remote Sensing of Environment*, 235:111456, 2019.

[40] Akinniyi Akinsunmade, Sylwia Tomecka-Suchoń, and Paweł Pysz. Correlation between agrotechnical properties of selected soil types and corresponding gpr response. *Acta Geophysica*, 67(6):1913–1919, 2019.

[41] D De Benedetto, A Castrignano, D Sollitto, and F Modugno. Spatial relationship between clay content and geophysical data. *Clay Minerals*, 45(2):197–207, 2010.

[42] Fabio Tosti, Claudio Patriarca, Evert Slob, Andrea Benedetto, and Sébastien Lambot. Clay content evaluation in soils through gpr signal processing. *Journal of Applied Geophysics*, 97:69–80, 2013.

[43] Tina Wunderlich and Wolfgang Rabbel. Absorption and frequency shift of gpr signals in sandy and silty soils: empirical relations between quality factor q, complex permittivity and clay and water contents. *Near Surface Geophysics*, 11(2):117–128, 2013.

[44] Francesco Benedetto and Fabio Tosti. GPR spectral analysis for clay content evaluation by the frequency shift method. *Journal of Applied Geophysics*, 97:89–96, 2013.

[45] Hao Bai and Joseph V Sinfield. Effects of gpr antenna configuration on subpavement drain detection based on the frequency-shift phenomenon. *Journal of Applied Geophysics*, 146:198–207, 2017.

[46] S. Hubbard, J. Chen, K. Williams, J. Peterson, and Y. Rubin. Environmental and agricultural applications of GPR. In *Proceedings of the 3rd International Workshop on Advanced Ground Penetrating Radar*, pages 45–49, 2005.

[47] M.B. Kowalsky, S. Finsterle, J. Peterson, S. Hubbard, Y. Rubin, E. Majer, A. Ward, and G. Gee. Estimation of field-scale soil hydraulic and dielectric parameters through joint inversion of GPR and hydrological data. *Water Resour. Res*, 41(11):W11425, 2005.

[48] N. Linde, J. Chen, M.B. Kowalsky, and S. Hubbard. Hydrogeophysical parameter estimation approaches for field scale characterization. *Applied Hydrogeophysics*, pages 9–44, 2006.

[49] M. Beres Jr and FP Haeni. Application of ground-penetrating-radar methods in hydrogeologie studies. *Ground Water*, 29(3):375–386, 1991.

[50] D.J. Inman, J.T. Ammons, R.E. Yoder, and R.S. Freeland. Soil investigations using electromagnetic induction and ground-penetrating radar in southwest tennessee. *Soil Science Society of America Journal*, 66(1):206–211, 2002.

[51] Xiuwei Liu, Xuejun Dong, and Daniel I Leskovar. Ground penetrating radar for underground sensing in agriculture: a review. *International Agrophysics*, 30(4), 2016.

[52] R.E. Yoder, R.S. Freeland, J.T. Ammons, and L.L. Leonard. Mapping agricultural fields with GPR and EMI to identify offsite movement of agrochemicals. *Journal of applied geophysics*, 47(3):251–259, 2001.

[53] Chameera Illawathure, Mumtaz Cheema, Vanessa Kavanagh, and Lakshman Galagedara. Distinguishing capillary fringe reflection in a gpr profile for precise water table depth estimation in a boreal podzolic soil field. *Water*, 12(6):1670, 2020.

[54] Daniela De Benedetto, Francesco Montemurro, and Mariangela Diacono. Repeated geophysical measurements in dry and wet soil conditions to describe soil water content variability. *Scientia Agricola*, 77(5), 2020.

[55] K. Oleschko, G. Korvin, A. Muñoz, J. Velazquez, ME Miranda, D. Carreon, L. Flores, M. Martínez, M. Velásquez-Valle, F. Brambila, et al. Mapping soil fractal dimension in agricultural fields with GPR. *Nonlin. Processes Geophys*, 15:711–725, 2008.

[56] Sabrina Mohd Ariffin, Mohamed Azwan Mohamed Zawawi, and Hasfalina Che Man. Evaluation of groundwater pollution risk (gpr) from agricultural activities using drastic model and gis. In *IOP Conference Series: Earth and Environmental Science*, volume 37, pages 1–22, 2016.

[57] TJ Gish, CST Daughtry, CL Walthall, and KJS Kung. Quantifying impact of hydrology on corn grain yield using ground-penetrating radar. In *Proceedings of the Tenth International Conference on Ground Penetrating Radar (GPR), 2004.*, pages 493–496. IEEE, 2004.

[58] S. Woeckel, M. Konstantinovic, J. Sachs, P.S. Lammers, and M. Kmec. Application of ultra-wideband m-sequence-radar to detect sugar beets in agricultural soils. In *11th International Conference on Ground Penetrating Radar, June*, pages 19–22, 2006.

[59] Petr Karásek and Eva Nováková. Agricultural tile drainage detection within the year using ground penetrating radar. *Journal of Ecological Engineering*, 21(4):205–213, 2020.

[60] TRIVEN Koganti, EVD Vijver, BARRY J Allred, Mogens Humlekrog Greve, Jørgen Ringgaard, and Bo Vangsø Iversen. Evaluating the performance of a frequency-domain ground penetrating radar and multi-receiver electromagnetic induction sensor to map subsurface drainage in agricultural areas. In *Proceedings of the 5th Global Workshop on Proximal Soil Sensing, Missouri, USA*, volume 28, pages 29–34, 2019.

[61] Barry Allred, DeBonne Wishart, Luis Martinez, Harry Schomberg, Steven Mirsky, George Meyers, John Elliott, and Christine Charyton. Delineation of agricultural drainage pipe patterns using ground penetrating radar integrated with a real-time kinematic global navigation satellite system. *Agriculture*, 8(11):167, 2018.

[62] B. ALLRED, N. FAUSEY, J. Daniels, C. Chen, L. Peters, and H. Youn. Considerations for using ground penetrating radar to locate buried agricultural drainage pipe. In *ASAE Annual International Meeting*, number 032344, 2003.

[63] Triven Koganti, Ellen Van De Vijver, Barry J Allred, Mogens H Greve, Jørgen Ringgaard, and Bo V Iversen. Mapping of agricultural subsurface drainage systems using a frequency-domain ground penetrating radar and evaluating its performance using a single-frequency multi-receiver electromagnetic induction instrument. 2020.

[64] BJ Allred, JJ Daniels, NR Fausey, C. Chen, L. Peters Jr, and H. Youn. Important considerations for locating buried agricultural drainage pipe using ground penetrating radar. *Applied Engineering in Agriculture*, 21(1):71–87, 2005.

[65] Wenke Zhao, Emanuele Forte, Federica Fontana, Michele Pipan, and Gang Tian. Gpr imaging and characterization of ancient roman ruins in the aquileia archaeological park, ne italy. *Measurement*, 113:161–171, 2018.

[66] Wenke Zhao, Emanuele Forte, Michele Pipan, and Gang Tian. Ground penetrating radar (gpr) attribute analysis for archaeological prospection. *Journal of Applied Geophysics*, 97:107–117, 2013.

[67] Lawrence B Conyers. Analysis and interpretation of gpr datasets for integrated archaeological mapping. *Near Surface Geophysics*, 13(6):645–651, 2015.

[68] G Leucci, L De Giorgi, G Di Giacomo, I Ditaranto, I Miccoli, and G Scardozzi. 3d gpr survey for the archaeological characterization of the ancient messapian necropolis in lecce, south italy. *Journal of Archaeological Science: Reports*, 7:290–302, 2016.

[69] Wenke Zhao, Emanuele Forte, Sara Tiziana Levi, Michele Pipan, and Gang Tian. Improved high-resolution gpr imaging and characterization of prehistoric archaeological features by means of attribute analysis. *Journal of Archaeological Science*, 54:77–85, 2015.

[70] M. Pipan, L. Baradello, E. Forte, A. Prizzon, and I. Finetti. 2-d and 3-d processing and interpretation of multi-fold ground penetrating radar data: a case history from an archaeological site. *Journal of Applied Geophysics*, 41(2):271–292, 1999.

[71] J. Leckebusch. Two-and three-dimensional ground-penetrating radar surveys across a medieval choir: a case study in archaeology. *Archaeological Prospection*, 7(3):189–200, 2000.

[72] Urs Böniger and Jens Tronicke. Integrated data analysis at an archaeological site: A case study using 3d gpr, magnetic, and high-resolution topographic data. *Geophysics*, 75(4):B169–B176, 2010.

[73] V. Basile, MT Carrozzo, S. Negri, L. Nuzzo, T. Quarta, and AV Villani. A ground-penetrating radar survey for archaeological investigations in an urban area (lecce, italy). *Journal of Applied Geophysics*, 44(1):15–32, 2000.

[74] B.K. Sternberg and J.W. McGill. Archaeology studies in southern arizona using ground penetrating radar. *Journal of Applied Geophysics*, 33(1):209–225, 1995.

[75] G. da Silva Cezar, P.L. Ferrucio da Rocha, A. Buarque, and A. da Costa. Two brazilian archaeological sites investigated by GPR: Serrano and morro grande. *Journal of applied geophysics*, 47(3):227–240, 2001.

[76] D. Goodman. Ground-penetrating radar simulation in engineering and archaeology. *Geophysics*, 59(2):224–232, 1994.

[77] Dominic Lacroix. Computer simulations facilitating archaeological interpretations of ground-penetrating radar field data. *Unpublished Master's thesis, Department of Archaeology, University of Calgary, Calgary, Alberta*, 2009.

[78] Edoardo Pasolli, Farid Melgani, and Massimo Donelli. Automatic analysis of gpr images: A pattern-recognition approach. *Geoscience and Remote Sensing, IEEE Transactions on*, 47(7):2206–2217, 2009.

[79] Edoardo Pasolli, Farid Melgani, Massimo Donelli, Redha Attoui, and Mariette De Vos. Automatic detection and classification of buried objects in gpr images using genetic algorithms and support vector machines. In *IGARSS 2008-2008 IEEE International Geoscience and Remote Sensing Symposium*, volume 2, pages II–525. IEEE, 2008.

[80] PD Gader, BN Nelson, H. Frigui, G. Vaillette, and JM Keller. Fuzzy logic detection of landmines with ground penetrating radar. *Signal processing*, 80(6):1069–1084, 2000.

[81] S.H. Yu, R.K. Mehra, and T.R. Witten. Automatic mine detection based on ground-penetrating radar. In *Proceedings of SPIE*, volume 3710, page 961, 1999.

[82] C. Bruschini, B. Gros, F. Guerne, P.Y. Pièce, and O. Carmona. Ground penetrating radar and imaging metal detector for antipersonnel mine detection. *Journal of Applied Geophysics*, 40(1):59–71, 1998.

[83] T.P. Montoya and G.S. Smith. Land mine detection using a ground-penetrating radar based on resistively loaded vee dipoles. *Antennas and Propagation, IEEE Transactions on*, 47(12):1795–1806, 1999.

[84] SL Earp, ES Hughes, TJ Elkins, and R. Vickers. Ultra-wideband ground-penetrating radar for the detection of buried metallic mines. *Aerospace and Electronic Systems Magazine, IEEE*, 11(9):30–39, 1996.

[85] Y. Sun and J. Li. Time-frequency analysis for plastic landmine detection via forward-looking ground penetrating radar. In *Radar, Sonar and Navigation, IEE Proceedings-*, volume 150, pages 253–61. IET, 2003.

[86] J. Song, Q.H. Liu, P. Torrione, and L. Collins. Two-dimensional and three-dimensional nufft migration method for landmine detection using ground-penetrating radar. *Geoscience and Remote Sensing, IEEE Transactions on*, 44(6):1462–1469, 2006.

[87] A.M. Zoubir, I.J. Chant, C.L. Brown, B. Barkat, and C. Abeynayake. Signal processing techniques for landmine detection using impulse ground penetrating radar. *Sensors Journal, IEEE*, 2(1):41–51, 2002.

[88] P.D. Gader, M. Mystkowski, and Y. Zhao. Landmine detection with ground penetrating radar using hidden markov models. *Geoscience and Remote Sensing, IEEE Transactions on*, 39(6):1231–1244, 2001.

[89] Meng Sun, Jingjing Pan, Cédric Le Bastard, Yide Wang, and Jianzhong Li. Advanced signal processing methods for ground-penetrating radar: Applications to civil engineering. *IEEE Signal Processing Magazine*, 36(4):74–84, 2019.

[90] Wallace Wai-Lok Lai, Xavier Derobert, and Peter Annan. A review of ground penetrating radar application in civil engineering: A 30-year journey from locating and testing to imaging and diagnosis. *Ndt & E International*, 96:58–78, 2018.

[91] J.S. Lee, C. Nguyen, and T. Scullion. A novel, compact, low-cost, impulse ground-penetrating radar for nondestructive evaluation of pavements. *Instrumentation and Measurement, IEEE Transactions on*, 53(6):1502–1509, 2004.

[92] G.R. Olhoeft and S.S. Smith III. Automatic processing and modeling of gpr data for pavement thickness and properties. In *Proceedings of SPIE*, volume 4084, page 188, 2000.

[93] T. Saarenketo and T. Scullion. Road evaluation with ground penetrating radar. *Journal of applied geophysics*, 43(2):119–138, 2000.

[94] Christina Plati and Andreas Loizos. Estimation of in-situ density and moisture content in hma pavements based on gpr trace reflection amplitude using different frequencies. *Journal of Applied Geophysics*, 97:3–10, 2013.

[95] Pekka Eskelinen and Terhi Pellinen. Comparison of different radar technologies and frequencies for road pavement evaluation. *Construction and Building Materials*, 164:888–898, 2018.

[96] T. Saarenketo. Measuring electromagnetic properties of asphalt for pavement quality control and defect mapping, 2009.

[97] K.R. Maser. Condition assessment of transportation infrastructure using ground-penetrating radar. *Journal of infrastructure systems*, 2(2):94–101, 1996.

[98] U. Spagnolini and V. Rampa. Multitarget detection/tracking for monostatic ground penetrating radar: application to pavement profiling. *IEEE Transactions on Geoscience and Remote Sensing*, 37(1):383–394, 1999.

[99] Ju Huyan, Wei Li, Susan Tighe, Liyang Xiao, Zhaoyun Sun, and Nana Shao. Three-dimensional pavement crack detection based on primary surface profile innovation optimized dual-phase computing. *Engineering Applications of Artificial Intelligence*, 89:103376, 2020.

[100] Lech Krysiński and Jacek Sudyka. Gpr abilities in investigation of the pavement transversal cracks. *Journal of Applied Geophysics*, 97:27–36, 2013.

[101] Andrea Benedetto. A three dimensional approach for tracking cracks in bridges using gpr. *Journal of Applied Geophysics*, 97:37–44, 2013.

[102] Man-Sung Kang, Namgyu Kim, Jong Jae Lee, and Yun-Kyu An. Deep learning-based automated underground cavity detection using three-dimensional ground penetrating radar. *Structural Health Monitoring*, 19(1):173–185, 2020.

[103] Wallace WL Lai, Ray KW Chang, and Janet FC Sham. A blind test of nondestructive underground void detection by ground penetrating radar (gpr). *Journal of Applied Geophysics*, 149:10–17, 2018.

[104] Ying Liu, Daryoush Habibi, Douglas Chai, Xiuming Wang, Hao Chen, Yan Gao, and Shuaiyong Li. A comprehensive review of acoustic methods for locating underground pipelines. *Applied Sciences*, 10(3):1031, 2020.

[105] Fabrício Almeida, Michael Brennan, Phillip Joseph, Stuart Whitfield, Simon Dray, and Amarildo Paschoalini. On the acoustic filtering of the pipe and sensor in a buried plastic water pipe and its effect on leak detection: an experimental investigation. *Sensors*, 14(3):5595–5610, 2014.

[106] SA Ganiyu, MA Oladunjoye, OI Onakoya, JO Olutoki, and BS Badmus. Combined electrical resistivity imaging and ground penetrating radar study for detection of buried utilities in federal university of agriculture, abeokuta, nigeria. *Environmental Earth Sciences*, 79:1–20, 2020.

[107] Mohamed Metwaly. Application of gpr technique for subsurface utility mapping: A case study from urban area of holy mecca, saudi arabia. *Measurement*, 60:139–145, 2015.

[108] Simone Meschino, Lara Pajewski, Matteo Pastorino, Andrea Randazzo, and Giuseppe Schettini. Detection of subsurface metallic utilities by means of a sap technique: Comparing music-and svm-based approaches. *Journal of Applied Geophysics*, 97:60–68, 2013.

[109] Chenxi Yuan, Shuai Li, Hubo Cai, and Vineet R Kamat. Gpr signature detection and decomposition for mapping buried utilities with complex spatial configuration. *Journal of Computing in Civil Engineering*, 32(4):04018026, 2018.

[110] Shuai Li, Hubo Cai, Dulcy M Abraham, and Peng Mao. Estimating features of underground utilities: Hybrid gpr/gps approach. *Journal of Computing in Civil Engineering*, 30(1):04014108, 2016.

[111] Giulio Curioni, David N Chapman, and Nicole Metje. Seasonal variations measured by tdr and gpr on an anthropogenic sandy soil and the implications for utility detection. *Journal of Applied Geophysics*, 141:34–46, 2017.

[112] Jingxia Li, Tian Guo, Henry Leung, Hang Xu, Li Liu, Bingjie Wang, and Yang Liu. Locating underground pipe using wideband chaotic ground penetrating radar. *Sensors*, 19(13):2913, 2019.

[113] Aleksandar Ristić, Željko Bugarinović, Milan Vrtunski, and Miro Govedarica. Point coordinates extraction from localized hyperbolic reflections in gpr data. *Journal of Applied Geophysics*, 144:1–17, 2017.

[114] Triven Koganti, Ellen Van De Vijver, Barry J Allred, Mogens H Greve, Jorgen Ringgaard, and Bo V Iversen. Assessment of a stepped-frequency gpr for subsurface drainage mapping for different survey configurations and site conditions. In *10th International Workshop on Advanced Ground Penetrating Radar*, volume 2019, pages 1–7. European Association of Geoscientists & Engineers, 2019.

[115] Shan Zhao and Imad Al-Qadi. Pavement drainage pipe condition assessment by gpr image reconstruction using fdtd modeling. *Construction and Building Materials*, 154:1283–1293, 2017.

[116] F Frezza, L Pajewski, C Ponti, G Schettini, and N Tedeschi. Cylindrical-wave approach for electromagnetic scattering by subsurface metallic targets in a lossy medium. *Journal of Applied Geophysics*, 97:55–59, 2013.

[117] WY Zhang, T Hao, Y Chang, and YH Zhao. Time-frequency analysis of enhanced gpr detection of rf tagged buried plastic pipes. *Ndt & E International*, 92:88–96, 2017.

[118] David Ayala-Cabrera, Manuel Herrera, Joaquin Izquierdo, and Rafael Perez-Garcia. Location of buried plastic pipes using multi-agent support based on gpr images. *Journal of Applied Geophysics*, 75(4):679–686, 2011.

[119] Sheng-Huoo Ni, Yan-Hong Huang, Kuo-Feng Lo, and Da-Ci Lin. Buried pipe detection by ground penetrating radar using the discrete wavelet transform. *Computers and Geotechnics*, 37(4):440–448, 2010.

[120] FJ Prego, M Solla, I Puente, and P Arias. Efficient gpr data acquisition to detect underground pipes. *NDT & E International*, 91:22–31, 2017.

[121] Shantanu Datta and Shibayan Sarkar. A review on different pipeline fault detection methods. *Journal of Loss Prevention in the Process Industries*, 41:97–106, 2016.

[122] Bella Wei-Yat Cheung and Wallace Wai-Lok Lai. Field validation of water-pipe leakage detection through spatial and time-lapse analysis of gpr wave velocity. *Near Surface Geophysics*, 17(3):231–246, 2019.

[123] Wallace WL Lai, Ray KW Chang, Janet FC Sham, and K Pang. Perturbation mapping of water leak in buried water pipes via laboratory validation experiments with high-frequency ground penetrating radar (gpr). *Tunnelling and Underground Space Technology*, 52:157–167, 2016.

[124] Ahmed Atef, Tarek Zayed, Alaa Hawari, Mohammad Khader, and Osama Moselhi. Multi-tier method using infrared photography and gpr to detect and locate water leaks. *Automation in Construction*, 61:162–170, 2016.

[125] Silvia J Ocaña-Levario, Elizabeth P Carreño-Alvarado, David Ayala-Cabrera, and Joaquín Izquierdo. Gpr image analysis to locate water leaks from buried pipes by applying variance filters. *Journal of Applied Geophysics*, 152:236–247, 2018.

[126] R.H. Johnson and E.P. Poeter. Interpreting dnapl saturations in a laboratory-scale injection using one-and two-dimensional modeling of GPR data. *Ground Water Monitoring & Remediation*, 25(1):159–169, 2005.

[127] H.J. Siriwardane, S. Pyakurel, R. Kiriakidis, U.B. Halabe, and R. Ingram. Laboratory determination of phreatic surface during seepage through soils using ground penetrating radar. In *AIP CONFERENCE PROCEEDINGS*, volume 894, page 1389. IOP INSTITUTE OF PHYSICS PUBLISHING LTD, 2007.

[128] E. Yigit, S. Demirci, C. Ozdemir, and A. Kavak. A synthetic aperture radar-based focusing algorithm for b-scan ground penetrating radar imagery. *Microwave and Optical Technology Letters*, 49(10):2534–2540, 2007.

[129] Omer Shamir, Naftaly Goldshleger, Uri Basson, and Moshe Reshef. Laboratory measurements of subsurface spatial moisture content by ground-penetrating radar (gpr) diffraction and reflection imaging of agricultural soils. *Remote Sensing*, 10(10):1667, 2018.

[130] Dwain K Butler. *Near-surface geophysics*. Society of Exploration Geophysicists Tulsa, 2005.

[131] Harry M Jol. *Ground penetrating radar theory and applications*. Elsevier, 2008.

[132] Jim Lester and Leonhard E Bernold. Innovative process to characterize buried utilities using ground penetrating radar. *Automation in construction*, 16(4):546–555, 2007.

[133] John David Jackson and John D Jackson. *Classical electrodynamics*, volume 3. Wiley New York etc., 1962.

[134] Xiaoxian Zeng and George A McMechan. GPR characterization of buried tanks and pipes. *Geophysics*, 62(3):797–806, 1997.

[135] Mark E Everett. *Near-surface applied geophysics*. Cambridge University Press, 2013.

[136] JL Davis and AP Annan. Ground-penetrating radar for high-resolution mapping of soil and rock stratigraphy. *Geophysical prospecting*, 37(5):531–551, 1989.

[137] AP Annan. Ground penetrating radar workshop notes. *Sensors and Software Inc., Mississauga*, 402, 1992.

[138] Harry M Jol. Ground penetrating radar antennae frequencies and transmitter powers compared for penetration depth, resolution and reflection continuity. *Geophysical Prospecting*, 43(5):693–709, 1995.

[139] GC Topp, JL Davis, and Aa P Annan. Electromagnetic determination of soil water content: Measurements in coaxial transmission lines. *Water resources research*, 16(3):574–582, 1980.

[140] H.R. Cedergren. *DRAINAGE OF HIGHWAY AND AIRFIELD PAVEMENTS (ORIGINAL EDITION 1974; REPRINT 1987 WITH UPDATING)*. 1987.

[141] L.K. Moulton. Highway subdrainage design. Technical report, 1980.

[142] H Bai and JV Sinfield. Simulation analysis for under pavement drainage detection by ground penetrating radar (GPR). In *27th Annual Symposium on the Application of Geophysics to Engineering and Environmental Problems (SAGEEP)*, 2014.

[143] Jun Cai and George A McMechan. Ray-based synthesis of bistatic ground-penetrating radar profiles. *Geophysics*, 60(1):87–96, 1995.

[144] Michael H Powers and Gary R Olhoeft. Modeling the GPR response of leaking, buried pipes. In *Proceedings of the Symposium on the Application of Geophysics to Environmental and Engineering Problems*, pages 525–534, 1996.

[145] Xiaoxian Zeng, George A McMechan, Jun Cai, and How-Wei Chen. Comparison of ray and fourier methods for modeling monostatic ground-penetrating radar profiles. *Geophysics*, 60(6):1727–1734, 1995.

[146] Bernhard Lampe, Klaus Holliger, and Alan G Green. A finite-difference time-domain simulation tool for ground-penetrating radar antennas. *Geophysics*, 68(3):971–987, 2003.

[147] Levent Gurel and Ugur Oguz. Three-dimensional FDTD modeling of a ground-penetrating radar. *Geoscience and Remote Sensing, IEEE Transactions on*, 38(4):1513–1521, 2000.

[148] JR Bourgeois and Glenn S Smith. A fully three-dimensional simulation of a ground-penetrating radar: FDTD theory compared with experiment. *Geoscience and Remote Sensing, IEEE Transactions on*, 34(1):36–44, 1996.

[149] Hao Bai and Joseph V Sinfield. Improved background and clutter reduction for pipe detection under pavement using ground penetrating radar (gpr). *Journal of Applied Geophysics*, 172:103918, 2020.

[150] Joseph V. Sinfield and Hao Bai. Nondestructive evaluation of the condition of subsurface drainage in pavements using ground penetrating radar (gpr). publication fhwa/in/jtrp-2013/25. Technical report, Joint Transportation Research Program, Indiana Department of Transportation and Purdue University, West Lafayette, Indiana, 2013.

[151] F. Abujarad, G. Nadim, and A. Omar. Clutter reduction and detection of landmine objects in ground penetrating radar data using singular value decomposition (SVD). In *Proceedings of the 3rd International Workshop on Advanced Ground Penetrating Radar, 2005. IWAGPR 2005.*, pages 37–42. IEEE, 2005.

[152] Lorena Cedrina, Néstor Bonomo, and Ana Osella. Gpr-signal improvement using a synthetic emitter array. *Journal of Applied Geophysics*, 74(2-3):123–130, 2011.

[153] Hai Liu, Xiaoyun Huang, Feng Han, Jie Cui, Billie F Spencer, and Xiongyao Xie. Hybrid polarimetric gpr calibration and elongated object orientation estimation. *IEEE Journal of Selected Topics in Applied Earth Observations and Remote Sensing*, 12(7):2080–2087, 2019.

[154] F. Abujarad, A. Jostingmeier, and AS Omar. Clutter removal for landmine using different signal processing techniques. In *Proceedings of the Tenth International Conference on Ground Penetrating Radar, 2004. GPR 2004.*, pages 697–700. IEEE, 2004.

[155] R. Caldecott. An underground obstacle detection and mapping system. *Rep./EPRI/Electric power research inst.*, 1985.

[156] H. Brunzell. Detection of shallowly buried objects using impulse radar. *IEEE Transactions on Geoscience and Remote Sensing*, 37(2):875–886, 1999.

[157] D. Carevic. A kalman filter-based approach to target detection and target-background separation in ground penetrating radar data. Technical report, DTIC Document, 1999.

[158] U.S. Khan and W. Al-Nuaimy. Background removal from gpr data using eigenvalues. In *13th International Conference on Ground Penetrating Radar (GPR), 2010*, pages 1–5. IEEE, 2010.

[159] H. Brunzell. Clutter reduction and object detection in surface penetrating radar. In *Radar 97 (Conf. Publ. No. 449)*, pages 688–691. IET, 1997.

[160] T. Dogaru and L. Carin. Time-domain sensing of targets buried under a rough air-ground interface. *Antennas and Propagation, IEEE Transactions on*, 46(3):360–372, 1998.

[161] M. Sezgin. A novel detection warning signal creation method for hand-held GPR applications. In *13th International Conference on Ground Penetrating Radar (GPR), 2010*, pages 1–6. IEEE, 2010.

[162] M. Sezgin. Simultaneous buried object detection and imaging technique utilizing fuzzy weighted background calculation and target energy moments on ground penetrating radar data. *EURASIP Journal on Advances in Signal Processing*, 2011(1):1–12, 2011.

[163] Wei Xue, Jichao Zhu, Xia Rong, Yujin Huang, Yue Yang, and Yunyun Yu. The analysis of ground penetrating radar signal based on generalized s transform with parameters optimization. *Journal of Applied Geophysics*, 140:75–83, 2017.

[164] L. Nuzzo and T. Quarta. Improvement in gpr coherent noise attenuation using τ-p and wavelet transforms. *Geophysics*, 69(3):789–802, 2004.

[165] D. Carevic. Clutter reduction and detection of minelike objects in ground penetrating radar data using wavelets. *Subsurface Sensing Technologies and Applications*, 1(1):101–118, 2000.

[166] Mohamed Rashed and Hussein Harbi. Background matrix subtraction (bms): A novel background removal algorithm for gpr data. *Journal of Applied Geophysics*, 106:154–163, 2014.

[167] V Montiel-Zafra, FJ Canadas-Quesada, P Vera-Candeas, N Ruiz-Reyes, J Rey, and J Martinez. A novel method to remove gpr background noise based on the similarity of non-neighboring regions. *Journal of Applied Geophysics*, 144:188–203, 2017.

[168] Hai Liu, Bangan Xing, Jinfeng Zhu, Bin Zhou, Fei Wang, Xiongyao Xie, and Qing Huo Liu. Quantitative stability analysis of ground penetrating radar systems. *IEEE Geoscience and Remote Sensing Letters*, 15(4):522–526, 2018.

[169] W Al-Nuaimy, Y Huang, M Nakhkash, MTC Fang, VT Nguyen, and A Eriksen. Automatic detection of buried utilities and solid objects with gpr using neural networks and pattern recognition. *Journal of Applied Geophysics*, 43(2):157–165, 2000.

[170] S Delbo, P Gamba, and D Roccato. A fuzzy shell clustering approach to recognize hyperbolic signatures in subsurface radar images. *Geoscience and Remote Sensing, IEEE Transactions on*, 38(3):1447–1451, 2000.

[171] Nada Milisavljević, Isabelle Bloch, Sebastiaan van den Broek, and Marc Acheroy. Improving mine recognition through processing and dempster–shafer fusion of ground-penetrating radar data. *Pattern Recognition*, 36(5):1233–1250, 2003.

[172] Bernd Ehret. Pattern recognition of geophysical data. *Geoderma*, 160(1):111–125, 2010.

[173] Carl B Dietrich, Kai Dietze, J Randall Nealy, and Warren L Stutzman. Spatial, polarization, and pattern diversity for wireless handheld terminals. *IEEE transactions on antennas and propagation*, 49(9):1271–1281, 2001.

[174] Roger L Roberts and Jeffrey J Daniels. Analysis of GPR polarization phenomena. *Journal of Environmental and Engineering Geophysics*, 1(2):139–157, 1996.

[175] Stanley J Radzevicius and Jeffrey J Daniels. Ground penetrating radar polarization and scattering from cylinders. *Journal of Applied Geophysics*, 45(2):111–125, 2000.

[176] Jorge Luís Porsani, Evert Slob, Robson S Lima, and David Nakamura Leite. Comparing detection and location performance of perpendicular and parallel broadside GPR antenna orientations. *Journal of Applied Geophysics*, 70(1):1–8, 2010.

[177] P Lutz, S Garambois, and H Perroud. Influence of antenna configurations for GPR survey: information from polarization and amplitude versus offset measurements. *Geological Society, London, Special Publications*, 211(1):299–313, 2003.

[178] Jean-Paul Van Gestel, Paul L Stofa, et al. Multi-configuration ground penetrating radar data. In *1999 SEG Annual Meeting*. Society of Exploration Geophysicists, 1999.

[179] Jean-Paul Van Gestel, Paul L Stoffa, Mrinal K Sen, et al. Combining multi-configuration ground penetrating radar data using a weighted migration approach. In *2000 SEG Annual Meeting*. Society of Exploration Geophysicists, 2000.

[180] Jean-Paul Van Gestel and Paul L Stoffa. Migration using multiconfiguration GPR data. In *8th International Conference on Ground Penetrating Radar*, pages 448–452. International Society for Optics and Photonics, 2000.

[181] Mathieu Jeannin, Stéphane Garambois, Colette Grégoire, and Denis Jongmans. Multiconfiguration GPR measurements for geometric fracture characterization in limestone cliffs (Alps). *Geophysics*, 71(3):B85–B92, 2006.

[182] Christian Fischer and Werner Wiesbeck. Multistatic antenna configurations and image processing for mine-detection GPR. In *Proceedings of the 3rd DTIF workshop, Joint Research Centre European Commission, Ispra (VA) Italy*, pages 23–24, 2002.

[183] Levent Gürel and Uğur Oğuz. Optimization of the transmitter-receiver separation in the ground-penetrating radar. *Antennas and Propagation, IEEE Transactions*, 51(3):362–370, 2003.

[184] John H Bradford. Applying reflection tomography in the postmigration domain to multifold ground-penetrating radar data. *Geophysics*, 71(1):K1–K8, 2006.

[185] Levent Gürel and Uğur Oğuz. Transmitter-receiver-transmitter configurations of ground-penetrating radar. *Radio Science*, 37(3), 2002.

[186] Lanbo Liu, John W Lane, and Youli Quan. Radar attenuation tomography using the centroid frequency downshift method. *Journal of Applied Geophysics*, 40(1):105–116, 1998.

[187] Youli Quan and Jerry M Harris. Seismic attenuation tomography using the frequency shift method. *Geophysics*, 62(3):895–905, 1997.

[188] Andrea Benedetto. Water content evaluation in unsaturated soil using GPR signal analysis in the frequency domain. *Journal of Applied Geophysics*, 71(1):26–35, 2010.

[189] Tieyuan Zhu, José M. Carcione, and Marco A. B. Botelho. Reverse time imaging of ground-penetrating radar and sh-seismic data including the effects of wave loss. *Geophysics*, 81(4):H21–H32, 2016.

[190] John H Bradford. Frequency-dependent attenuation analysis of ground-penetrating radar data. *Geophysics*, 72(3):J7–16, 2007.

[191] J Pedret Rodés, V Pérez-Gracia, and A Martínez-Reguero. Evaluation of the GPR frequency spectra in asphalt pavement assessment. *Construction and Building Materials*, 96:181–188, 2015.

[192] José M Carcione, Géza Seriani, and Davide Gei. Acoustic and electromagnetic properties of soils saturated with salt water and napl. *Journal of Applied Geophysics*, 52(4):177–191, 2003.

[193] Ronald W Ward and M Nafi Toksöz. Causes of regional variation of magnitudes. *Bulletin of the Seismological Society of America*, 61(3):649–670, 1971.

[194] Norman Ricker. Wavelet functions and their polynomials. *Geophysics*, 9(3):314–323, 1944.

[195] Paul Gader, Wen-Hsiung Lee, and Joseph N Wilson. Detecting landmines with ground-penetrating radar using feature-based rules, order statistics, and adaptive whitening. *IEEE Transactions on Geoscience and Remote Sensing*, 42(11):2522–2534, 2004.

[196] Fok Hing Chi Tivive, Abdesselam Bouzerdoum, and Canicious Abeynayake. Gpr target detection by joint sparse and low-rank matrix decomposition. *IEEE Transactions on Geoscience and Remote Sensing*, 57(5):2583–2595, 2018.

[197] Deliang Xiang, Kai Zhou, Yi Su, et al. Fast prescreening for gpr antipersonnel mine detection via go decomposition. *IEEE Geoscience and Remote Sensing Letters*, 16(1):15–19, 2018.

[198] Yıldırım Bahadırlar and Mehmet Sezgin. Ca-cfar detection against k-distributed clutter in gpr. In *Detection and Remediation Technologies for Mines and Minelike Targets XII*, volume 6553, page 65532E. International Society for Optics and Photonics, 2007.